

STARS


University of Central Florida
STARS

Electronic Theses and Dissertations, 2004-2019

2005

Seawinds Radiometer Brightness Temperature Calibration And Validation

Mayank Rastogi
University of Central Florida

 Part of the [Electrical and Electronics Commons](#)
Find similar works at: <https://stars.library.ucf.edu/etd>
University of Central Florida Libraries <http://library.ucf.edu>

This Masters Thesis (Open Access) is brought to you for free and open access by STARS. It has been accepted for inclusion in Electronic Theses and Dissertations, 2004-2019 by an authorized administrator of STARS. For more information, please contact STARS@ucf.edu.

STARS Citation

Rastogi, Mayank, "Seawinds Radiometer Brightness Temperature Calibration And Validation" (2005).
Electronic Theses and Dissertations, 2004-2019. 494.
<https://stars.library.ucf.edu/etd/494>



SeaWinds RADIOMETER BRIGHTNESS TEMPERATURE CALIBRATION AND VALIDATION

by

MAYANK RASTOGI

B.Tech. Amity School of Engineering and Technology, New Delhi, 2003

A thesis submitted in partial fulfillment of the requirements
for the degree of Master of Science
in the Department of Electrical and Computer Engineering
in the College of Engineering and Computer Science
at the University of Central Florida
Orlando, Florida

Summer Term
2005

ABSTRACT

The NASA SeaWinds scatterometer is a radar remote sensor which operates on two satellites; NASA's QuikSCAT launched in June 1999 and on Japan's ADEOS-II satellite launched in December 2002. The purpose of SeaWinds is to provide global measurements of the ocean surface wind vector. On QuikSCAT, a ground data processing algorithm was developed, which allowed the instrument to function as a QuikSCAT Radiometer (QRad) and measure the ocean microwave emissions (brightness temperature, Tb) simultaneously with the backscattered power. When SeaWinds on ADEOS was launched, this same algorithm was applied, but the results were anomalous. The initial SRad brightness temperatures exhibited significant, unexpected, ascending/descending orbit Tb biases.

This thesis presents an empirical correction algorithm to correct the anomalous SeaWinds Radiometer (SRad) ocean brightness temperature measurements. I use the Advanced Microwave Scanning Radiometer (AMSR) as a brightness temperature standard to calibrate and then, with independent measurements, validate the corrected SRad Tb measurements. AMSR is a well-calibrated multi-frequency, dual-polarized microwave radiometer that also operates on ADEOS-II.

These results demonstrate that, after tuning the Tb algorithm, good quality SRad brightness temperature measurements are obtained over the oceans.

This thesis is dedicated to my Parents.

ACKNOWLEDGMENTS

This thesis has been an enormous learning experience and a great accomplishment on my part which would not have been possible without the guidance, support and time of my advisor Dr. Linwood Jones. I appreciate the endless help from my mentor and colleague Ian Adams. I am also thankful to my team members for their assistance during the challenging stages of my thesis. I am grateful to my committee, Dr. Takis Kasparis and Dr. Stephen Watson for their time and interest in my work. Also I would like to thank my family and friends for their well wishes, encouragement and patience.

This work was sponsored under a grant with the Oregon State University for research supporting the NASA Headquarters SeaWinds Program for ADEOS-II.

TABLE OF CONTENTS

LIST OF TABLES	vi
LIST OF FIGURES	vii
LIST OF ACRONYMS	xi
CHAPTER 1. INTRODUCTION	1
1.1 SeaWinds On QuikSCAT	3
1.2 SeaWinds on ADEOS-II	8
1.3 Oceanic Rain	9
CHAPTER 2. SeaWinds BRIGHTNESS TEMPERATURE MEASUREMENT	11
2.1 QRad External Radiometric Calibration using TMI	11
2.2 QRad Radiometric Calibration Results	14
2.3 SeaWinds Radiometer (SRad)	16
CHAPTER 3. SRad BRIGHTNESS TEMPERATURE RADIOMETRIC CALIBRATION	22
3.1 Radiometric Calibration Approach	22
3.2 QRad Empirical Tb Correction	25
CHAPTER 4. SRad BRIGHTNESS TEMPERATURE VALIDATION	34
4.1 Comparison of SRad and AMSR	35
CHAPTER 5. CONCLUSIONS	50
APPENDIX A. QRad RADIOMETRIC TRANSFER FUNCTION	52
A.1 Variable Definitions	55
A.2 Other Terms	59
A.3 Algorithmic Architecture	61
APPENDIX B. SRad FOURIER CORRECTION COEFFICIENTS	64
APPENDIX C. ADEOS-II AMSR BRIGHTNESS TEMPERATURE CALIBRATION	67
C.1 RadTb Tuning using WindSat	68
C.2 ADEOS AMSR Comparison with AMSR-E	75
APPENDIX D. SRad VALIDATION RESULTS	78
LIST OF REFERENCES	103

LIST OF TABLES

Table 2.1. Linear regression of QRad to TMI ocean brightness temperatures	16
Table 3.1. Frequency and Incidence angle differences for SeaWinds and AMSR	24
Table 4.1. SRad/AMSR overall (averaged over latitude) Mean and Std	47
Table 4.2. Independent Data sets of 2-day ocean delta Tb (SRad-AMSR) used for Validation	48
Table 4.3. Typical SRad – AMSR Delta-Tb, Sept. 1 st , 2003	48
Table 4.4. SRad/AMSR Linear Regression, Sept. 1 st , 2003	49
Table B.1. Fourier Coefficients of SRad Empirical Correction, H-Pol	65
Table B.2. Fourier Coefficients of SRad Empirical Correction, V-Pol	66
Table C.1. Typical AMSR – AMSR-E Delta-Tb, 3-day avg Sept. (1-3), 2003	77

LIST OF FIGURES

Figure 1.1 SeaWinds Measurement Geometry	5
Figure 1.2 SeaWinds Radiometersimplified receiver functional diagram	5
Figure 1.3 SeaWinds Received Power Spectrum	6
Figure 1.4 ADEOS-II Satellite with Five Instruments	9
Figure 2.1 Spectral Ratio Vs Water Vapor	13
Figure 2.2 Comparison of QRad and TMI ocean brightness temperatures for rain-free five day average	15
Figure 2.3 Three-day average, rain-free, ocean brightness temperature probability density function	15
Figure 2.4 SRad ocean Tb histograms – ascending and descending orbit segments	18
Figure 2.5 QRad ocean Tb histograms – ascending and descending orbit segments	19
Figure 2.6 (QRad – SRad) Tb H-pol delta-Tb latitude series	20
Figure 3.1 Spectral Ratio H-Pol Vs Water Vapor	24
Figure 3.2 SRad-AMSR Biases along the land/ocean boundaries	26
Figure 3.3 Conservative land mask to remove the land contaminated data	26
Figure 3.4 (SRad - AMSR) H-pol delta-Tb latitude series	27
Figure 3.5 (SRad – AMSR) radiometric bias (y-axis) latitude series (x-axis) for three days	29
Figure 3.6 Fourier Series for seven months for H-Polarization	30
Figure 3.7 Fourier Series for seven months for V-Polarization	30
Figure 3.8 (SRad - AMSR) H-pol delta-Tb average for ascending orbit segment	32
Figure 3.9 (SRad - AMSR) H-pol delta-Tb average for descending orbit segment	33
Figure 4.1 (SRad - AMSR) H-pol delta-Tb ascending segments (Sept 1 st , 2003)	36

Figure 4.2 (SRad - AMSR) H-pol delta-Tb descending segments (Sept 1 st , 2003)	37
Figure 4.3 (SRad – AMSR) H-pol delta Tb ascending segments histogram (Sept 1 st , 2003)	39
Figure 4.4 (SRad – AMSR) H-pol delta Tb descending segments histogram (Sept 1 st , 2003)	40
Figure 4.5 (SRad – AMSR) V-pol delta Tb ascending segments histogram (Sept 1 st , 2003)	41
Figure 4.6 (SRad – AMSR) V-pol delta Tb descending segments histogram (Sept 1 st , 2003)	42
Figure 4.7 Delta Tb (SRad – AMSR) image after Fourier correction for H-Pol	44
Figure 4.8 Delta Tb (SRad – AMSR) image after Fourier correction for V-Pol	45
Figure 4.9 Comparison of SRad and AMSR H-pol brightness temperatures for ascending (red) and descending (blue) orbit segments	46
Figure A.1 QuikSCAT Radiometer Equivalent Block Diagram	54
Figure C.1 Brightness Temperature Error Vs Sea Surface Temperature, 10.7 GHz	69
Figure C.2 Brightness Temperature Error Vs Sea Surface Temperature, 18.7 GHz	70
Figure C.3 Brightness Temperature Error Vs Wind Speed, 10.7 GHz	71
Figure C.4 Brightness Temperature Error Vs Wind Speed, 18.7 GHz	72
Figure C.5 Brightness Temperature Error Vs Water Vapor, 10.7 GHz	73
Figure C.6 Brightness Temperature Error Vs Water Vapor, 18.7 GHz	74
Figure D.1 (SRad - AMSR) H-pol 2-day avg delta-Tb ascending orbit segments (April 30 - May 1,2003)	79
Figure D.2 (SRad - AMSR) H-pol 2-day avg delta-Tb descending orbit segments (April 30 - May 1,2003)	80
Figure D.3 (SRad - AMSR) V-pol 2-day avg delta-Tb ascending orbit segments (April 30 - May 1,2003)	81
Figure D.4 (SRad - AMSR) V-pol 2-day avg delta-Tb descending orbit segments (April 30 - May 1,2003)	82
Figure D.5 (SRad - AMSR) H-pol 2-day avg delta-Tb ascending orbit segments (May 31 - June 1,2003)	83

Figure D.6 (SRad - AMSR) H-pol 2-day avg delta-Tb descending orbit segments (May 31 - June 1,2003)	84
Figure D.7 (SRad - AMSR) V-pol 2-day avg delta-Tb ascending orbit segments (May 31 - June 1,2003)	85
Figure D.8 (SRad - AMSR) V-pol 2-day avg delta-Tb descending orbit segments (May 31 - June 1,2003)	86
Figure D.9 (SRad - AMSR) H-pol 2-day avg delta-Tb ascending orbit segments (June 30 - July 1,2003)	87
Figure D.10 (SRad - AMSR) H-pol 2-day avg delta-Tb descending orbit segments (June 30 - July 1,2003)	88
Figure D.11 (SRad - AMSR) V-pol 2-day avg delta-Tb ascending orbit segments (June 30 - July 1,2003)	89
Figure D.12 (SRad - AMSR) V-pol 2-day avg delta-Tb descending orbit segments (June 30 - July 1,2003)	90
Figure D.13 (SRad - AMSR) H-pol 2-day avg delta-Tb ascending orbit segments (July 31 - August 1,2003)	91
Figure D.14 (SRad - AMSR) H-pol 2-day avg delta-Tb descending orbit segments (July 31 - August 1,2003)	92
Figure D.15 (SRad - AMSR) V-pol 2-day avg delta-Tb ascending orbit segments (July 31 - August 1,2003)	93
Figure D.16 (SRad - AMSR) V-pol 2-day avg delta-Tb descending orbit segments (July 31 - August 1,2003)	94
Figure D.17 (SRad - AMSR) H-pol 2-day avg delta-Tb ascending orbit segments (August 31 - September 1,2003)	95
Figure D.18 (SRad - AMSR) H-pol 2-day avg delta-Tb descending orbit segments (August 31 - September 1,2003)	96
Figure D.19 (SRad - AMSR) V-pol 2-day avg delta-Tb ascending orbit segments (August 31 - September 1,2003)	97
Figure D.20 (SRad - AMSR) V-pol 2-day avg delta-Tb descending orbit segments (August 31 - September 1,2003)	98
Figure D.21 (SRad - AMSR) H-pol 2-day avg delta-Tb ascending orbit segments (September 30 - October 1,2003)	99

Figure D.22 (SRad - AMSR) H-pol 2-day avg delta-Tb descending orbit segments (September 30 - October 1,2003)	100
Figure D.23 (SRad - AMSR) V-pol 2-day avg delta-Tb ascending orbit segments (September 30 - October 1,2003)	101
Figure D.24 (SRad - AMSR) V-pol 2-day avg delta-Tb descending orbit segments (September 30 - October 1,2003)	102

LIST OF ACRONYMS

QRad	QuikSCAT Radiometer
SRad	SeaWinds Radiometer
AMSR	Advanced Microwave Scanning Radiometer
TRMM	Tropical Rainfall Measuring Mission
SSM/I	Special Sensor Microwave/Imager
NASA	National Aeronautics and Space Administration
TMI	TRMM Microwave Imager
IFOV	Instantaneous field of view
SST	Sea Surface Temperature
CLW	Cloud Liquid Water
WS	Wind Speed
WV	Water Vapor
CFRSL	Central Florida Remote Sensing Laboratory

CHAPTER 1

INTRODUCTION

Earth remote sensing is the science of acquiring geophysical information about the Earth's atmosphere and surface without being in physical contact. This is accomplished by using electromagnetic techniques, over a wide range of frequencies from RF to beyond visible light, which involves measuring the reflected or emitted energy and analyzing this information to infer the relevant physical conditions that produced the remote sensing observations. The process involves an interaction between incident radiation and the targets (dielectric media) of interest.

As oceans cover 70 percent of the earth surface, characterizing the interaction between air and sea is vital for developing a robust understanding of the Earth's weather and climactic processes. The advent of Earth remote sensing satellites in the 1970's, with their unprecedented ability to provide global coverage, together with the simultaneous development of sophisticated sensors and data processing systems, has led to rapid advances in applying sensing techniques over the world's. Even today, satellite remote sensing of the ocean and atmosphere continues to evolve with a wide range of operational sensors in orbit, and new platforms with enhanced sensor capabilities continue to be planned, constructed and launched.

The driving force of this air-sea interaction is the stress or friction of the wind, which affects everything from ocean movements (waves and currents) to atmospheric weather systems and long-term climactic patterns. Hence surface wind velocity (speed and direction) proves to be an important

parameter to be incorporated in regional and global numerical meteorological (weather) and oceanographic models. Before the advent of satellite-based wind measurements, ocean surface wind vectors were acquired from infrequent (about 15,000 observations/day), non-uniform spatial coverage (concentrated along shipping routes), and often inaccurate reports from commercial ships, augmented by a less than 100 high quality weather ships and anchored buoys around the world. The accuracy of the weather prediction model depends (in part) on the availability of reliable measurements of ocean surface winds that are sampled uniformly in space and time over the world's oceans. Spaceborne microwave remote sensing instruments can fulfill this requirement by providing twice daily observations distributed over approximately 90 percent of the ice-free oceans (greater than 250 thousand/day). Satellite-borne passive microwave instruments, known as radiometers, and active microwave instruments, known as scatterometers, are capable of measuring ocean surface wind speed; but primarily scatterometers have provided wind velocity (both speed and direction). Over the past two and a half decades, scatterometers have demonstrated the capability of providing accurate measurements of ocean surface wind velocity under day/night and all-weather conditions [1].

A scatterometer is a special purpose microwave radar designed specifically to measure ocean surface wind speed and direction [2]. This active microwave radar transmits pulses and measures the echo energy, radar backscatter, which is used to calculate the reflection coefficient, called the normalized radar cross-section (σ^0) of the ocean surface area illuminated by the sensor antenna. As the wind blows over the ocean, the surface is roughened by the generation of centimeter-scale capillary waves that are the major contributor to the ocean surface backscatter reflectivity through the Bragg scattering mechanism. For a given ocean wind vector measurement cell, the scatterometer obtains multiple measurements of σ^0 from different azimuth angles that are used to infer the near-surface wind vector.

NASA's SeaWinds scatterometer was flown on QuickSCAT (launched in June 1999) and ADEOS-II (launched in December 2002) missions. On both missions, the SeaWinds instrument also provide a radiometric brightness temperature measurement, referred to as QRad on QuikSCAT and SRad on ADEOS-II, which were used for rain corrections to wind vector measurements. Although the SeaWinds instrument had the same design, the satellites are very different causing the on-orbit instrument thermal environments to be significantly different. The QRad radiometric transfer function is assumed to be applicable for SRad; but for SRad many radiometric measurements could not be performed during the initial on-orbit calibration. Specifically for ADEOS-II, no spacecraft maneuver was available to point the SeaWinds antenna to space, which complicates the determination of front-end ohmic losses and balancing of V- and H-Pol channels. Because of these differences, the QRad transfer function was not adequate to perform the intended operation of converting the SRad received noise measurements into ocean surface brightness temperature. Thus, the objective of this thesis is to calibrate and validate the SeaWinds radiometric transfer function on ADEOS-II so that good quality SRad brightness temperature measurements are obtained over the oceans. For this analysis, data from a well-calibrated radiometer also flying on ADEOS-II is used. This instrument known as the Advanced Microwave Scanning Radiometer (AMSR), is a multi frequency microwave radiometer that serves as a "brightness temperature standard" to first calibrate and then, using independent measurements, validate SRad Tb measurements.

1.1 SeaWinds on QuikSCAT

The first SeaWinds launched was a microwave Ku-band (13.4 GHz) scatterometer that is currently operating on a dedicated small, polar-orbiting satellite known as QuikSCAT. Unlike its satellite

scatterometer predecessors (SASS and NSCAT) that used multiple fixed fan beam antennas [2], SeaWinds uses a rotating parabolic dish antenna to collect σ^0 as shown in Fig. 1.1 [10]. Measurements are made over the entire conical scan (forward and aft looking) with separate offset pencil beams at vertical (v-pol) and horizontal (h-pol) polarizations respectively for outer and inner beams. The antenna produces a slightly elliptical instantaneous field of view (IFOV) approximately 30 km X 40 km (inner beam). As a result of the dual-beam operation, each wind vector cell on the surface in the overlapping region of the inner and outer beams, is viewed at four different azimuth look angles.

The SeaWinds Radiometer simplified functional block diagram is shown in Fig. 1.2. SeaWinds measures both signal (ocean surface echo) and noise (blackbody radiation captured by the antenna plus internal electronic noise) in dual receiver channels. In ground signal processing, these quantities are separated to yield an estimate of the sea surface reflectivity, (σ^0) and ocean/atmosphere blackbody microwave emission (brightness temperature, T_b).

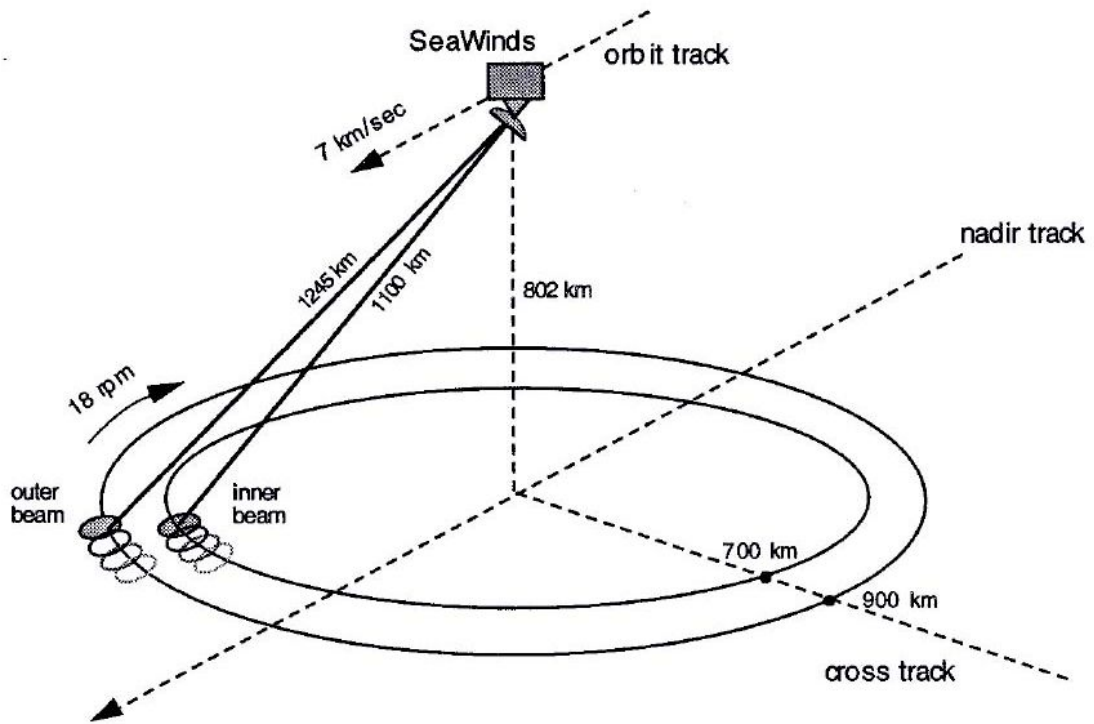


Figure 1.1 SeaWinds Measurement Geometry

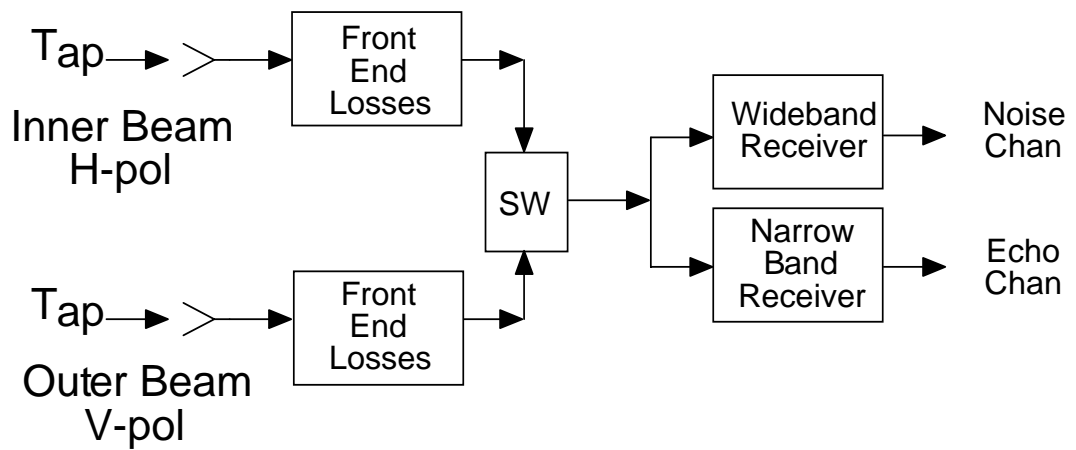


Figure 1.2 SeaWinds Radiometer simplified receiver functional diagram

The SeaWinds received signal (radar echo and blackbody noise) spectrum is shown in Fig. 1.3. For the scatterometer σ^0 measurement, the ocean backscatter echo is totally captured in the narrow band (250 KHz) “echo channel”, while simultaneously both echo and blackbody noise are also received in a second wideband (1 MHz) receiver “noise channel”. While both channels capture signal and noise, the resulting signal-to-noise ratios (SNR’s) are considerably different. Thus, by integrating the channel power for a time period (τ) and then subtracting the two channel outputs, the resulting differential signal is only noise energy (i.e., the echo is removed). Then, the noise energy, derived from the differential noise channel measurement, is subtracted from the (signal + noise) energy of the echo channel to yield only the echo signal, which is used to calculate the ocean σ^0 [4].

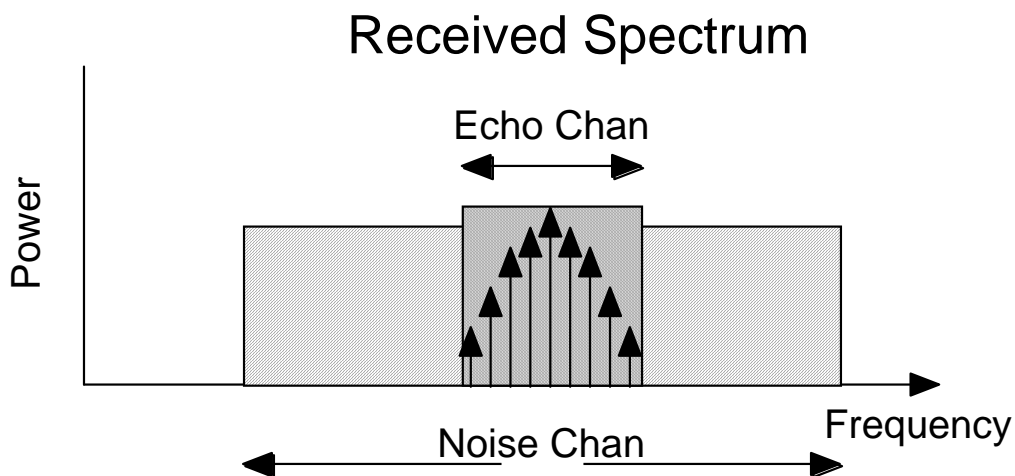


Figure 1.3 SeaWinds Received Power Spectrum

For the ocean Tb measurement, the above process is reversed, and the echo channel output energy (E_e) is subtracted from the noise channel output energy (E_n) to yield the total system noise energy (N), which is given by,

$$N = E_n - \beta E_e = k T_{sys} (B_n - B_e) G_n \tau \quad (1.1)$$

where

k = Boltzmann's constant, Joules/K;

B_n = noise channel bandwidth, Hz;

B_e = echo channel bandwidth, Hz;

τ = Range gate width (integration period), sec;

T_{sys} = system noise (radiometric) temperature, K, defined as

and $\beta = \frac{G_n}{G_e}$ is the gain ratio where G_n is the noise channel gain and G_e is the echo

channel gain.

The system noise temperature is given by,

$$T_{sys} = T_{ant} + T_{rec} \quad (1.2)$$

where T_{ant} is the antenna radiometric temperature and T_{rec} is the receiver noise temperature.

The antenna temperature input to the receiver includes both the Earth's apparent brightness temperature (T_{ap}) collected by the antenna and the noise emitted from the front end loss:

$$T_{ant} = T_{ap} * L_{fe} + (1 - L_{fe}) * T_{phys} , \text{ K} \quad (1.3)$$

where,

T_{ap} = ocean apparent brightness temperature

L_{fe} = front-end loss power ratio

T_{phys} = front-end loss physical temperature

Since the front-end losses, their physical temperatures, the receiver noise figure are known from pre-launch calibration and the channel gains are measured on-orbit, the ocean brightness temperature can be determined from the noise only measurements. Of course the actual system is more complicated; and a detailed derivation of the QRad radiometer transfer function and the associated Tb algorithm is given in Appendix A[6][7].

1.2 SeaWinds on ADEOS-II

The second (identical) SeaWinds scatterometer design was launched on Japan's Advance Earth Observing Satellite-II (ADEOS-II) on December 14, 2002 into a sun-synchronous orbit. ADEOS-II carried five remote sensing instruments (see Fig. 1.4) including the Advanced Microwave Scanning Radiometer (AMSR) developed by National Space Development Agency of Japan (NASDA).

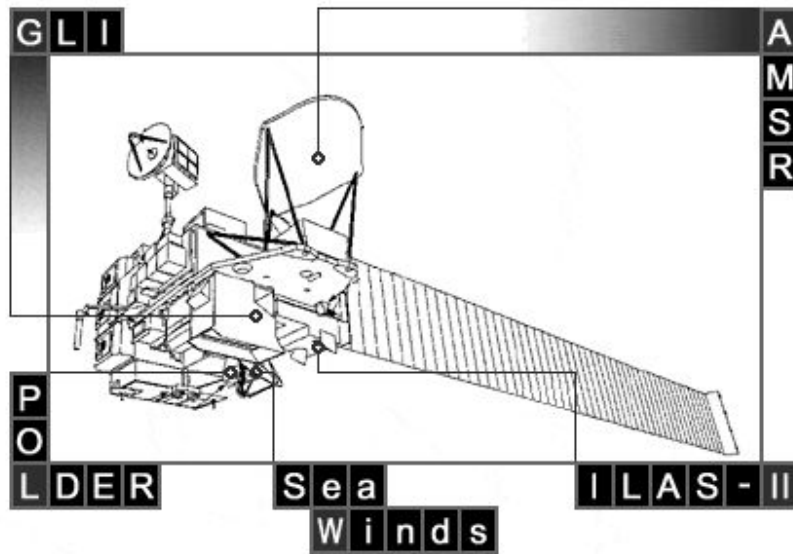


Figure 1.4 ADEOS-II Satellite with Five Instruments

1.3 Oceanic Rain

Rain affects scatterometer radar measurements in three ways: 1) rain attenuates the transmitted signal and the signal backscattered from the sea surface (i.e., two-way attenuation); 2) rain backscatters some of the transmitted signal; and 3) rain alters the sea surface's radar cross section and therefore contaminates the estimation of the sea surface wind speed and direction [11]. On a global average basis, rain occurs simultaneously with a typical low earth orbiting remote sensing satellite observations less than 4 to 6 % of the times. Although this number is not large, never the less, as the spatial and temporal distribution of rain is not random; so the existence of significant systematic biases in scatterometer measure wind fields is highly probable [11].

Ocean radiometric observations with rain have higher brightness temperatures than those without rain; therefore, rain rate can be estimated from measuring ocean brightness temperatures. A QRad rain

rate algorithm has been developed at CFRSL [7][8]. , This algorithm was based upon a statistical correlation between simultaneous SeaWinds excess brightness temperature and rain rate derived from the Tropical Rainfall Measuring Mission Microwave Imager (TMI). The excess brightness temperature is defined as the residual of the average measured SeaWinds brightness temperature after subtracting the ocean background brightness temperature (non-raining atmosphere) and the brightness due to the surface wind speed. Thus the remaining excess brightness is assumed to be solely due to rain

$$Tex_{bp} = T_{bp} - T_bOcean_p - T_bW.speed_p \quad (1.4)$$

where,

T_{bp} = SeaWinds measured brightness temperature

T_bOcean_p = Ocean background brightness temperature

$T_bW.speed_p$ = Wind speed brightness bias

and p refers to the polarization.

A detailed discussion of the SeaWinds brightness temperature measurement is covered in the next chapter.

CHAPTER 2

SeaWinds BRIGHTNESS TEMPERATURE MEASUREMENT

2.1 QRad External Radiometric Calibration using TMI

Since the SeaWinds instrument was not originally intended for radiometric (brightness temperature) measurements, it did not have provisions for absolute radiometric calibration (i.e., separate hot and cold load calibration targets). Fortunately, there are several operating microwave radiometer systems on-orbit that can be used as secondary standards to calibrate the QRad system (e.g., TMI). The approach taken was to compare 3-day average earth microwave emissions obtained with QRad and TMI over rain-free oceans and to equate the mean QRad brightness temperatures to those of the calibrated system [4] [5].

However, because the QRad operates at different incidence angles (46° and 54°) and a different frequency (13.4 GHz) than the TMI, “equivalent” QRad brightness temperature was calculated using measured TMI brightness temperatures that were interpolated in frequency and extrapolated in incidence angle. The QRad polarized brightness temperature was calculated using the measured TMI brightness temperature difference between the 10.7 and 19 GHz channels as :

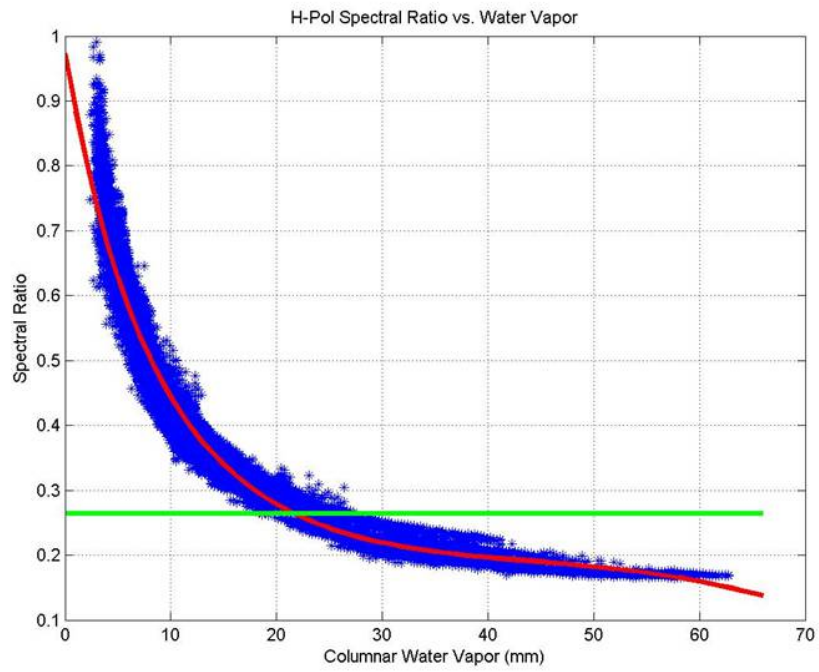
$$T_{13.4p} = (T_{19} - T_{10.7}) * (\text{spectralratio})_p + T_{10.7}, K \quad (2.1)$$

where p = V or H

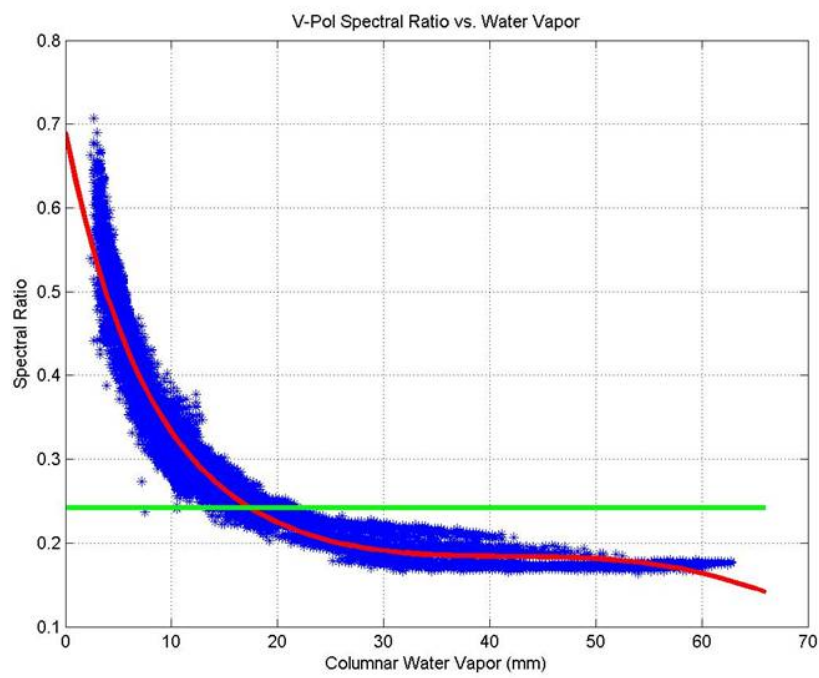
and spectral ratio is given as:

$$(\text{spectralratio})_p = \frac{(T_{13 \text{ mod}} - T_{10 \text{ mod}})}{(T_{19 \text{ mod}} - T_{10 \text{ mod}})}, \text{ ratio} \quad (2.2)$$

To calculate the spectral ratio, 14 monthly-averaged environmental parameters (e.g., sea surface temperature, wind speed, water vapor, cloud liquid, etc.) were used as input to a radiative transfer model, which was run with QRad incidence angles (H-pol = 46 deg, V-pol = 54 deg) to calculate the ocean brightness temperatures at 13.4 GHz. The same process was repeated to generate brightness temperatures at two TMI frequencies (10.7 GHz and 19.4 GHz) using the TMI incidence angle of 52.1deg. Figure 2.1 shows the (a) H-Pol and (b) V-Pol spectral ratio versus water vapor. The red line indicates the regression developed for the SRad spectral ratio and the green line denotes the previously used QRad constant spectral ratio.



(a) H-Pol



(b) V-Pol

Figure 2.1 Spectral Ratio Vs Water Vapor

2.2 QRad Radiometric Calibration Results

The following is a summary of the work previously performed at CFRSL and documented by Ahmad [9]. An example of linear regression scatter diagrams for QRad and TMI equivalent brightness temperatures, T_b , using (eq 2.1) is given in Fig. 2.2 for both H- and V-pols. Data is rain-free combined horizontal and vertical polarization three-day averaged ocean brightness temperatures. TMI brightness temperatures are interpolated to the QRad frequency and extrapolated to the QRad incidence angle. The symbols are binned and averaged QRad and TMI T_b s with H-pol being the symbols close to 100K, and the error bars denoting +/- one standard deviation [9]. The dashed line (the 45 degree line) is the perfect agreement (offset equal to zero and slope equal to unity) and the solid line shows the least square regression. The stability of this external calibration procedure is good as observed from the resulting regression slope and offset for several different calibrations during 2000 that are provided in Table 2.1 [9].

Another assessment of the QRad calibration stability compares histograms of QRad and TMI equivalent ocean T_b taken seasonally. Here, three-day averages of ocean brightness temperatures were produced with rain removed, and a typical set of histograms is shown in Figure 2.3. For H-Pol, QRad median T_b is within 1 Kelvin of TMI; but for V-Pol QRad results are low by a few Kelvin. The TMI histograms are almost Gaussian. The QRad histograms are also almost Gaussian but have a lower peak i.e. are spread out because of the increased QRad ΔT . [9]

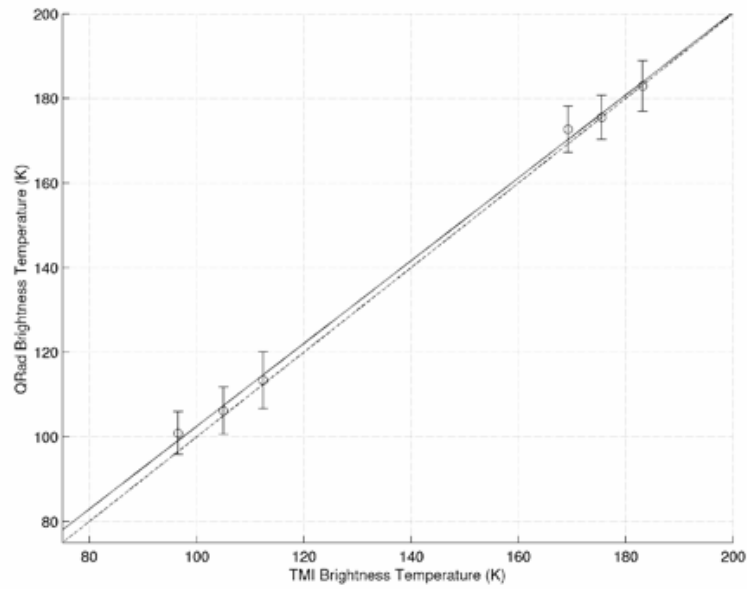


Figure 2.2 Comparison of QRad and TMI ocean brightness temperatures for rain-free five day average

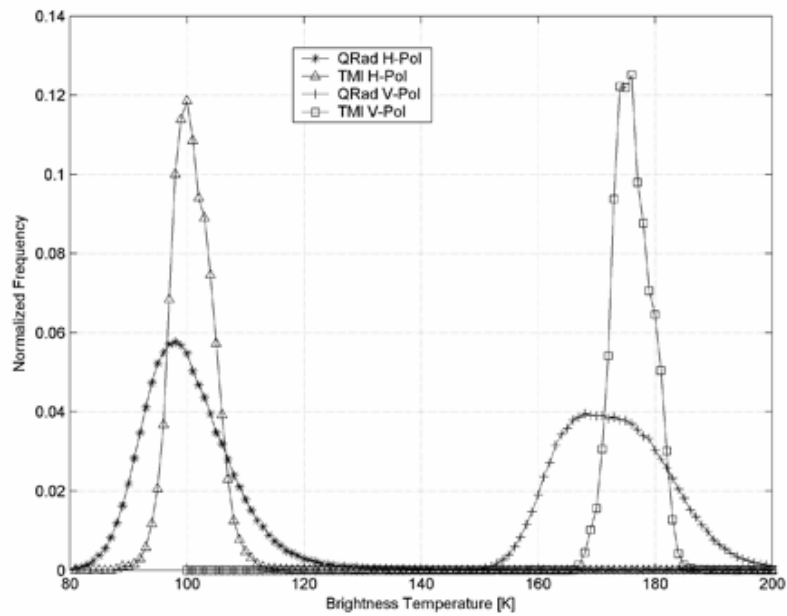


Figure 2.3 Three-day average, rain-free, ocean brightness temperature probability density function

Table 2.1. Linear regression of QRad to TMI ocean brightness temperatures

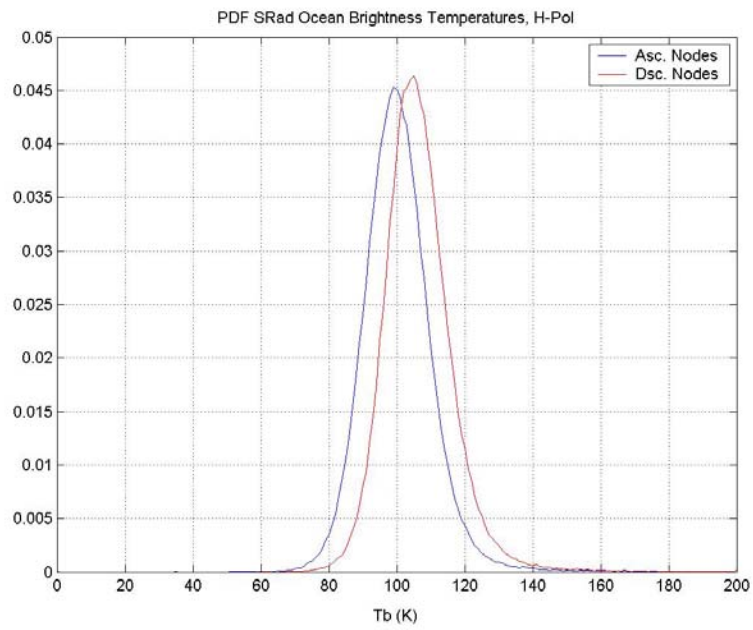
Date	Offset	Slope
Sept. '99	6.55 K	0.977
June '00	6.32 K	0.955
Jan. '01	9.07 K	0.958
Apr. '03	4.67 K	0.978

2.3 SeaWinds Radiometer (SRad)

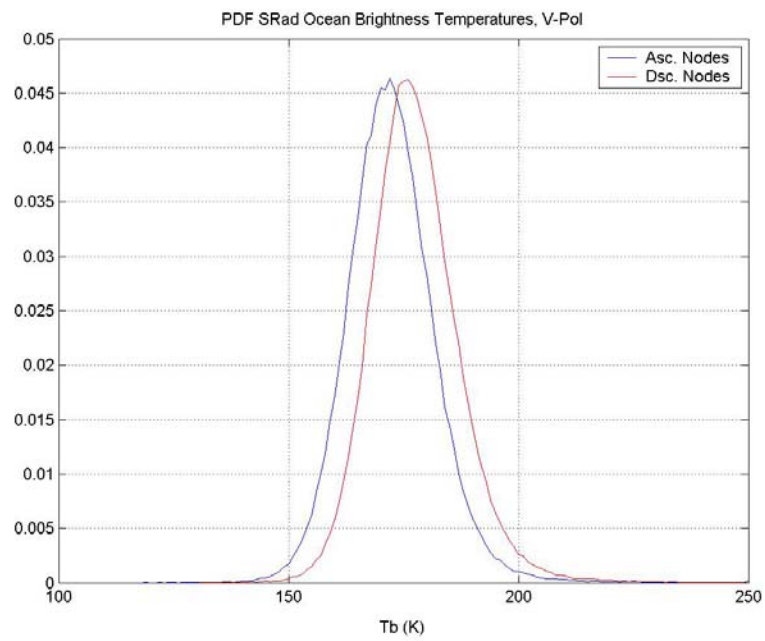
After the launch of SeaWinds on ADEOS-II, first Tb comparisons were made between SRad and QRad. Because of the difference in the orbits of QuikSCAT and ADEOS-II, simultaneous Tb comparisons were not possible; so global images of polarized Tb, separately for the ascending and descending portions of the orbit and polarizations, were examined. To produce global images, 3-day average of Tb over the ocean was used because it takes approximately 3 days to fill out the “gaps” between orbits. When comparing the corresponding 3-day images for both instruments, there were notable Tb differences observed for ascending/descending segments for both polarizations [12]. Further, by comparing histograms of the ocean brightness temperature for ascending and descending portions, the SRad ascending brightness temperatures (Figure 2.4, (a) H-Pol and (b) V-Pol) were found to be colder by about 5K, while QRad ascending/descending brightness temperatures were found to be equal (Fig 2.5, (a) H-Pol and (b) V-Pol) . Similar results were found for both polarizations.

To determine whether or not the SRad Tb bias varied with orbit position as a function of latitude, the difference between SRad and QRad Tb's were calculated for the corresponding 3-day images. First, pixels contaminated by rain were removed, this is necessary because the transient nature of rain could cause different brightness temperatures to exist. For other geophysical parameters (e.g., sea surface temperature, wind speed and water vapor) the mean values over the 3-day period were expected to be the same for both ascending and descending orbits; therefore the brightness temperatures should likewise be nearly constant. Next, a conservative land flag was used to remove data contaminated by land due to the poor spatial resolution of the SeaWinds antenna.

Finally, to reduce the measurement standard deviation, zonal averages (over longitude) were performed over quarter degree latitude bins, to form a latitude series. Results are presented for H-pol in Fig. 2.6.

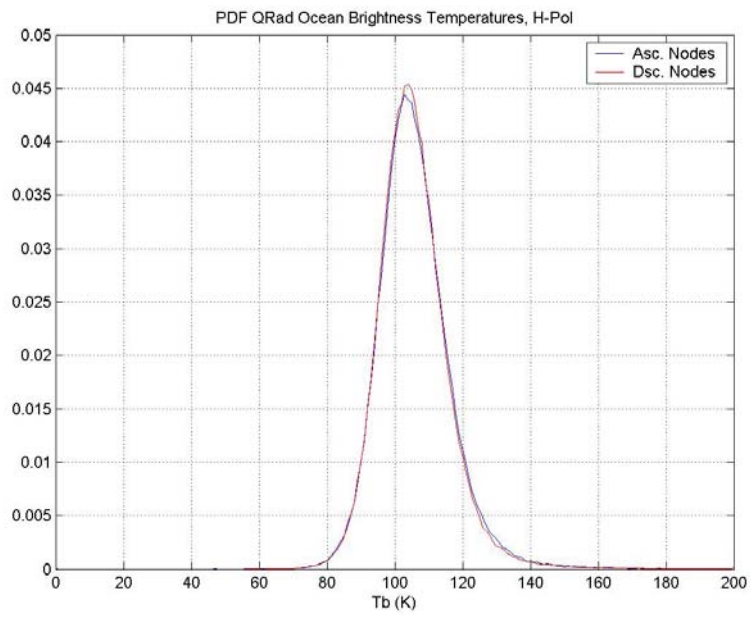


(a) H-Pol

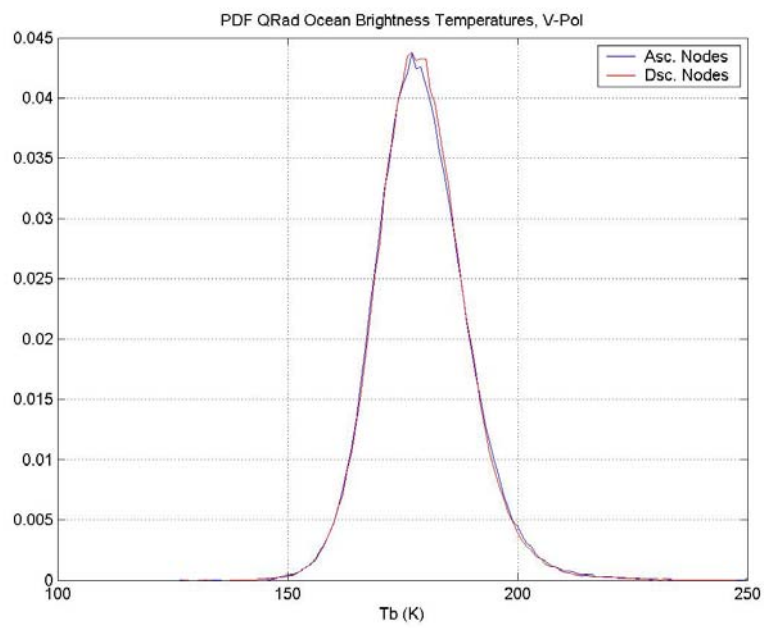


(b) V-Pol

Figure 2.4. SRad ocean Tb histograms - ascending (blue) and descending (red) orbit segments.

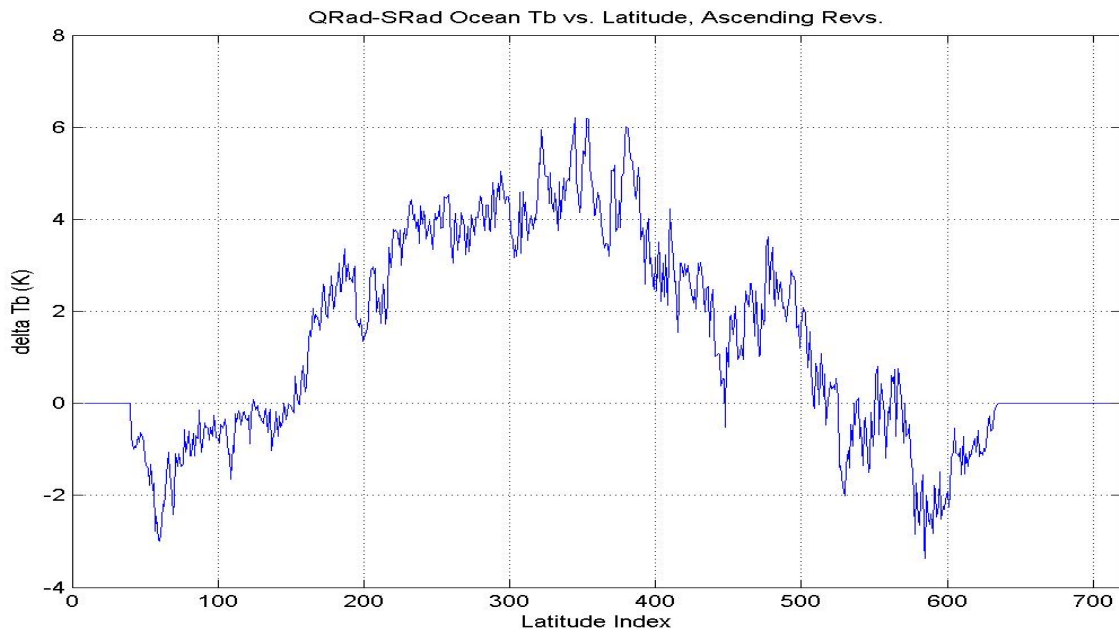


(a) H-Pol

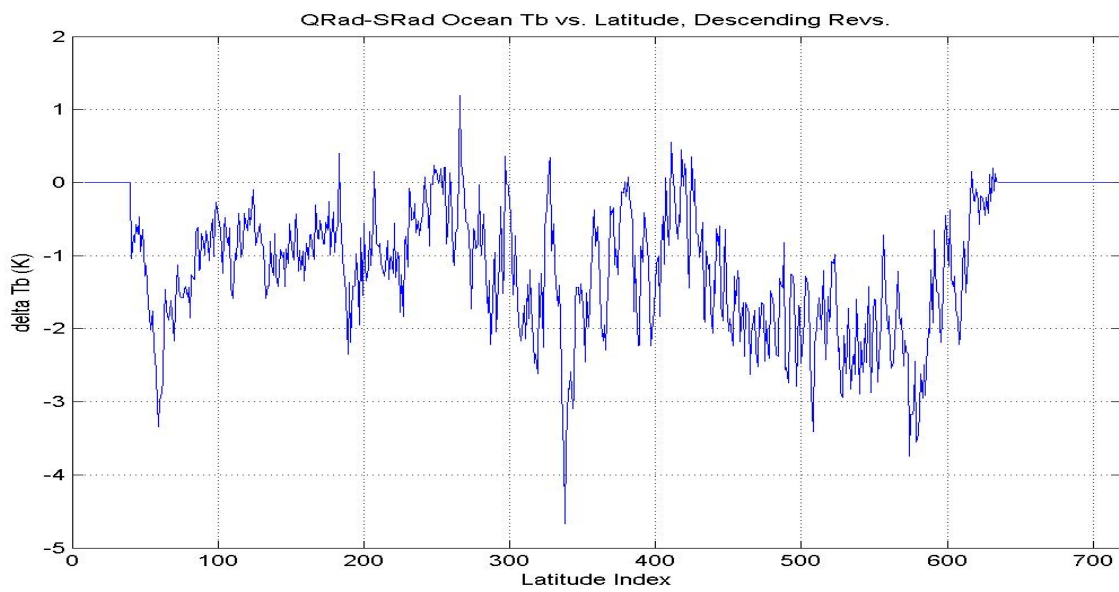


(b) V-Pol

Figure 2.5. QRad ocean Tb histograms - ascending (blue) and descending (red) orbit segments.



Ascending orbit segment (South to North pole)



Descending orbit segment (North to South pole)

Figure 2.6. (QRad – SRad) H-pol delta-Tb latitude series.

Thus, results from both the delta-Tb histograms and especially the delta-Tb latitude series (Fig. 2.6), lead to the same conclusion that there was a significant SRad Tb error, which was a function of the satellite position (latitude) in orbit. Obviously this effect is not geophysical; therefore the cause must be the instrument, which indicates that the QRad Tb algorithm used to process SeaWinds data does not perform adequately for ADEOS-II.

An investigation of possible causes was examined and the most plausible for this anomaly was the result of errors in modeling the instrument's on-orbit temperatures. For QuikSCAT, the satellite is usually in continuous sun light, which produces no temperature swings over an orbit. On the other hand for ADEOS, the orbit has day (descending) and night (ascending) segments, which produce large temperature excursions (cooling) on the dark side of the orbit. Because the physical temperature of the front-end losses is not measured, there are most likely significant errors introduced by the modeled orbital pattern of physical temperature. For the night half of the orbit, the front-end losses experience a strong temperature drop due to infrared radiation cooling, and this temperature transient is not adequately modeled in the SRad Tb algorithm [12].

The next chapter describes the SRad Tb radiometric calibration approach and the procedure followed for generating the empirical correction to remove the SRad ascending/descending Tb error discussed above.

CHAPTER 3

SRad Tb RADIOMETRIC CALIBRATION

3.1 Radiometric Calibration Approach

To correct the ascending/descending anomaly discussed in Chapter 2, the Advanced Microwave Scanning Radiometer (AMSR) was used as a brightness temperature standard to calibrate SRad, while both instruments simultaneously measured collocated ocean microwave emissions. AMSR is a well-calibrated multi-frequency, dual-polarized microwave radiometer that also operates on ADEOS-II; and therefore, AMSR Tb's are spatially and temporally co-registered with SRad. However, since the SeaWinds operates at different incidence angles (46° and 54°) and a different frequency (13.4 GHz) than the AMSR channels, the AMSR brightness temperatures are interpolated in frequency and extrapolated in incidence angle to yield an equivalent Tb comparison. Table 3.1 gives the radiometric channel's frequencies and incidence angles used in this comparison, which follows a similar procedure to that used for the QRad/TMI radiometric calibration.

The first step was to model AMSR's 10.65 GHz and the 18.7 GHz channels and the SRad 13.4 GHz channels using an ocean radiative transfer model that was tuned to match satellite Tb observations from a well-calibrated microwave radiometer, WindSat [3], which is described in the Appendix-C. A ratio of the brightness temperatures at these frequencies (and incidence angles) was calculated as a function of atmospheric water vapor (wv) and cloud liquid water (clw), and sea surface temperature (sst). This quantity, as described in (eq 2.1), called the spectral ratio is given by

$$(\textit{spectralratio}) = \frac{T_{b_{13.4}} - T_{b_{10.64}}}{T_{b_{18.7}} - T_{b_{10.65}}} \quad (3.1)$$

and was calculated separately for horizontal and vertical polarizations.

To calculate the spectral ratio, a set of 14-months of environmental parameters (e.g., sea surface temperature, wind speed, water vapor, cloud liquid, etc.) were used as input to the radiative transfer model.[3] For our calculation, the following environmental parameters were used low cloud liquid water (< 0.1mm), no precipitation, all values of sea surface temperature and water vapor, and wind speed less than 8 m/s. Figure 3.1 shows the resulting H-Pol spectral ratio versus water vapor.

The AMSR brightness temperatures were then translated to the corresponding SRad frequency/polarization using this theoretical spectral ratio and the following equation (already described in (eq 2.2)):

$$T_{b_{13.4}} = T_{b_{10.65}} + (\textit{spectralratio}) * (T_{b_{18.7}} - T_{b_{10.65}}) \quad (3.2)$$

In comparisons that follow, the SRad Tb's are compared with the Tb's calculated by this equation. This is hereafter referred to as the "AMSR equivalent brightness temperature".

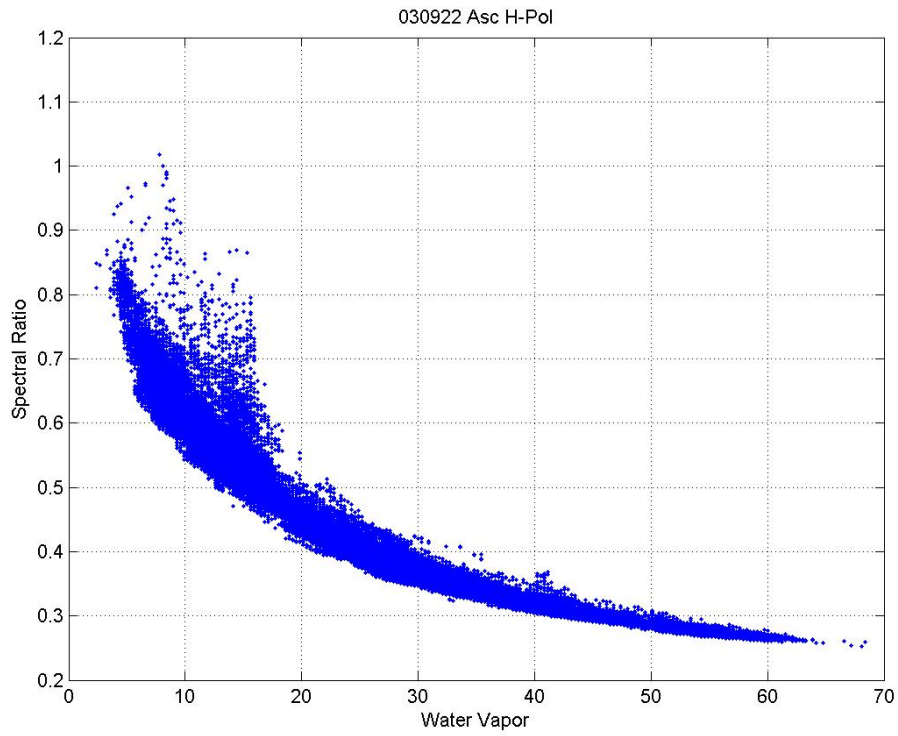


Figure 3.1 Spectral Ratio H-Pol Vs Water Vapor

Table 3.1. Frequency and Incidence angle differences for SeaWinds and AMSR

Frequency /Instrument	Incidence angle	
	H-Pol	V-Pol
SeaWinds 13.4 GHz	46 ⁰	54 ⁰
AMSR 10.65 GHz	55 ⁰	55 ⁰
18.7 GHz	55 ⁰	55 ⁰

3.2 Empirical Tb Correction

The standard SeaWinds data product Tb's (SRad L2A) exhibited a systematic Tb error that was a function of the orbit position, and this was named the ascending/descending radiometric bias. To determine this bias, the differences between SRad and AMSR equivalent Tb's were calculated for all ocean segments for nine consecutive days. After close examination of delta Tb images (shown in Fig. 3.2), it was discovered that there were large biases along the land/ocean boundaries because of "land coupling" into the SeaWinds antenna patterns. As a result, a conservative land flag was used to remove land-contaminated data as shown in Fig 3.3. The x-axis of the above figure is the latitude index where:

$$\text{latitude index} = 4 * \text{latitude}$$

$$\text{latitude} = 0-360^0; \text{ orbit latitude ascending followed by orbit latitude descending}$$

Next, these edited Tb's were zonal averaged (over longitude) to produce a latitude series of 0.25 degree bin size. Finally, the land-contaminated pixels were removed by applying the conservative land mask created above and the resulting delta-Tb's were plotted versus latitude in Fig. 3.4. From this figure, the anomalous systematic bias is clearly evident and these results are typical of those for both polarizations and for ascending and descending portions of the orbits.

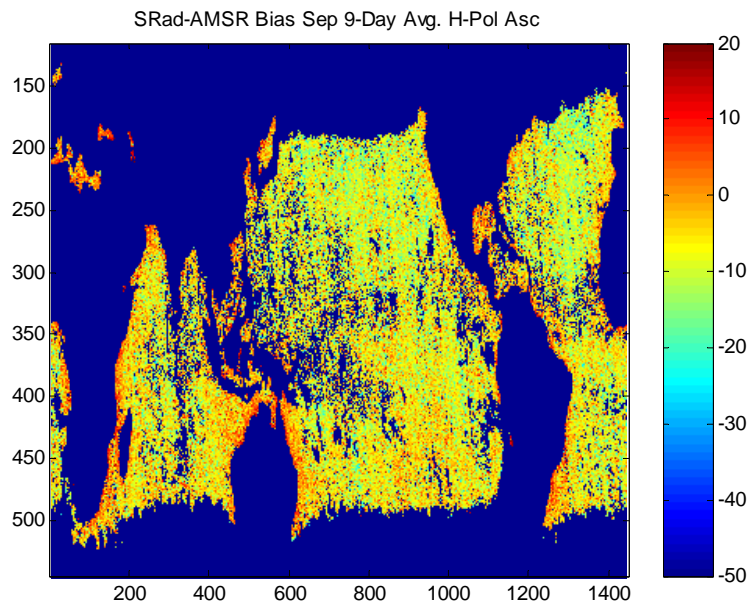


Figure 3.2. SRad-AMSR Biases along the land/ocean boundaries

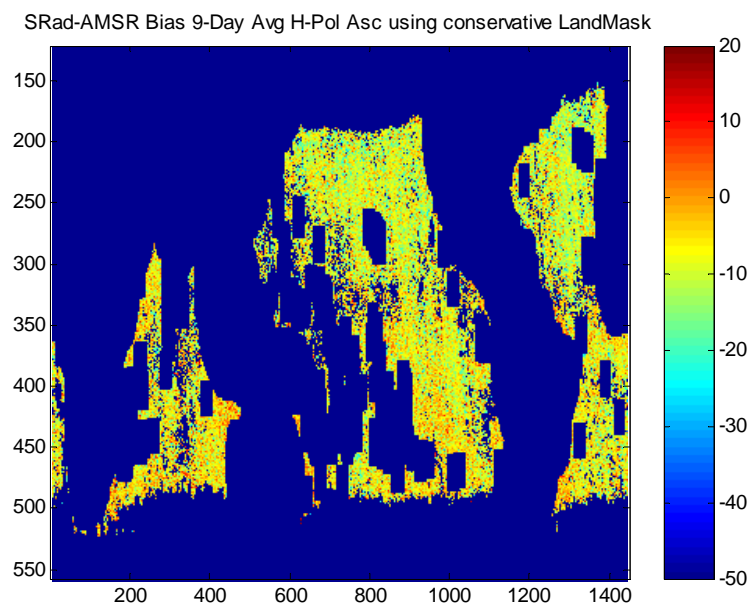
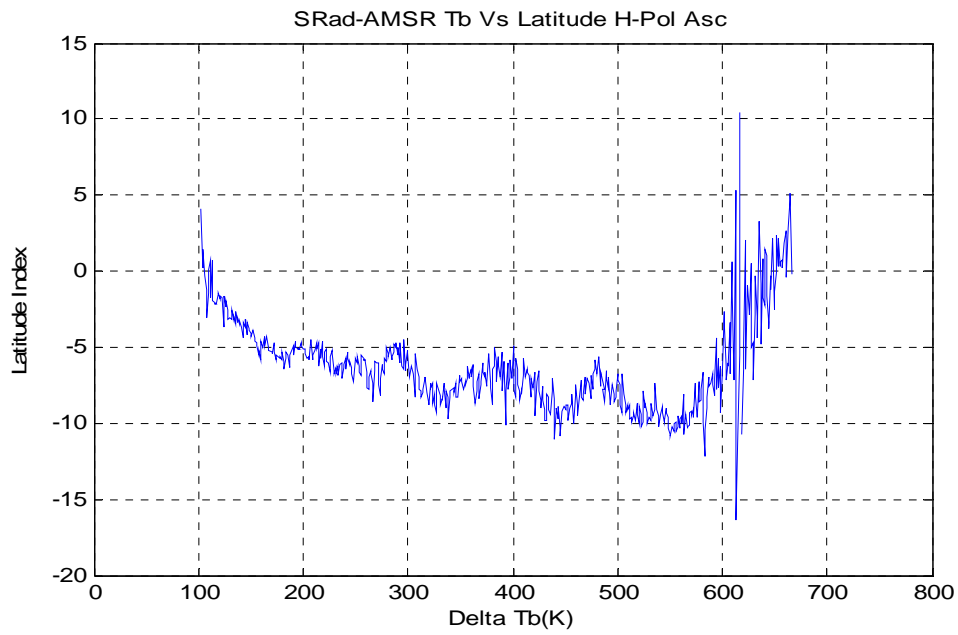
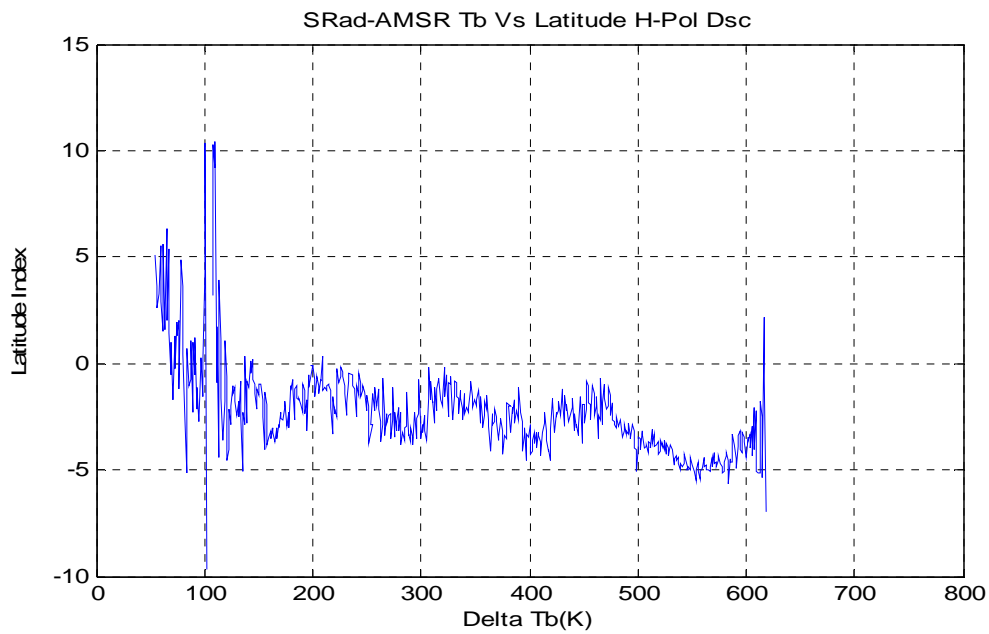


Figure 3.3. Conservative land mask to remove the land contaminated data



(a) Ascending orbit segment (South to North pole)

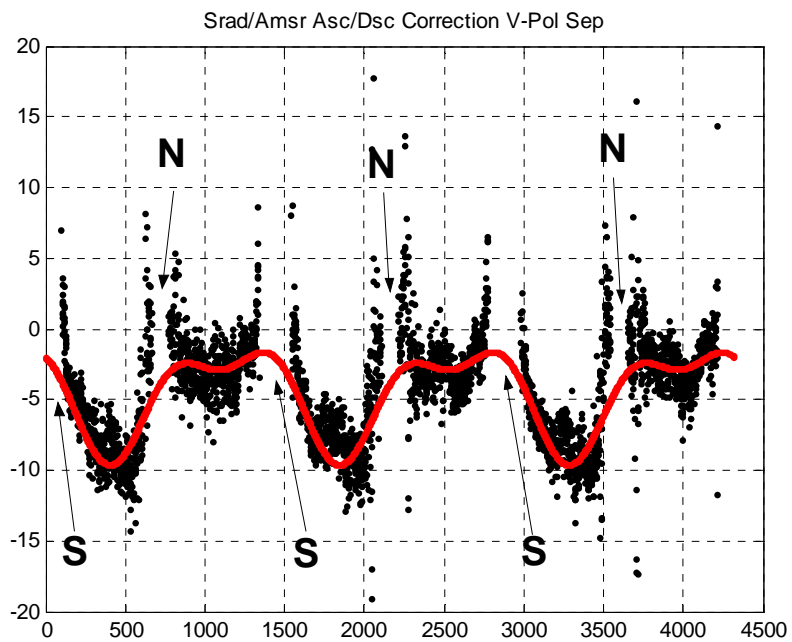


(b) Descending orbit segment (North to South pole)

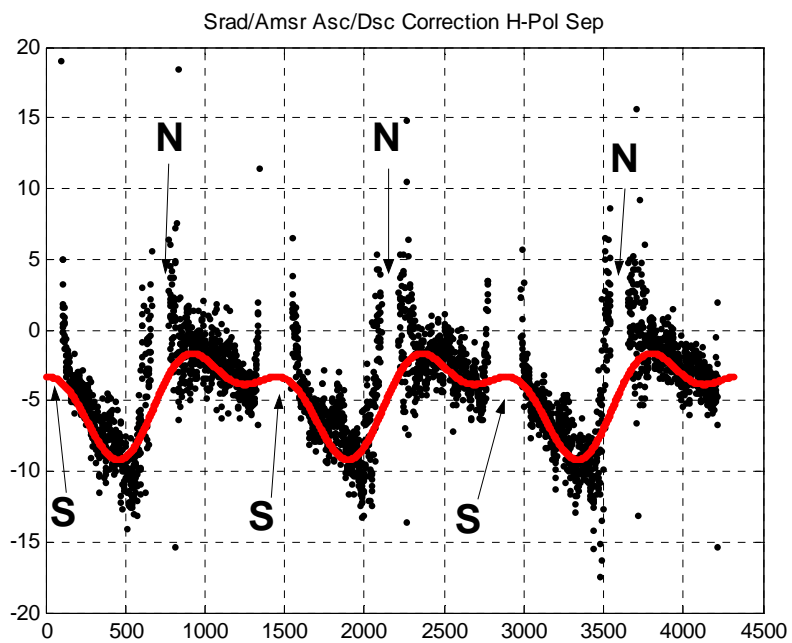
Figure 3.4 (SRad - AMSR) H-pol delta-Tb latitude series.

To develop an analytical expression for the delta Tb bias, the average orbital pattern of Tb differences between SRad and AMSR equivalent were calculated for five consecutive days. Next, a Fourier analysis was performed and the resulting orbit average pattern for the middle three consecutive days is given in Fig 3.5 with the orbit average Tb error (SRad – AMSR) in black and the Fourier series representation in red. The locations of the north (N) and south poles (S) are indicated. Two harmonics of the orbital period and a DC term were sufficient to model this systematic error. This analysis was repeated for data from all the seven months of 2003 (i.e April to October) for which the satellite and instruments were operational.

The monthly results were nearly identical, except for a phase drift which correlated with the seasonal change of the angle of the sun above (below) the equatorial plane. Figure 3.6 shows the empirical Fourier series representation of the H-Pol Tb error for a single orbit for each of the seven months. The V-Pol results are shown in Fig 3.7. The results of this Fourier analysis were applied as an additive bias to the SRad Tb algorithm as a function of latitude, which caused a very significant reduction in the magnitude of the delta Tb error. The Fourier coefficients of the empirical corrections for each of the seven months are given in Appendix B.



(a) Vertical polarization bias, K.



(b) Horizontal polarization bias, K.

Figure 3.5. (SRad – AMSR) radiometric bias (y-axis) latitude series (x-axis) for three days.

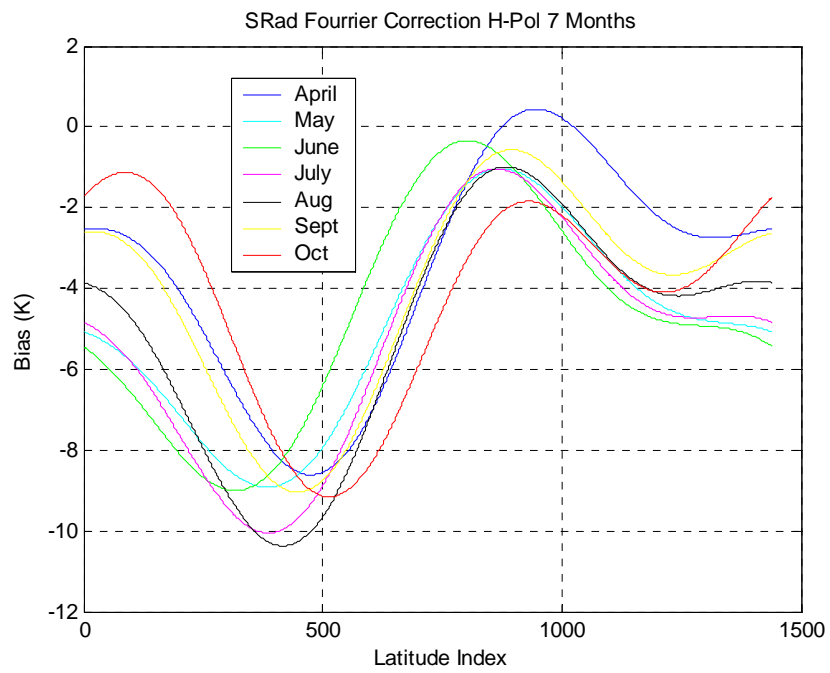


Figure 3.6. Fourier Series for seven months for H-Polarization.

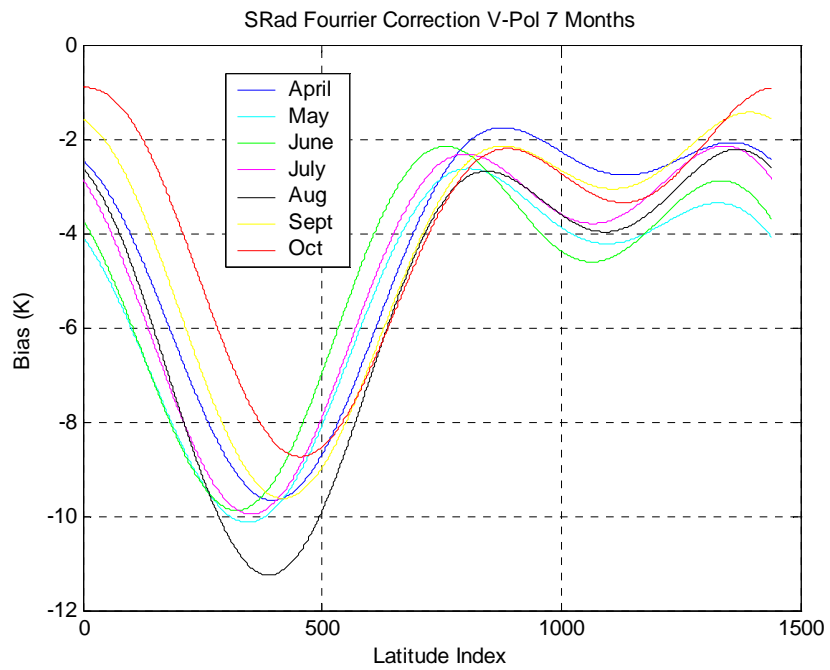


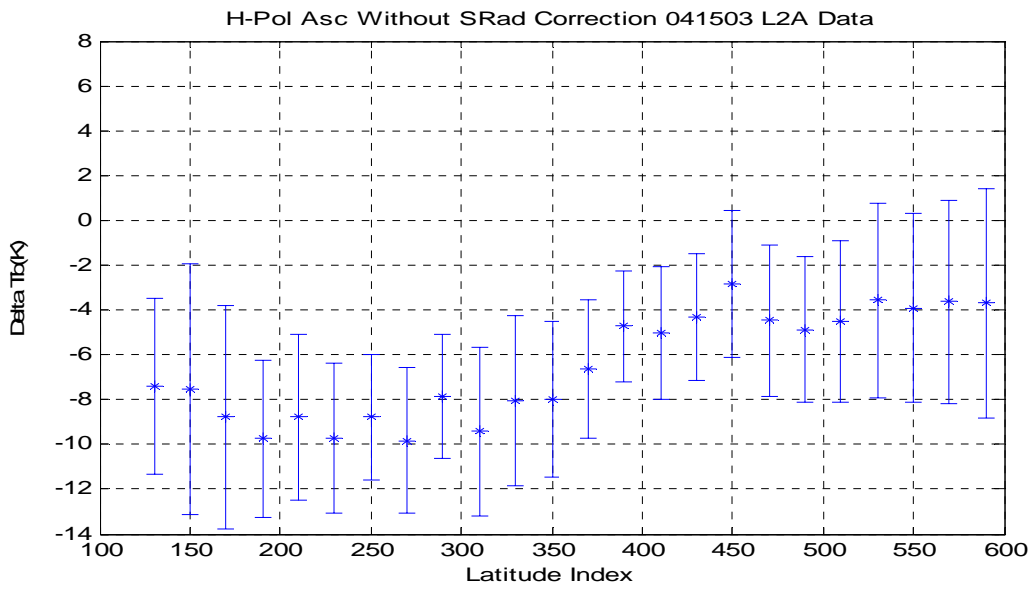
Figure 3.7. Fourier Series for seven months for V-Polarization.

Next, to achieve the goal of correcting the ascending/descending bias and to generate good quality SRad brightness temperature measurements over the oceans, the differences between SRad and AMSR equivalent Tb's were calculated. The SRad empirical correction was then applied to the SRad Tb. These comparisons were performed on the training data sets consisting of 1-day ocean Tb which were used to calculate the empirical correction.

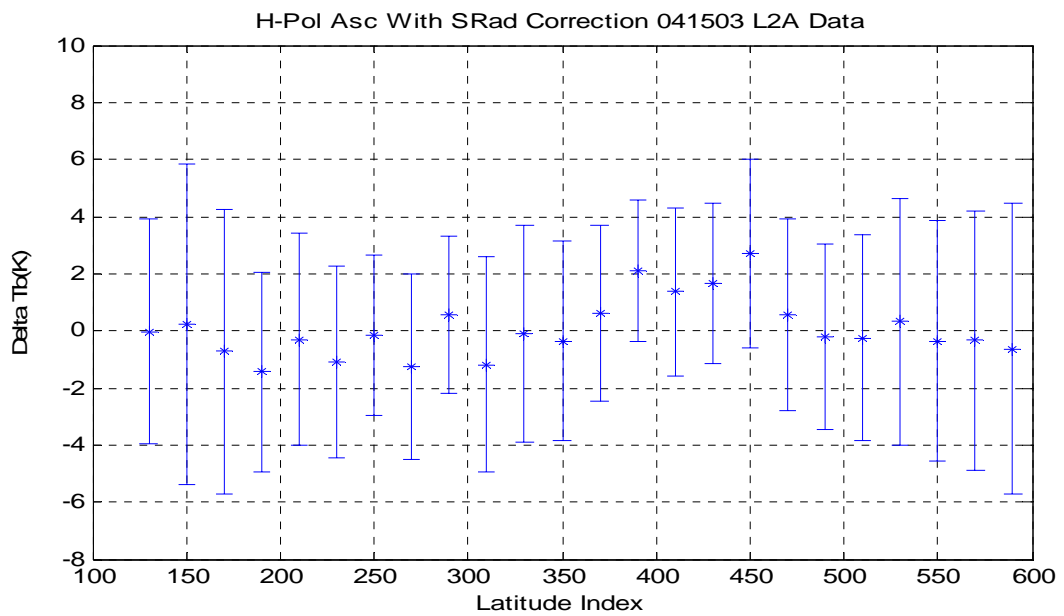
Figure 3.8 shows a typical case for H-Polarization and ascending segment where zonal averaged delta Tb's over 14 orbits (1-day) are plotted separately for (a) before applying the empirical correction and (b) after applying the empirical correction. Figure 3.9 shows similar plots for the descending segment.

The above plots shows that for the ascending orbit segment, the ocean delta Tb after applying the empirical correction had a mean value of approx 0 K with a standard deviation of approx +/- 2 K over latitude compared to a mean value of -8 K before correction. For the descending orbit segment, there was a slight improvement in the ocean delta Tb after applying the empirical correction. The above analysis was performed on different days of the training data sets and similar results were achieved.

In the next chapter, the independent validation of the revised Tb algorithm is presented through comparisons with SRad and AMSR.

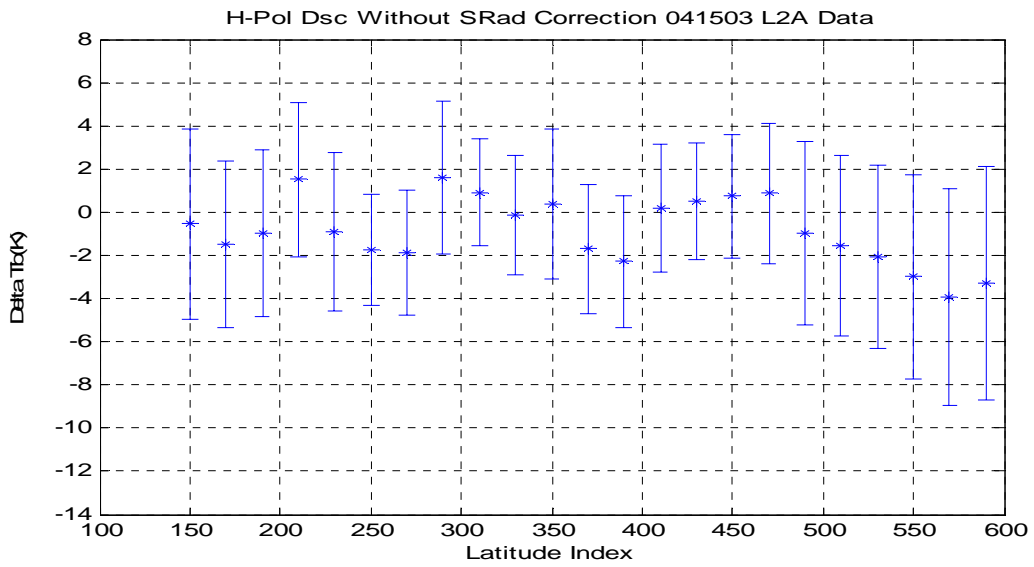


(a) before applying the empirical correction

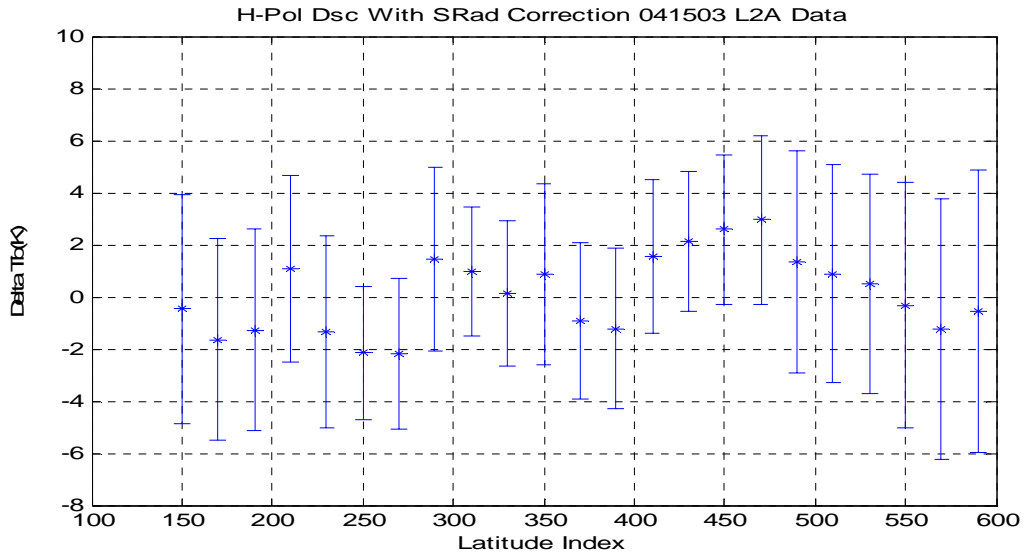


(b) after applying the empirical correction

Figure 3.8 (SRad - AMSR) H-pol delta-Tb average for ascending orbit segment.



(a) before applying the empirical correction



(b) after applying the empirical correction

Figure 3.9 (SRad - AMSR) H-pol delta-Tb average for descending orbit segment.

CHAPTER 4

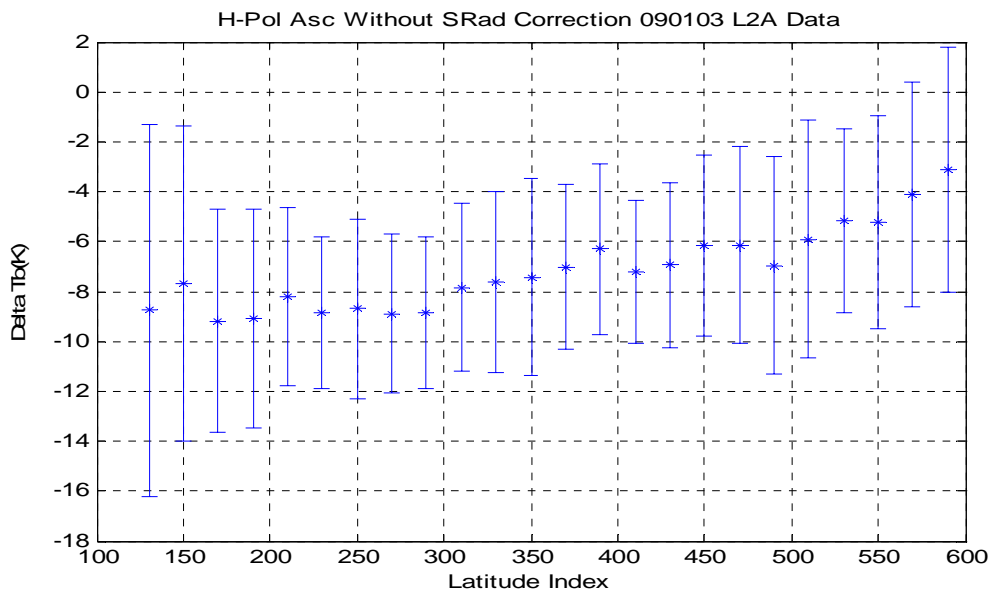
SRad BRIGHTNESS TEMPERATURE VALIDATION

This chapter presents the results of independent validation of the SRad brightness temperatures over the entire period of SeaWinds science operations for the ADEOS-II mission (approximately April – October, 2003). As explained in chapter 3, after the empirical Fourier series bias correction was developed using the seven monthly training sets, the next step was to validate the resulting “corrected” SRad Tb’s using independent AMSR comparisons. Since the empirical SRad bias correction varied by month (see Figs 3.7 and 3.8), the correction applied was linearly interpolated to the day of observation using bracketing monthly Fourier coefficients. After applying the bias correction, the SRad Tb was compared with the AMSR equivalent Tb. An example of SRad validation results are presented in this chapter and all results are summarized in Table 4.1. Further, validation comparisons for the entire 7-months are presented in the Appendix-D. These results show that, after correction, the mean ocean delta Tb bias (averaged over latitude and longitude) is < 1 K with a standard deviation of < 1.4 K. This is compared to the original delta-Tb bias (before correction) of -7 K to -9 K and a standard deviation < 2 K. It is noted that the majority of the improvement is in the reduction in the mean difference, which is reasonable given the poor delta-T of SRad. These results validate that the empirical bias adjustment performs very well in removing the ascending/descending Tb bias over the entire SRad operating period.

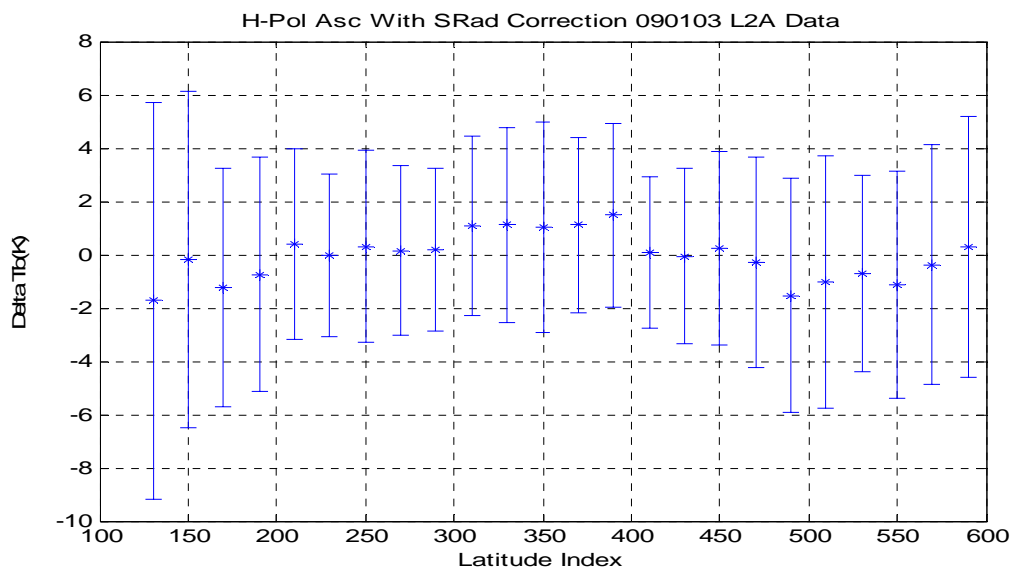
4.1 Comparison of SRad and AMSR brightness temperatures

Using an identical procedure, as described in Chap.-3, brightness temperature difference (delta-Tb) was calculated for corrected L2A SRad Tb's and AMSR equivalent Tb. For purposes of showing the improvement, the delta-Tb was calculated before and after the empirical correction was applied to the SRad Tb. This analysis was performed for data sets that were independent of the training data sets used in the SRad Tb calibration. These sets consisted of two-day ocean Tb images from beginning and end of every month over the entire period of normal SeaWinds operations (April to October, 2004), see Table 4.2.

A typical comparison case for H-polarization using one-day combined ascending orbit segments on September 1, 2003 is shown in Fig 4.1, Here data points are average delta Tb's for 15° latitude bins (a) before applying the SRad empirical correction and (b) after applying the empirical correction. Similar plots for the corresponding descending segments are shown in Fig. 4.2.

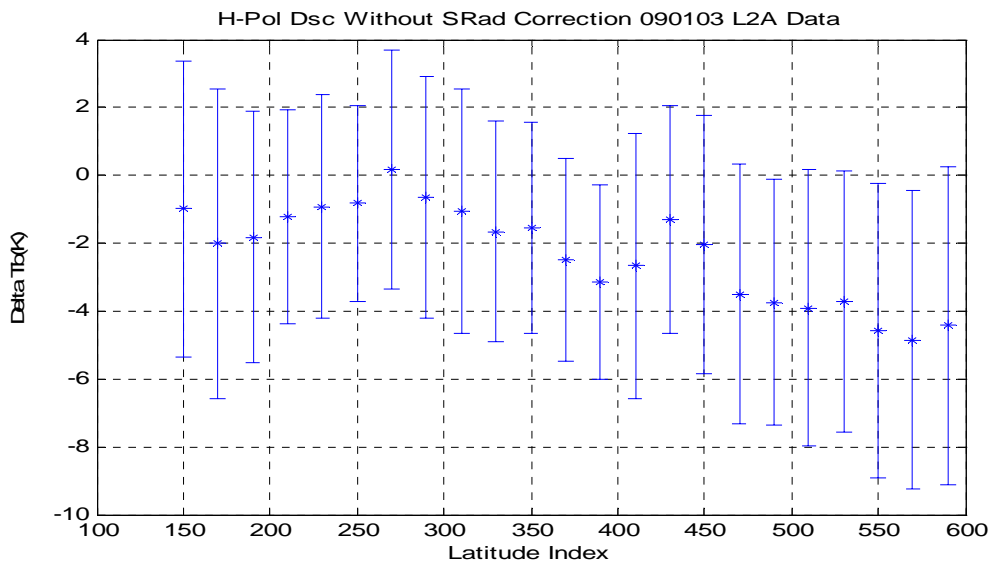


(a) Before applying the empirical correction

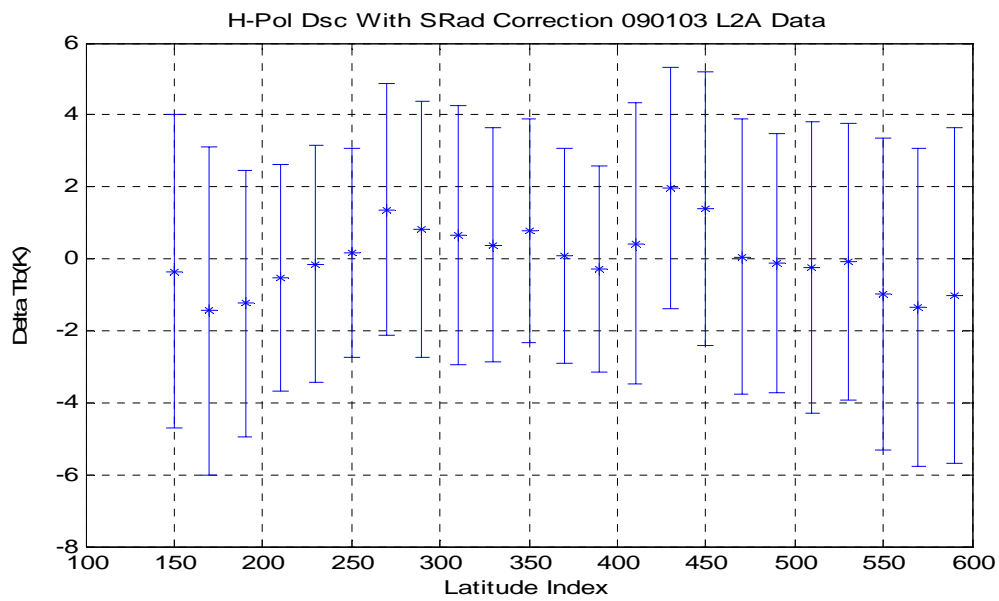


(b) After applying the empirical correction

Figure 4.1 (SRad - AMSR) H-pol delta-Tb ascending segments (Sept 1, 2003).



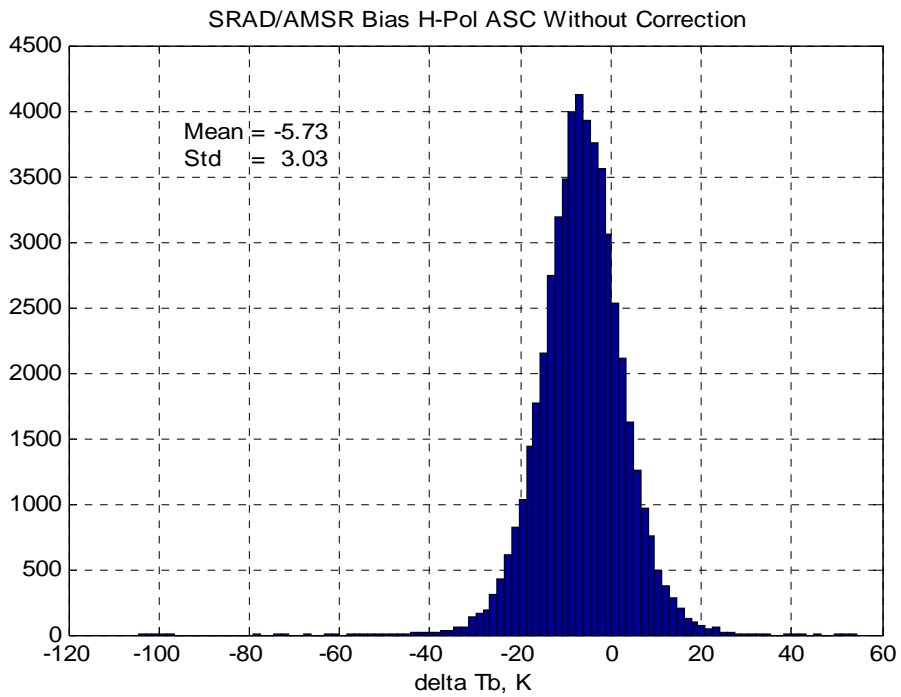
(a) Before applying the empirical correction



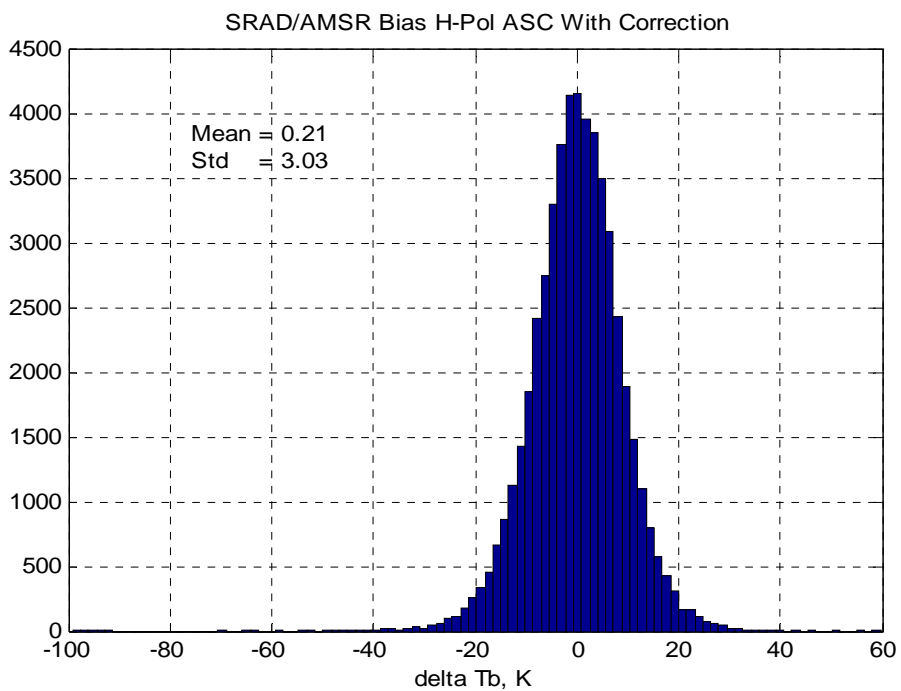
(b) After applying the empirical correction

Figure 4.2 (SRad - AMSR) H-pol delta-Tb descending segment (Sept 1, 2003).

Next, typical daily histograms of (SRad – AMSR) delta-Tb for Sept. 1, 2003 are presented for ascending and descending orbit segments and for both polarizations in Fig. 4.3 and 4.4 respectively. Similar results for V-polarization are shown in histograms in Fig. 4.5 and 4.6; and results for both are tabulated in Table 4.3. For all comparisons, the most notable change is that the bias is significantly improved (< 1 K after correction). Further, the histogram standard deviations, which are the result of the large SRad delta-T, are essentially unchanged by the empirical bias adjustment.

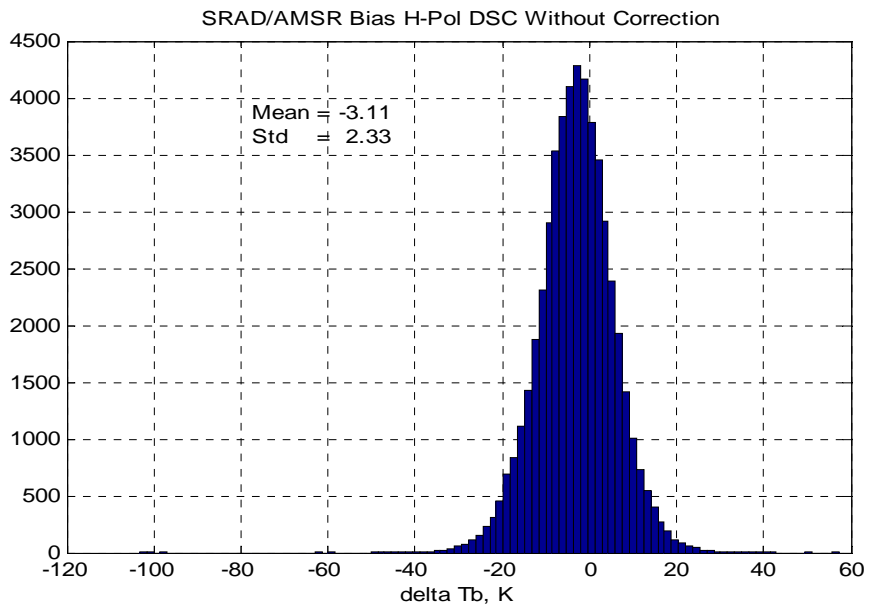


(a) Before bias correction

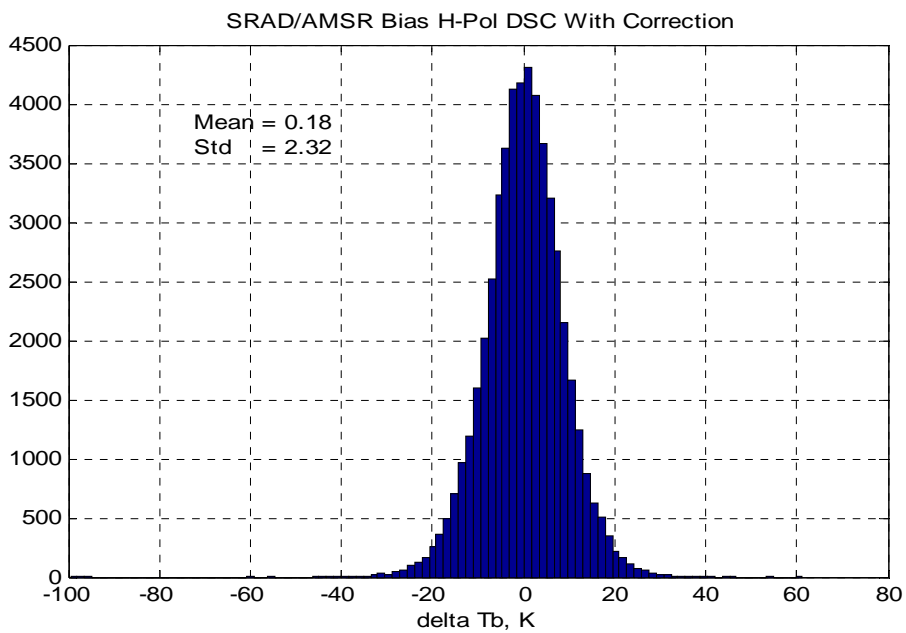


(b) After bias correction

Figure 4.3 (SRad – AMSR) H-pol delta Tb ascending segment histogram (Sept 1, 2003)

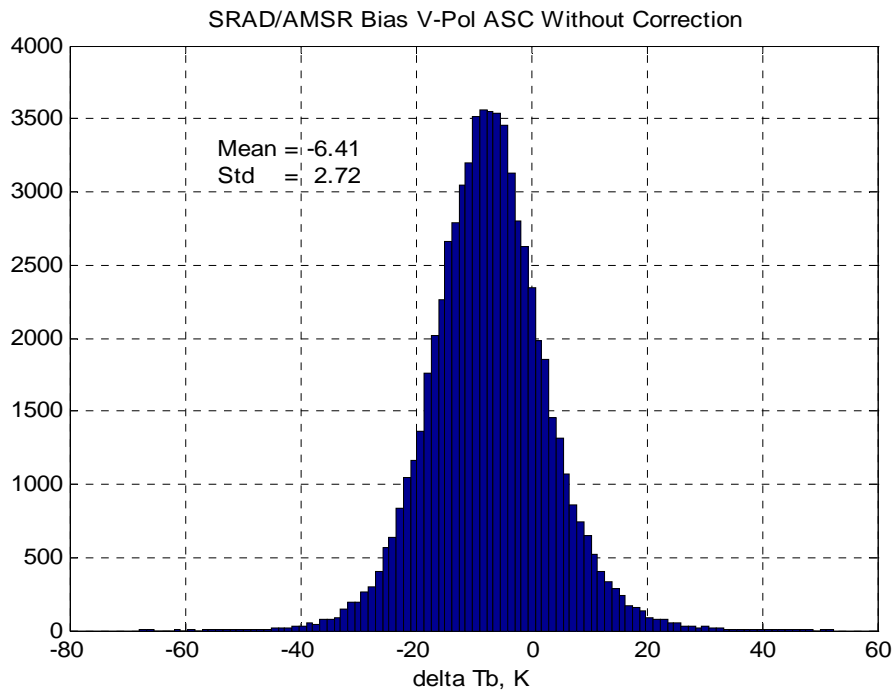


(a) Before bias correction

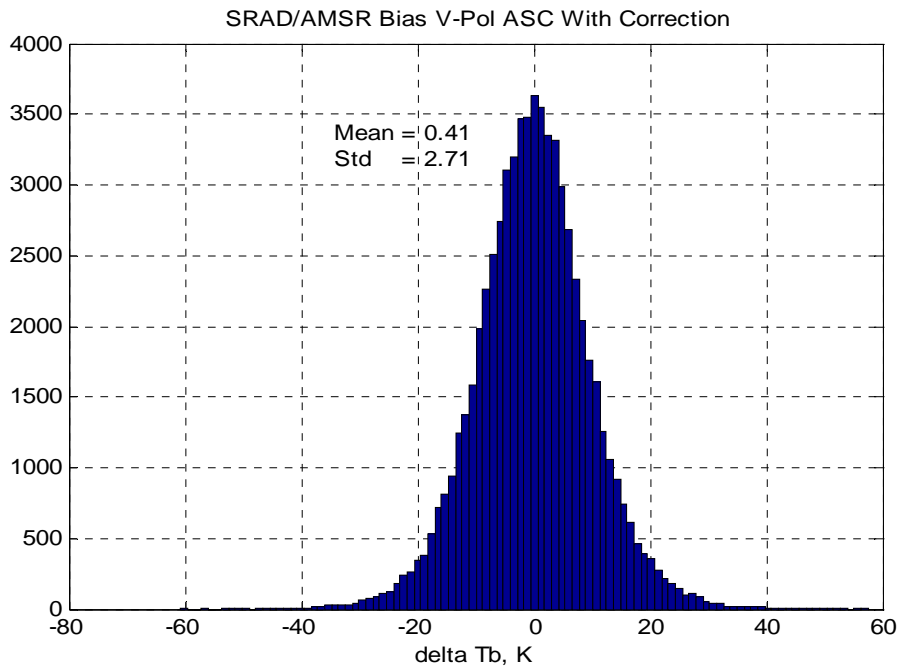


(b) After bias correction

Figure 4.4 (SRad – AMSR) H-pol delta Tb descending segment histogram(Sept 1, 2003)

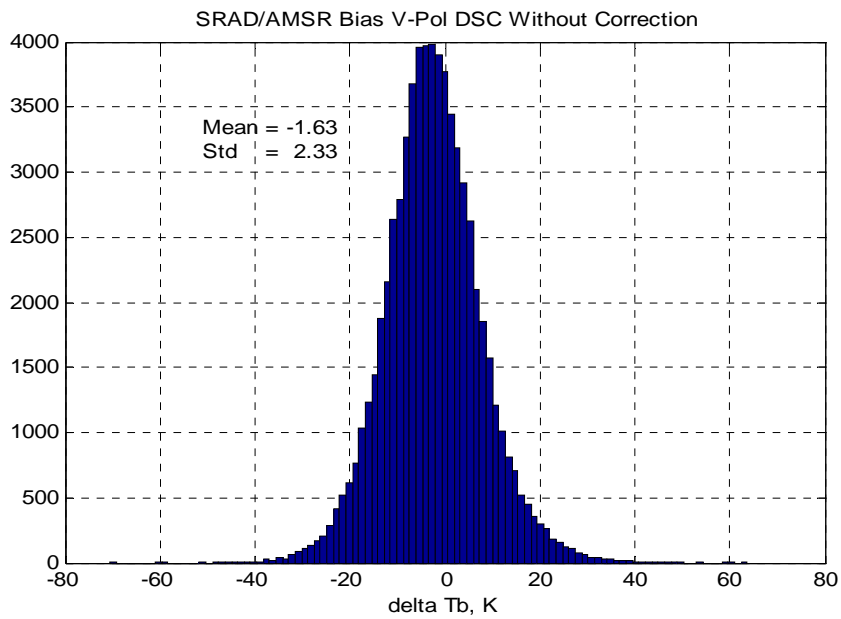


(a) Before bias correction

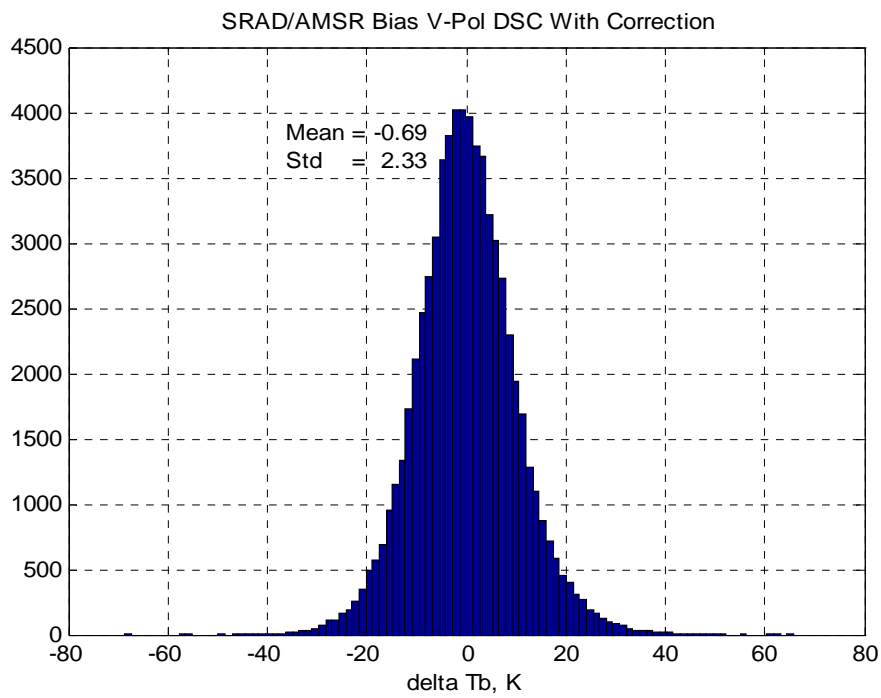


(b) After bias correction

Figure 4.5 (SRad – AMSR) V-pol delta Tb ascending segment histogram (Sept 1, 2003)



(a) Before bias correction

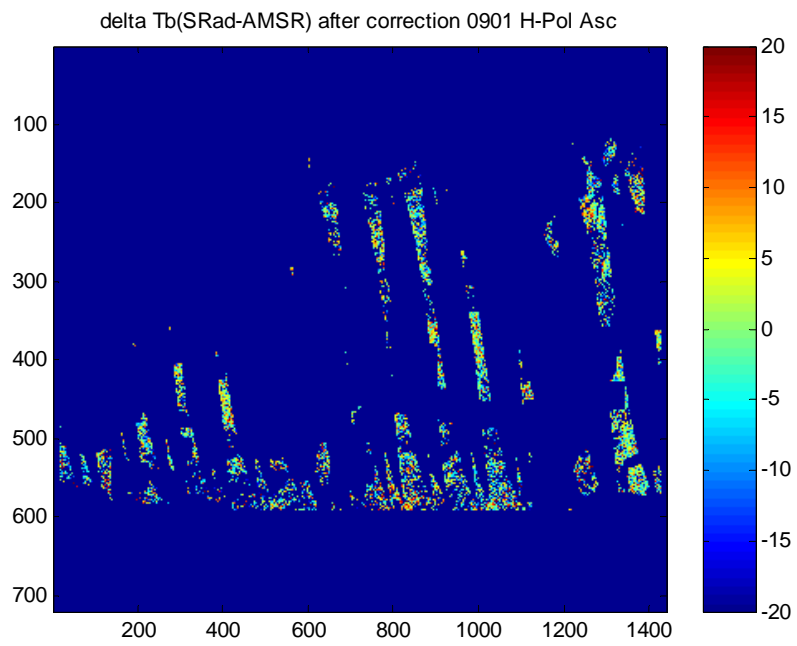


(b) After bias correction

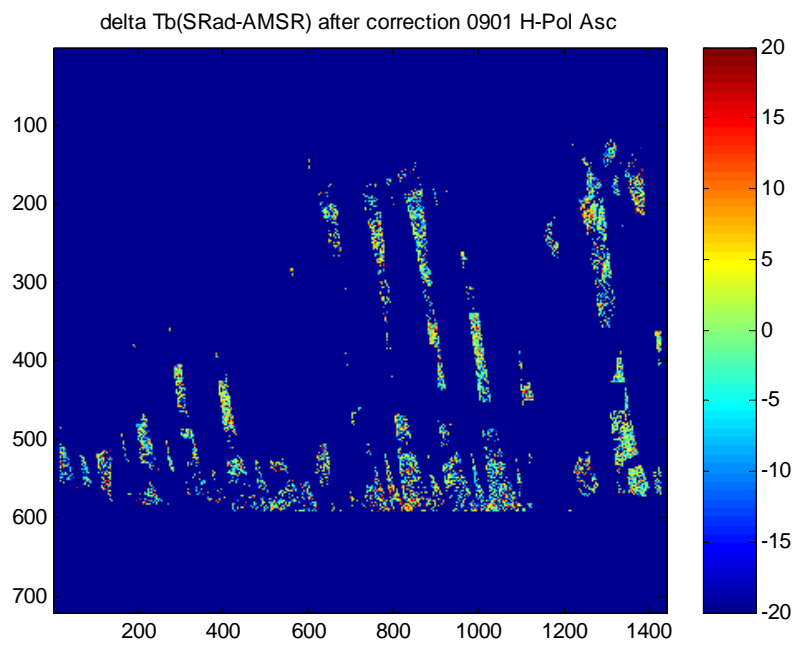
Figure 4.6 (SRad – AMSR) V-pol delta Tb descending segment histogram (Sept 1, 2003)

Finally, one-day average delta-Tb images for H- and V-pol are presented in Fig. 4.7 – 4.8 for September 1, 2003. Careful examination reveals that the delta-Tb are random and that there are no systematic biases with either latitude or longitude. Also the scatter diagram is shown in Fig. 4.9, where the data points are the binned average ocean Tb's for SRad and AMSR equivalent with a total of 243,288 points used for this comparison. These data are binned (collected) in 5 K steps for the AMSR equivalent Tb and then averages of both the SRad and AMSR equivalent Tb are performed and are plotted separately for ascending (shown in red) and descending (shown in blue) orbit segments. Data points clustered between 100 – 130 K are H-pol, and those around 180 K are V-pol. Linear regressions performed separately for ascending and descending orbit segments yield nearly unity slopes and small offsets that are tabulated in Table 4.4.

These validation results demonstrate that, on average, biases between SRad and AMSR are small < 1 K and are independent of orbit location (both latitude and longitude). Further, as shown in Appendix-D, the empirical SRad Tb corrections are equally effective over the entire 7-month period of SRad measurements.

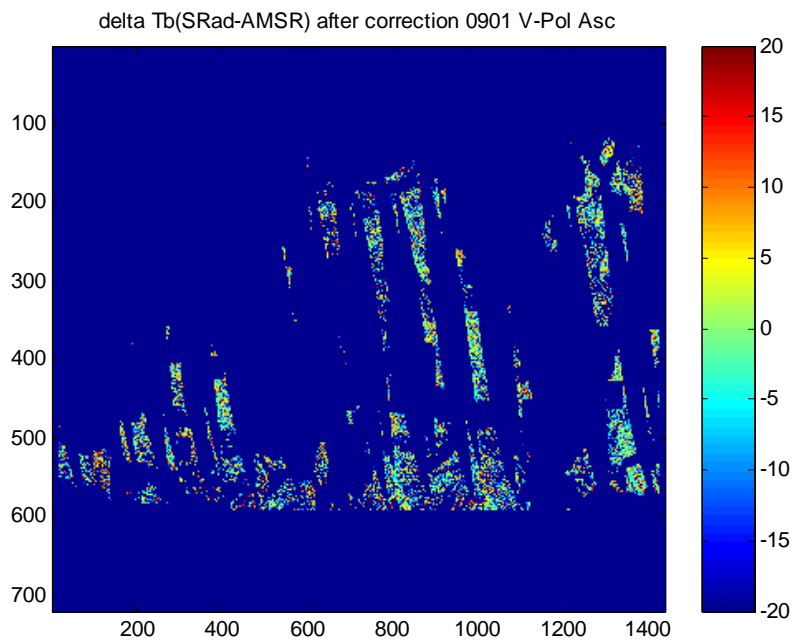


(a) Ascending Rev

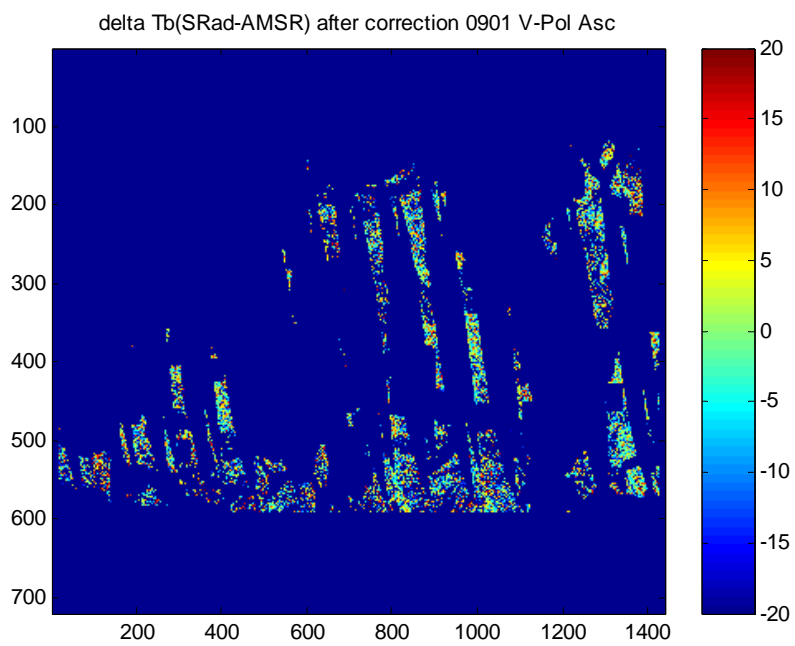


(b) Descending Rev

Figure 4.7 Delta Tb (SRad – AMSR) image after Fourier correction for H-Pol



(a) Ascending Rev



(b) Descending Rev

Figure 4.8 Delta Tb (SRad – AMSR) image after Fourier correction for V-Pol

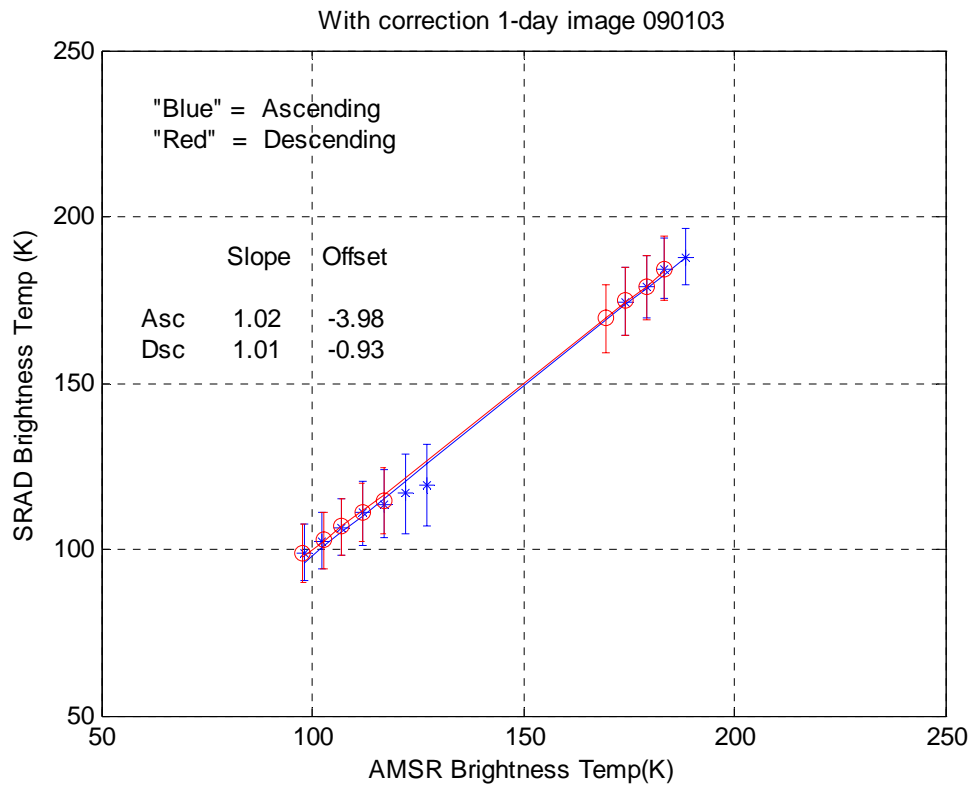


Figure 4.9 Comparison of SRad and AMSR equivalent H-pol brightness temperatures for ascending (red) and descending (blue) orbit segments

Table 4.1. SRad/AMSR overall (averaged over latitude) Mean and Std

(a) Original algorithm (before correction)

Days (2-day Avg)	Mean (K) H-Pol	Std (K) H-Pol	Mean (K) V-Pol	Std (K) V-Pol
April 30-May01	-7.65	1.48	-8.23	1.10
May 31-June01	-8.53	1.48	-8.94	1.46
June 30-July01	-8.49	1.65	-8.77	1.52
July31-Aug01	-8.89	1.57	-8.69	1.57
Aug31-Sept01	-7.45	1.23	-8.11	1.31
Sept30-Oct01	-6.78	2.39	-7.53	1.49

(b) Revised algorithm (after correction)

Days (2-day Avg)	Mean (K) H-Pol	Std (K) H-Pol	Mean (K) V-Pol	Std (K) V-Pol
April 30-May01	-0.31	1.10	0.33	0.95
May 31-June01	-0.61	1.36	-0.28	1.21
June 30-July01	-0.21	0.97	-0.32	0.75
July31-Aug01	0.004	1.20	0.40	1.09
Aug31-Sept01	0.67	0.77	0.69	0.99
Sept30-Oct01	0.13	1.13	-0.003	0.89

Table 4.2. Independent Data sets of 2-day ocean delta Tb (SRad-AMSR) used for Validation

Data Set Days (2 - day Avg)
April 30,2003 – May 01, 2003
May 31,2003 – June 01, 2003
June 30,2003 – July 01,2003
July 31,2003 – August 01,2003
August 31,2003 – September 01,2003
September 30,2003 – October 01,2003

Table 4.3 Typical SRad – AMSR Delta-Tb, Sept. 1st, 2003

(a) Original algorithm (before correction)

	Mean (K)	Std (K)	# pts
H-Pol Ascending	-5.7	3.0	52253
V-Pol Ascending	-6.4	2.7	66584
H-Pol Descending	-3.1	2.3	52031
V-Pol Descending	-1.6	2.3	67545

(b) Revised algorithm (after correction)

	Mean (K)	Std (K)
H-Pol Ascending	0.21	3.0
V-Pol Ascending	0.41	2.1
H-Pol Descending	0.18	2.3
V-Pol Descending	-0.70	2.3

Table 4.4. SRad/AMSR Linear Regression, Sept. 1st, 2003

	Slope	Offset (K)
Ascending	1.02	-3.98
Descending	1.01	-0.93

CHAPTER 5

CONCLUSIONS

This thesis describes a novel use of the SeaWinds radar scatterometer on the ADEOS-II satellite as a SeaWinds Radiometer (SRad) to obtain the ocean's microwave emissions (brightness temperature) simultaneously with ocean normalized cross section measurements. These dual active and passive microwave measurements are useful for flagging rain, which frequently contaminates scatterometer wind vector retrievals.

The ocean brightness temperature is calculated during ground data processing from simultaneous measurements of ocean backscatter and blackbody noise, which have been captured using narrow band and wideband receiver channels. A radiometric transfer function, developed for the previous SeaWinds on the QuikSCAT satellite, was also used to process SRad data. Unfortunately, differences in the on-orbit thermal environments caused erroneous results (T_b biases), which varied with the satellite's latitude position for ascending and descending orbit segments.

The objective of this thesis was to find an acceptable solution to eliminate this T_b anomaly by modifying the ground processing algorithm. The approach taken was to use another instrument on ADEOS-II, the Advanced Microwave Scanning Radiometer (AMSR), as a brightness temperature standard to calibrate SRad, while both instruments simultaneously measuring collocated ocean microwave emissions. Ocean brightness

temperature differences between SRad and AMSR equivalent Tb's were calculated, and results exhibited a systematic Tb error, called the ascending/descending bias that was a function of the orbit position (latitude). A very similar bias was evident for all the seven months of SRad data. To model this bias, an empirical three term fourier series correction versus latitude was generated for each of the seven months using 3-days of comparison data in the middle of each month. The results of this Fourier analysis were applied as an additive correction to the SRad Tb algorithm as a function of latitude, which caused a very significant reduction in the magnitude of the delta Tb error. This procedure was validated by comparing the "corrected" SRad Tb's with independent AMSR equivalent Tb's. These validation data sets consisted of two-day ocean Tb images from beginning and end of every month over the entire period of normal SeaWinds operations (April to October, 2004), see Table 4.2. These results demonstrate that, after correction, the mean ocean delta Tb bias (averaged over latitude and longitude) is < 1 K with a standard deviation of < 1.4 K. This is compared to the original delta-Tb bias (before correction) of -7 K to -9 K and a standard deviation < 2 K. It is noted that the majority of the improvement is in the reduction in the mean difference, which is reasonable given the poor delta-T of SRad. These results validate that the empirical bias adjustment performs very well in removing the ascending/descending Tb bias over the entire SRad operating period.

The results presented in this thesis will be used by the Jet Propulsion Laboratory SeaWinds project in the upcoming reprocessing of SeaWinds data (including SRad Tb's) for ADEOS-II.

APPENDIX A

QRad RADIOMETRIC TRANSFER FUNCTION

The functional block diagram for the QuikSCAT Radiometer, shown in Fig. A.1 is used to define the constants, parameters and variables used in the instrument transfer function. Functionally, the radiometer is divided into three major subsystems: Antenna Assembly, Switch Assembly and Receiver that comprise the SeaWinds Electronics Subsystem. The block diagram indicates these subsystems with their internal dissipative losses.

The SeaWinds antenna assembly consists of a parabolic dish reflector of about 1m diameter with two separate offset feeds for slightly elliptical radiation beams, and a rotary mechanical platform. The beams are incident upon the surface of the earth at 46 degrees and 54 degrees respectively for the inner and outer beams. These beams are polarized horizontal for the inner and vertical for the outer beam. In the block diagram, three losses l_1 (feed assembly), l_2 (microwave rotary joint) & l_3 (wave-guide losses) are combined and designated as l_{1A} and l_{1B} . The, A and B designation refers to the inner and outer beams respectively.

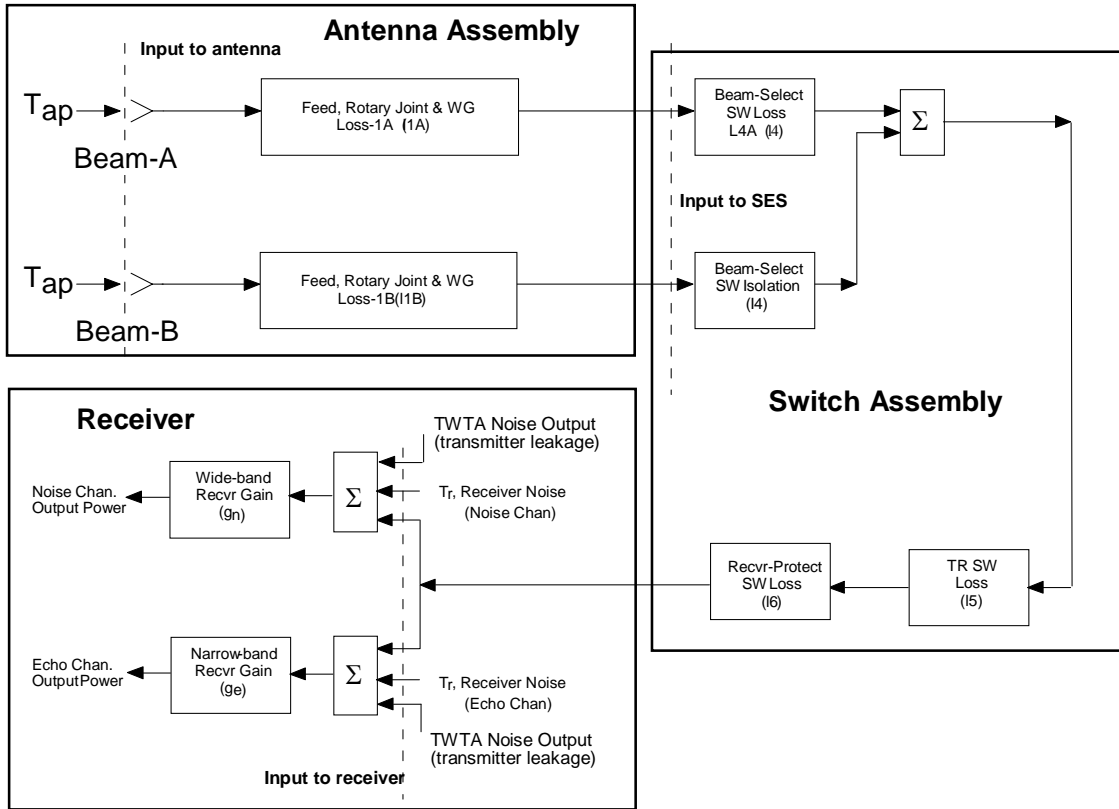


Figure A.1 QuikSCAT Radiometer Equivalent Block Diagram

The switch assembly contains of number of microwave circulator switches; beam select switch, transmit/receive switch and the receiver-protect switch indicated by losses *14*, *15* and *16* respectively.

The receiver section comprises a common low noise amplifier, frequency down-converter and intermediate frequency amplifier. After the common stages, the receiver is split into a wide-band “noise” and a narrow-band “echo” channel for digital power detection. The two channels are A/D converted and then formed by digital filters that

contain no active elements; therefore their relative gains are precisely known. For simplification, the block diagram lumps the “common gain” into each channel for a wide-band noise channel gain, g_n and a narrow-band echo channel with gain, g_e . The output of these filters is digitally power detected using a fast fourier transform and squaring of the spectral components.

The following subsections present the equations used to process QRad engineering data level L1A to level L2A, polarized microwave apparent brightness temperatures for the inner and outer antenna beams (T_{aph} and T_{apv} respectively).

A.1 Variable Definitions

Echo Energy and Noise:

E_{ei} is the sum of the 12 slice echo energies, which comprise radar echo plus noise (L1A variable “power_dn”), units are DN

where $i = “h”$ for inner beam = A and $i = “v”$ for outer beam = B

$$E_{ei} = \sum_{j=1}^{12} power_dn_j, \text{ DN} \quad (\text{A.1})$$

Excess Noise:

N_{xi} is the weighted difference between the noise channel and echo channel output energies where

$$N_{xi} = (E_{ni} - \beta * E_{ei}) * \frac{\alpha - 1}{\alpha - (1 + \varepsilon)}, \text{DN} \quad (\text{A.2})$$

i = “h” for inner beam and i = “v” for outer beam,

E_{ni} is the noise channel energy which comprise radar echo plus noise

(L1A variable “noise_dn”);

α is the mean noise channel to echo channel bandwidth ratio (calculated in L1B processing)

β is the mean noise channel to echo channel gain ratio (table input)

ε is the mod-on to mod-off noise energy ratio (table input).

Receiver Physical Temperature:

T_0 is the physical temperature of the receiver given in Fig. A.1. The value of T_0 is defined as the running average (approximately 240 frames) of the L1A variable “receiver_temp” (receiver temperature) expressed as Kelvin.

Rotary Joint and Platform Waveguide Physical Temperature:

T_1 is the physical temperature of loss-1 given in Fig. A.1. The value of T_1 is defined as the running average (approximately 240 frames) of the L1A variable “rj_temp” (rotary joint temperature) expressed as Kelvin.

Transmit/Receive Switch Physical Temperature:

T_6 is the physical temperature of losses-4, 5 & 6 given in Fig. A.1. The value of T_6 is defined as the running average (approximately 240 frames) of the L1A variable "rcv_protect_sw_temp" (receive protect switch temperature) expressed as Kelvin.

Transfer Function Parameters Definitions:

The following parameters are required for use in equations for the apparent brightness temperature. These are defined in terms of the instrument parameters given in Fig. A.1 using the equations below.

Effective or System Radiometric Temperature:

T_{eff} is the effective (system) radiometric temperature for the given antenna beam (i = h or v)

$$T_{eff} = \frac{(N_{xi} * T_{cal})}{(E_{n-cal} * (1 - 1/\alpha))}, K \quad (A.3)$$

where:

N_{xi} is the excess noise defined previously (equation A.2)

$$T_{cal} = (T_6 + T_r) / c_{eff}, K \quad (A.4)$$

c_{eff} is the "effective_load_cal_factor"

E_{n-cal} is the noise channel energy measured using the "load calibration" pulses. The value is defined as the running average for approximately 120 calibration pulses

Receiver-Protect Switch Loss:

The receiver-protect switch loss “l6” (given in Fig. A.1) is expressed as a power ratio. This loss varies with its physical temperature and is given by the following polynomial of the physical temperature, T₆. Coefficients for the polynomial are input constants (table input).

$$l6 = a_{62} * T_6^2 + a_{61} * T_6 + a_{60}, \text{ ratio} \quad (\text{A.5})$$

Transmitter Leakage Radiometric Temperature:

T_x is a constant radiometric temperature that characterizes the leakage from the transmitter. The value of T_x is approximately 2 K and is provided as an input constant (table input).

Waveguide Radiometric Bias Temperature:

T_{wg} is the radiometric bias temperature contributed by the losses between the antenna and the receiver input; where losses-1, 4, 5 & 6 are the losses given in Fig. A.1. Loss values are input constants (table inputs). For beam-A, h-pol:

$$T_{wgh} = l6 * [(1-l1A) * T_1 * l4 * l5 + (1-l4) * T_6 * l5 + (1-l5) * T_6] + (1-l6) * T_6, \text{ K} \quad (\text{A.6})$$

And for beam-B, v-pol:

$$T_{wgv} = l6 * [(1-l1B) * T_1 * l4 * l5 + (1-l4) * T_6 * l5 + (1-l5) * T_6] + (1-l6) * T_6, \text{ K} \quad (\text{A.7})$$

Receiver Noise Figure and Noise (Radiometric) Temperature:

The receiver noise figure ratio is “nf”. This is expressed as a polynomial of the receiver physical temperature T_0 by the following equation:

$$nf = 10 \exp[a_{r1} * T_0 + a_{r0}], \text{ratio} \quad (\text{A.8})$$

where:

polynomial coefficients are input constants (table inputs)

And the receiver radiometric temperature, T_r , is

$$T_r = (nf - 1) * T_{nf-ref}, \text{K} \quad (\text{A.9})$$

where:

T_{nf-ref} is the noise figure reference temperature that is a table input (= 290 K)

A.2 Other Terms

X-factor:

There are separate “X-factors” for each antenna beam. Instrument parameters are table inputs.

$$X_A = l1A * l4 + l1B * l4, \text{ratio} \quad (\text{A.10a})$$

$$X_B = l1B * l4 + l1A * l4, \text{ratio} \quad (\text{A.10b})$$

D-factor:

There are separate “D-factors” for each antenna beam, where del-T_A & T_B , $l1A$ & B , and $I4$ are input constants (table input).

$$D_A = \text{del}T_A * l1B * I4, \text{ Kelvin} \quad (\text{A.11a})$$

$$D_B = \text{del}T_B * l1A * I4, \text{ Kelvin} \quad (\text{A.11b})$$

Y-factor:

There are separate “Y-factors” for each antenna beam.

$$Y_A = (1 - l1B) * T_1 * I4, \text{ Kelvin} \quad (\text{A.12a})$$

$$Y_B = (1 - l1A) * T_1 * I4, \text{ Kelvin} \quad (\text{A.12b})$$

Z-factor:

There is only one “Z-factor” i.e., used for both antenna beams.

$$Z = l5 * l6, \text{ ratio} \quad (\text{A.13})$$

Polarized Apparent Brightness Temperature:

The polarized apparent brightness temperature is:

$$T_{aph} = \frac{C_{1A} * \left(\frac{T_{effh} - T_{wgh} - T_x - T_r}{Z} - D_A - Y_A \right)}{X_A} + C_{0A}, \text{ K} \quad (\text{A.14a})$$

$$T_{apv} = \frac{C_{1B} * \left(\frac{T_{effv} - T_{wgv} - T_x - T_r}{Z} - D_B - Y_B \right)}{X_B} + C_{0B}, \text{ K} \quad (\text{A.14a})$$

where; C1A & C1B are the correlation slopes, and C0A & C0B are the correlation offsets.

A.3 Algorithm Architecture

The apparent brightness temperature algorithm can be partitioned into three classes of calculations, namely things calculated once, things calculated using running averages, and things calculated every pulse.

Calculated only once/rev:

The following terms of the T_{api} equations are calculated only once/orbit. The inputs for these terms are read from the input parameter table.

X-factor (equations A.10a & A.10b)

D-factor (equations A.11a & A.11b)

Calculated using running-mean of approximately 240 frames:

The following terms of the T_{api} equations use physical temperatures as an input variable. Because of the relatively coarse quantization of the physical temperature measurement, it is necessary to average the physical temperatures T_0 , T_1 and T_6 for about 240 frames. This value is long compared to the pulse-to-pulse digitization period and was selected to reduce the quantization “noise”. Further, this value is short compared to the time-rate-of-change of the physical temperature over an orbit period such that effective physical temperature measurement resolution of about 0.1 K can be realized.

Receiver-Protect Switch Loss (equation A.5)

Waveguide Radiometric Bias Temperature (equations A.6 & A.7)

Receiver Noise Figure and Radiometric Temperature (equations A.8 & A.9)

Y-factor (equations A.12a & A.12b)

Z-factor (equation A.13)

T_{cal} (equation A.4)

Calculated using running-mean of approximately 120 calibration pulses:

The noise channel energy load calibrate (DN) is derived from the load calibration pulses that occur at a period of slightly greater than every three frames. To estimate the mean value, the noise channel energy must be calculated using a running average of 120 load calibration pulses.

Noise Channel Energy, E_{n-cal} , (used in equation A.3)

Calculated using running-mean of approximately 800 calibration pulses:

The mean noise channel to echo channel bandwidth ratio (α) is calculated in L1B using the running average of 800 load calibrate pulses.

Calculated every pulse:

The following terms of the T_{api} equations are calculated every pulse except for calibrate (loop-back and load measurements).

Echo Energy

Sum of 12 slice DN's (equation A.1)

Excess Noise Energy (equation A.2)

Effective Radiometric Temperature (equation A.3)

Polarized apparent brightness temperature (equations A.14a & A.14b)

APPENDIX B

SRad FOURIER CORRECTION COEFFICIENTS

Table B.1. Fourier Coefficients of SRad Empirical Correction, H-Pol

	A0	A1	A2	B1	B2
April 2003	-7.14	0.57	0.48	-3.38	1.84
May 2003	-9.87	-1.15	1.02	-2.90	0.98
June 2003	-9.97	-1.87	1.32	-2.62	0.43
July 2003	-10.52	-1.01	1.43	-3.29	1.07
August 2003	-10.15	-0.23	1.44	-3.51	1.42
September 2003	-8.29	0.31	1.22	-2.91	1.74
October 2003	-8.44	1.82	0.67	-1.81	2.30

Table B.2. Fourier Coefficients of SRad Empirical Correction, V-Pol

	A0	A1	A2	B1	B2
April 2003	-8.99	0.46	1.59	-3.42	0.62
May 2003	-10.78	-0.47	1.77	-2.95	-0.78
June 2003	-10.16	-0.72	2.08	-2.57	-0.55
July 2003	-9.69	-0.03	2.02	-3.08	-0.16
August 2003	-10.82	0.64	2.15	-3.59	0.47
September 2003	-8.83	1.11	1.73	-3.12	0.83
October 2003	-8.03	1.58	1.52	-2.30	1.29

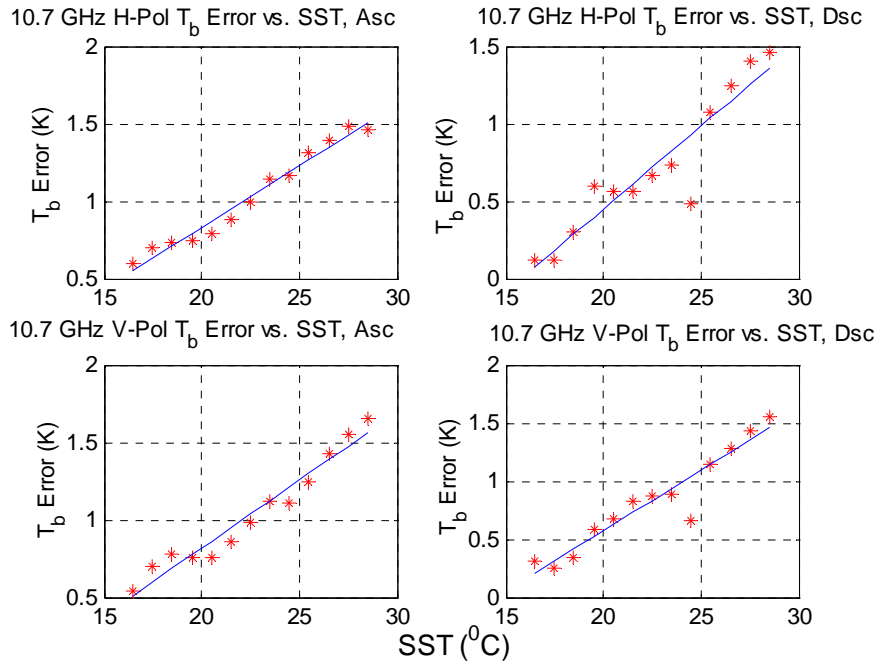
APPENDIX C

ADEOS-II AMSR BRIGHTNESS TEMPERATURE CALIBRATION

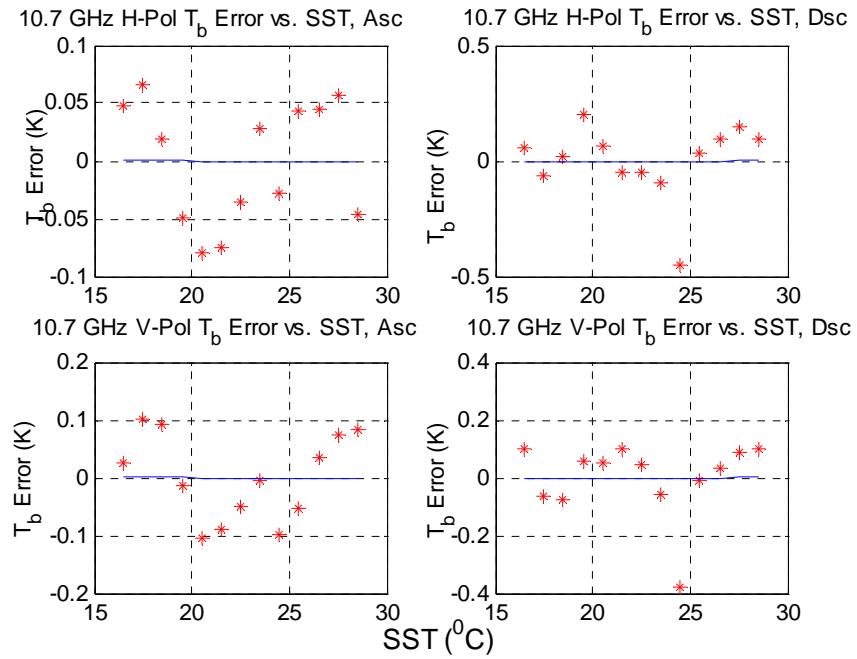
C.1 RadTb Tuning using WindSat

As described in section 3.1, before the radiometric channels of AMSR and SRad could be modeled using the radiative transfer model, RadTb, it was necessary that it be “tuned” (validated) using satellite Tb observations from a well-calibrated microwave radiometer named WindSat. During the previous work performed at CFRSL by Thompson [3], it was determined that the model dependence on sea surface temperature and wind speed needed adjustment. A modeling correction was applied for both these environmental parameters and the results indicated that the RadTb comparisons with WindSat were less than about ± 0.5 K.

Figure C.1 – C.6 the plots of the Tb error versus different environmental parameters before and after the correction to wind speed and sea surface temperature were applied. For AMSR comparisons presented next, we used low cloud conditions (integrated cloud liquid < 0.1 mm) and low to moderate wind speeds (< 8 m/s) and all SST's.

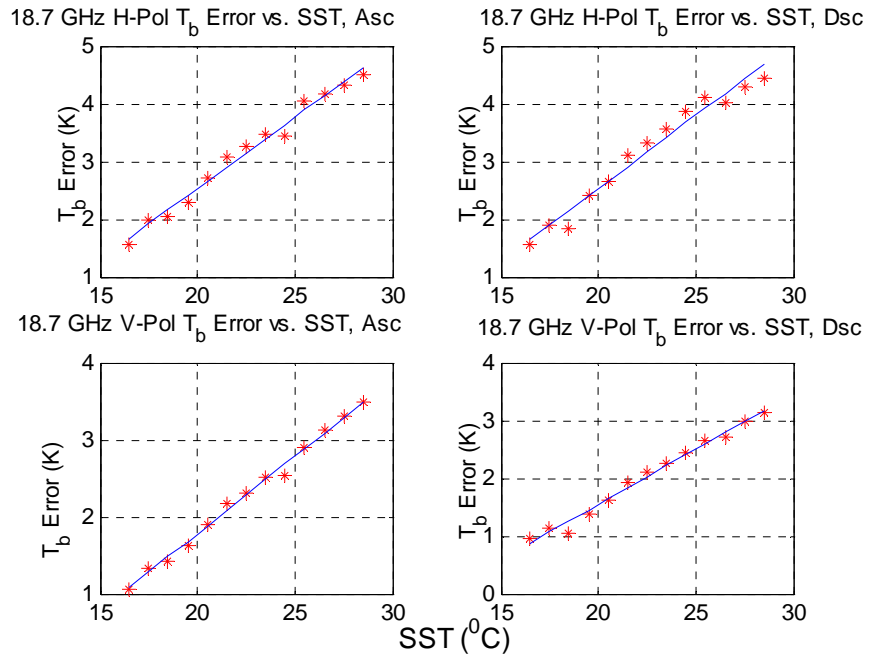


(a) before ws and sst correction

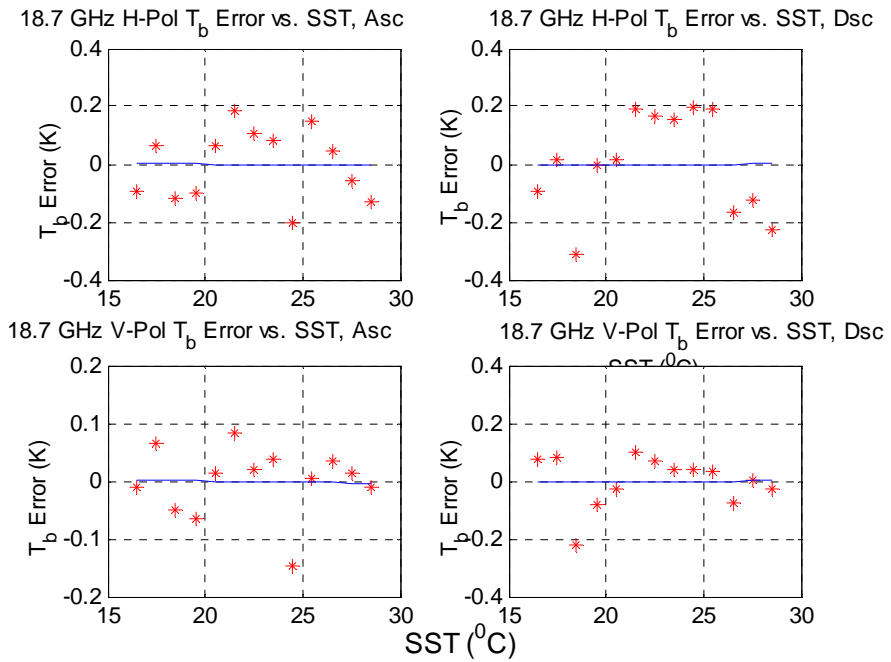


(b) after ws and sst correction

Figure C.1 Brightness Temperature Error Vs Sea Surface Temperature, 10.7 GHz

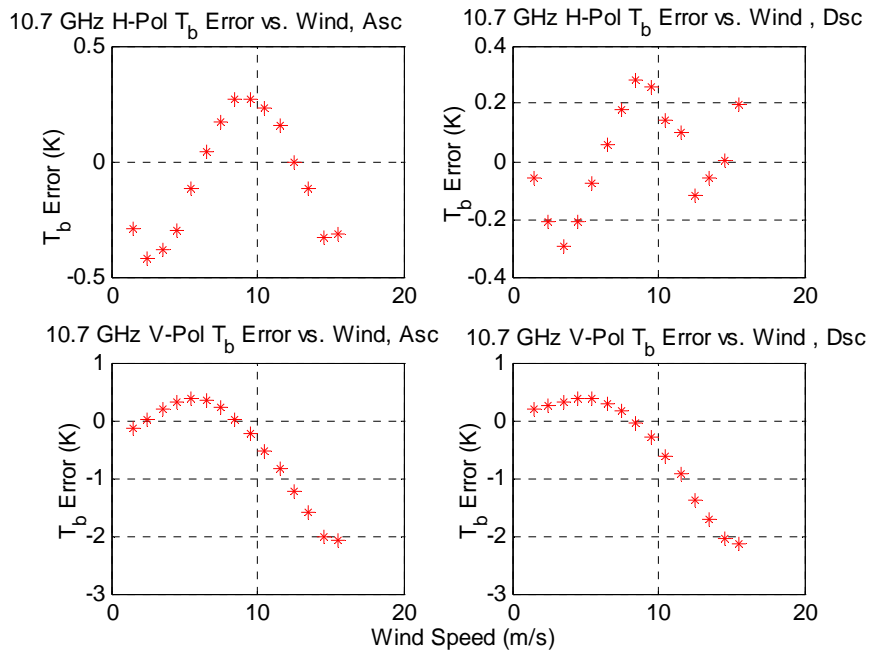


(a) before ws and sst correction

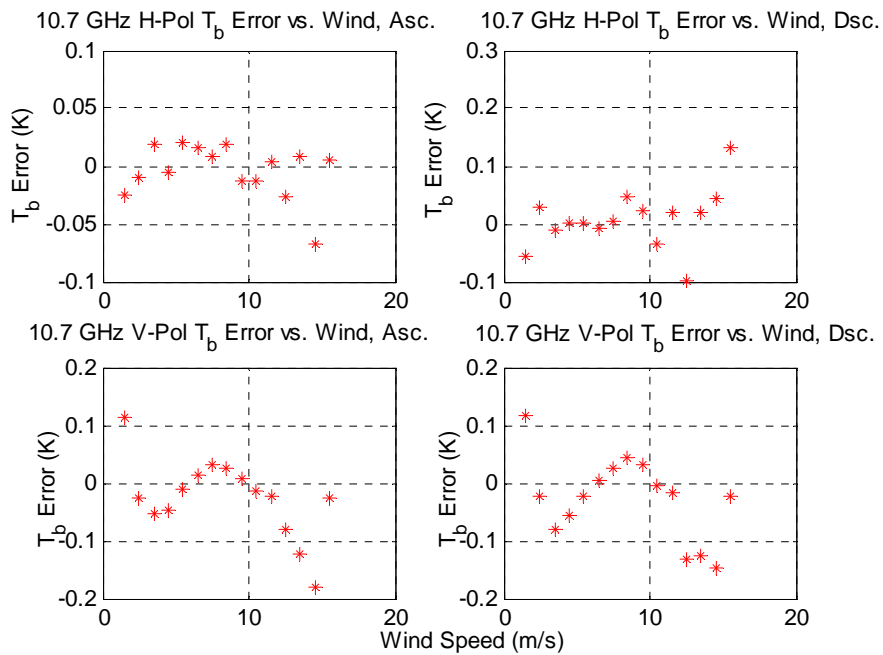


(b) after ws and sst correction

Figure C.2 Brightness Temperature Error Vs Sea Surface Temperature, 18.7 GHz

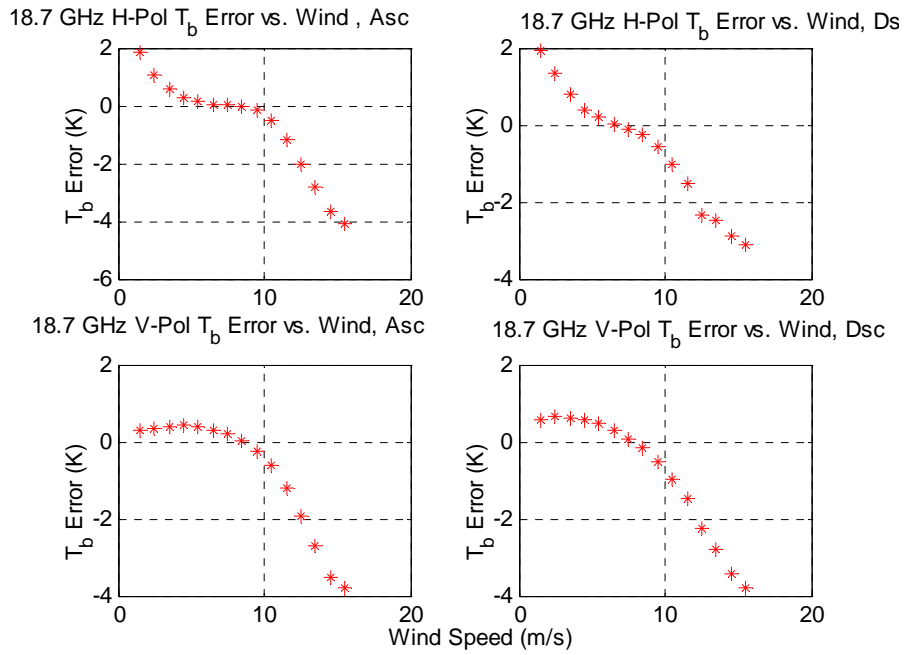


(a) before ws and sst correction

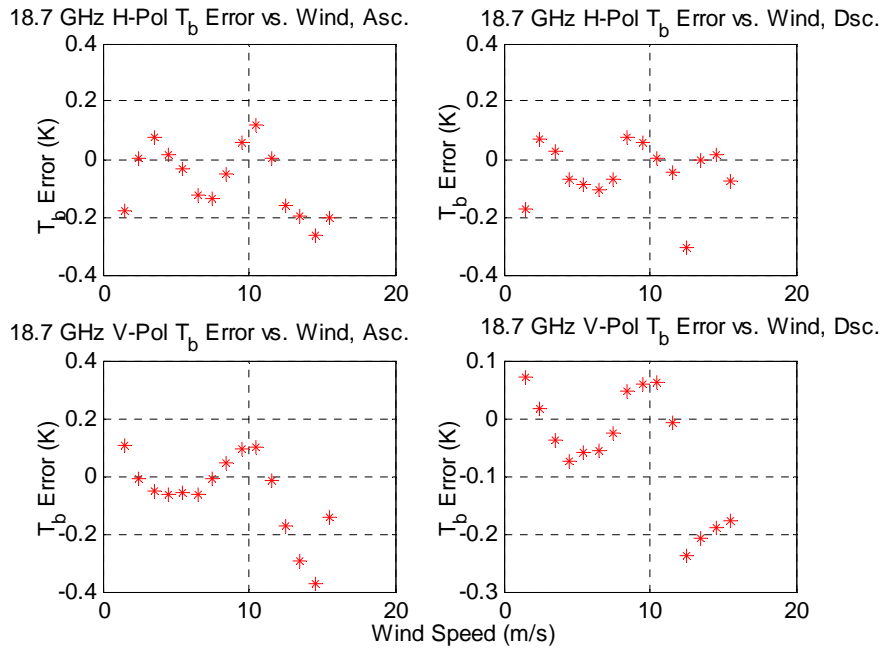


(b) after ws and sst correction

Figure C.3 Brightness Temperature Error Vs Wind Speed, 10.7 GHz

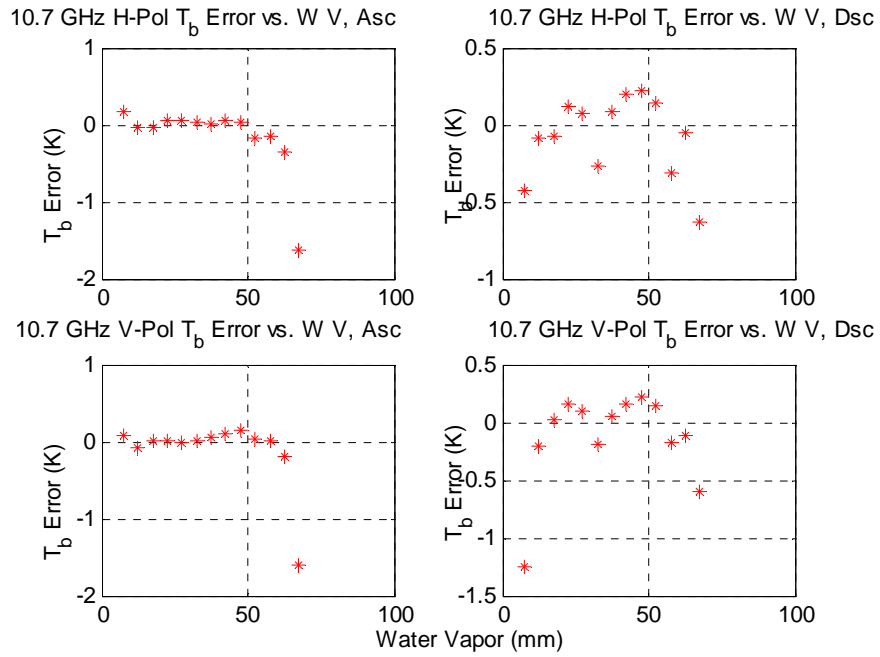


(a) before ws and sst correction

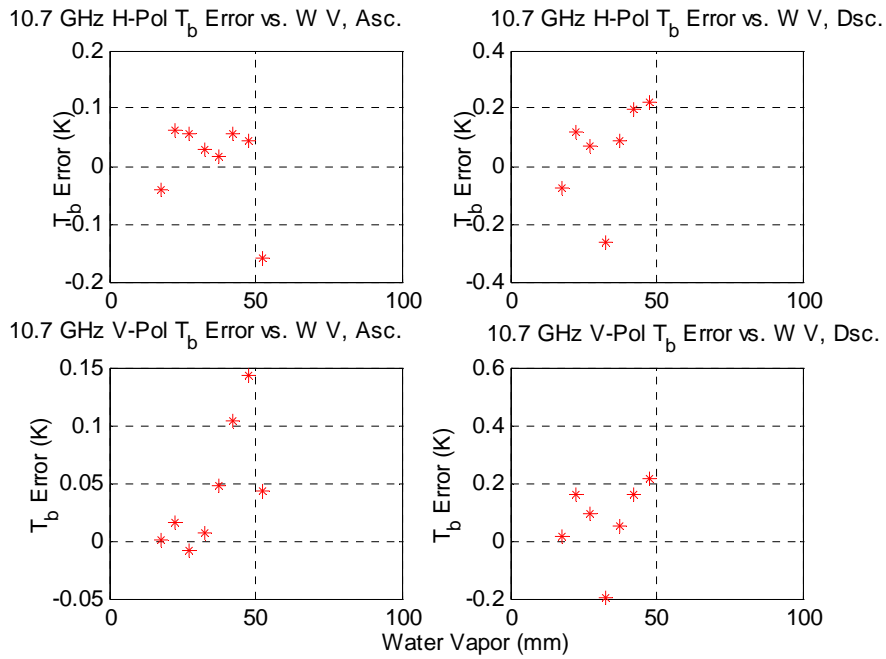


(b) after ws and sst correction

Figure C.4 Brightness Temperature Error Vs Wind Speed, 18.7 GHz

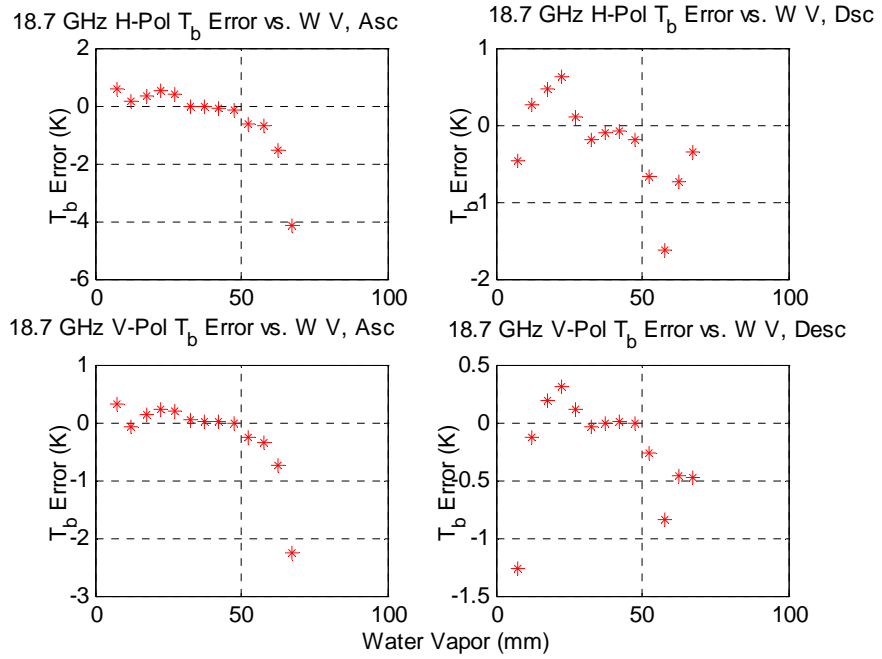


(a) before ws and sst correction

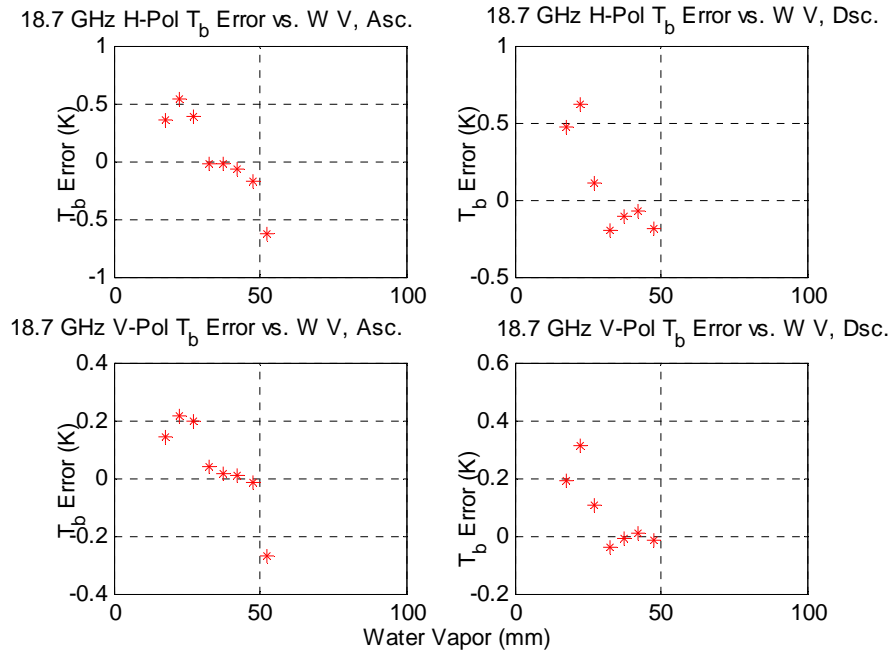


(b) after ws and sst correction

Figure C.5 Brightness Temperature Error Vs Water Vapor, 10.7 GHz



(a) before ws and sst correction



(b) after ws and sst correction

Figure C.6 Brightness Temperature Error Vs Water Vapor, 18.7 GHz

C.2 ADEOS AMSR Comparison with AMSR-E

At the time that this thesis research was being conducted, there were brightness temperature calibration issues with the preliminary AMSR data available; therefore, AMSR brightness temperatures for the 10.65 and 18.7 GHz channels were tuned using the RadTb radiative transfer model. RadTb environmental input parameters were obtained from SSMI F-15 and NOAA NCEP numerical weather analyses; and 3-day global Tb comparisons were performed for the beginning, middle and end of the ADEOS-II mission. Results indicated that small Tb biases were present, which were a function of orbit latitude; however, there were no systematic correlations with longitude nor season of the year. Thus, a single additive sinusoidal correction for AMSR was made using biases. The correction provides the additive Tb bias (in Kelvin) of 720 steps (0.5° latitude) for each orbit and for both frequencies (10.65 GHz and 18.7GHz) and both polarization.

Further, these same AMSR radiometric channels Tb's were compared with AMSR-E, which is the same instrument design that flies on a different NASA Earth Observing System satellite named AQUA and is well calibrated. For this comparison, the 3-day average (AMSR-AMSRE) delta-Tb's were calculated for September (1-3), 2003, and the data outliers (beyond the mean ± 2 * Std) were removed. Table C.1 presents the mean and standard deviation for this comparison, before and after applying the empirical RadTb correction. Given that the two AMSR's are only collocated in space but not time, there are transient geophysical events (e.g., winds and precip) that can cause the

brightness temperatures to differ significantly. Never the less, there is significant improvement after the RadTb tuning, which confirms this approach.

Table C.1. Typical AMSR – AMSR-E Delta-Tb, 3-day avg Sept. (1-3), 2003

(a) before AMSR sinusoidal correction

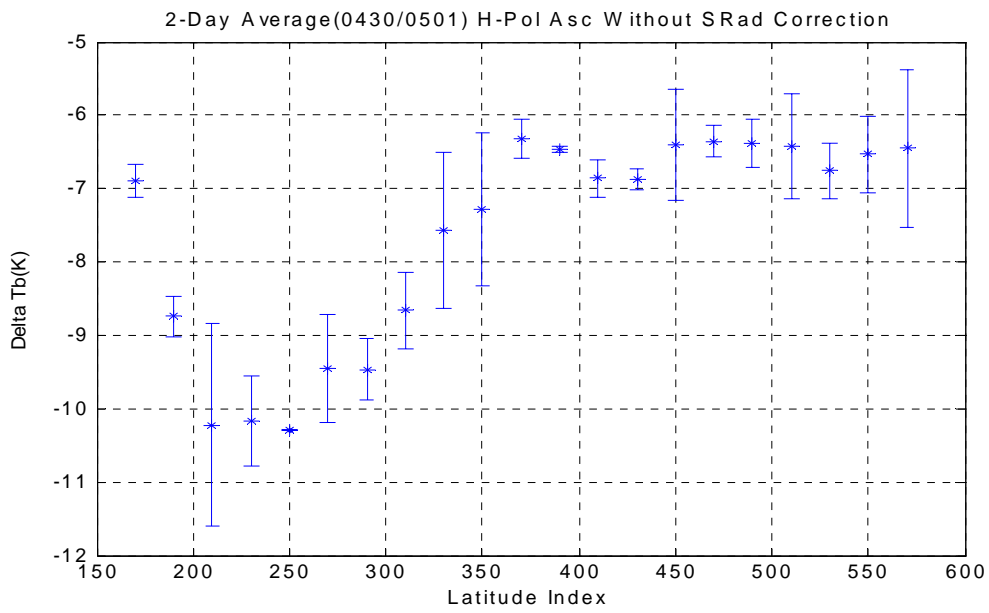
	Mean (K)	Std (K)
V-Pol Asc 18.7 GHz	5.19	3.27
V-Pol Dsc 18.7 GHz	2.87	3.23
V-Pol Asc 10.7 GHz	4.52	1.65
V-Pol Dsc 10.7 GHz	2.56	1.79
H-Pol Asc 18.7 GHz	3.34	6.54
H-Pol Dsc 18.7 GHz	1.19	6.50
H-Pol Asc 10.7 GHz	2.65	2.97
H-Pol Dsc 10.7 GHz	1.49	2.98

(b) after AMSR sinusoidal correction

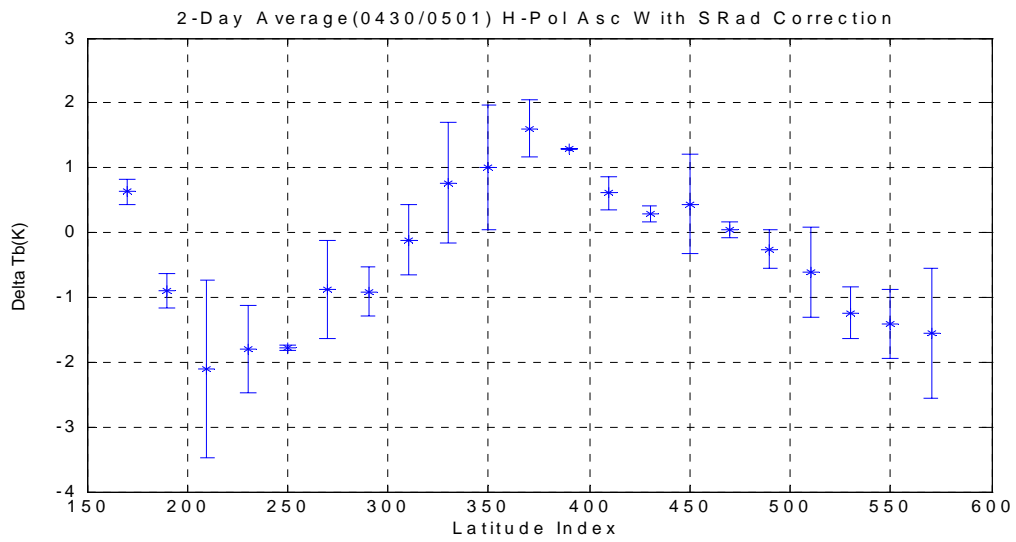
	Mean (K)	Std (K)
V-Pol Asc 18.7 GHz	2.08	3.23
V-Pol Dsc 18.7 GHz	0.75	3.31
V-Pol Asc 10.7 GHz	1.40	1.59
V-Pol Dsc 10.7 GHz	0.43	1.89
H-Pol Asc 18.7 GHz	2.17	6.52
H-Pol Dsc 18.7 GHz	1.66	6.51
H-Pol Asc 10.7 GHz	1.47	2.95
H-Pol Dsc 10.7 GHz	1.96	2.98

APPENDIX D

SRad VALIDATION RESULTS

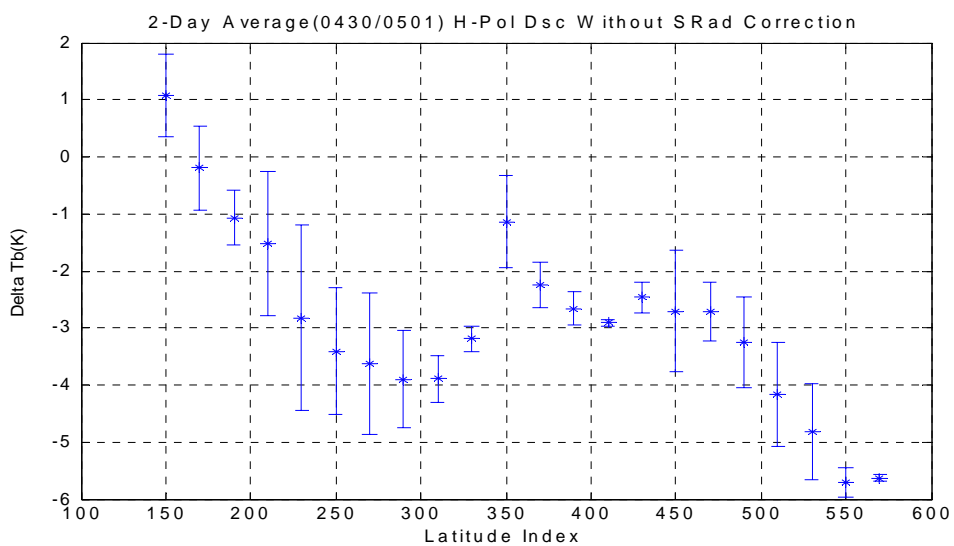


(a) Before applying the empirical correction

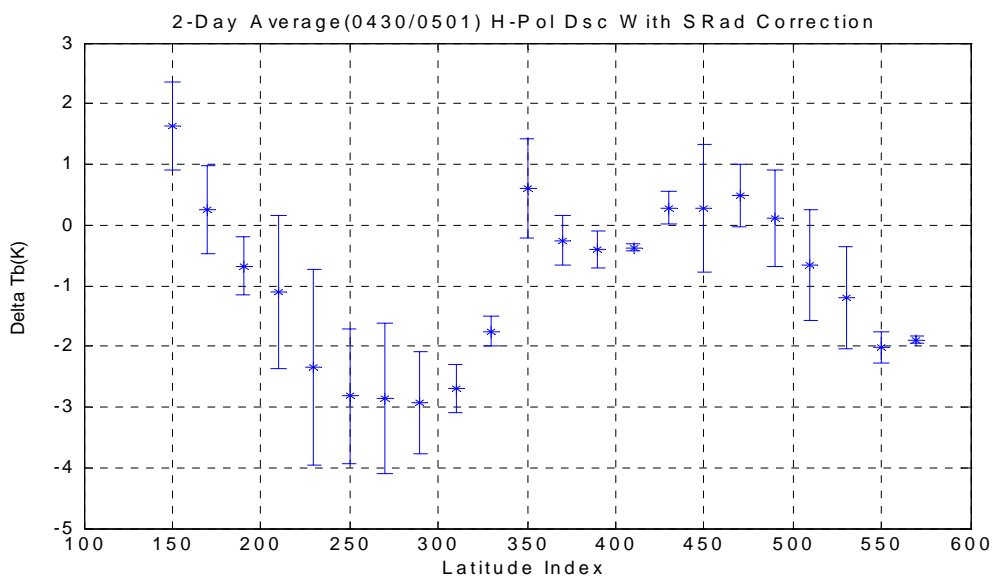


(b) After applying the empirical correction

Figure D.1 (SRad - AMSR) H-pol 2-day avg delta-Tb ascending orbit segments (April 30 - May 1,2003)

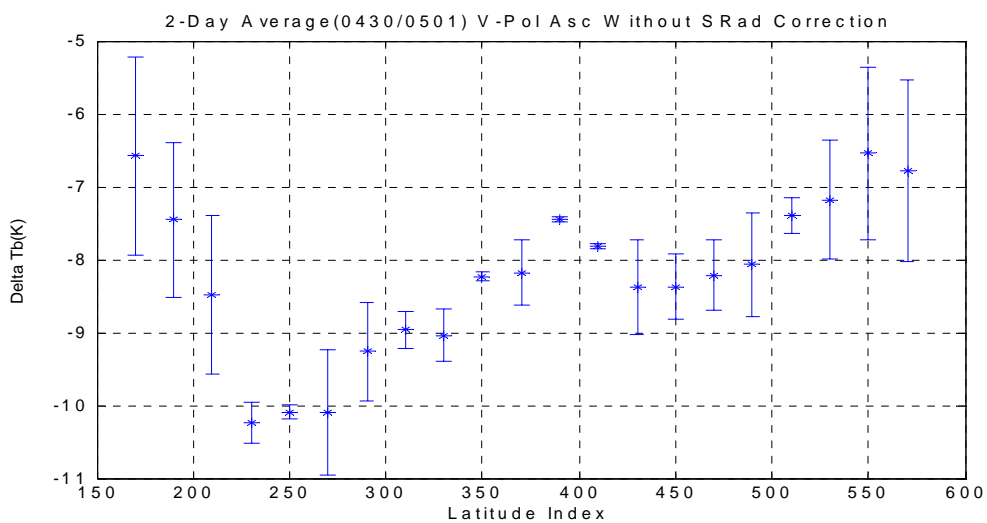


(a) Before applying the empirical correction

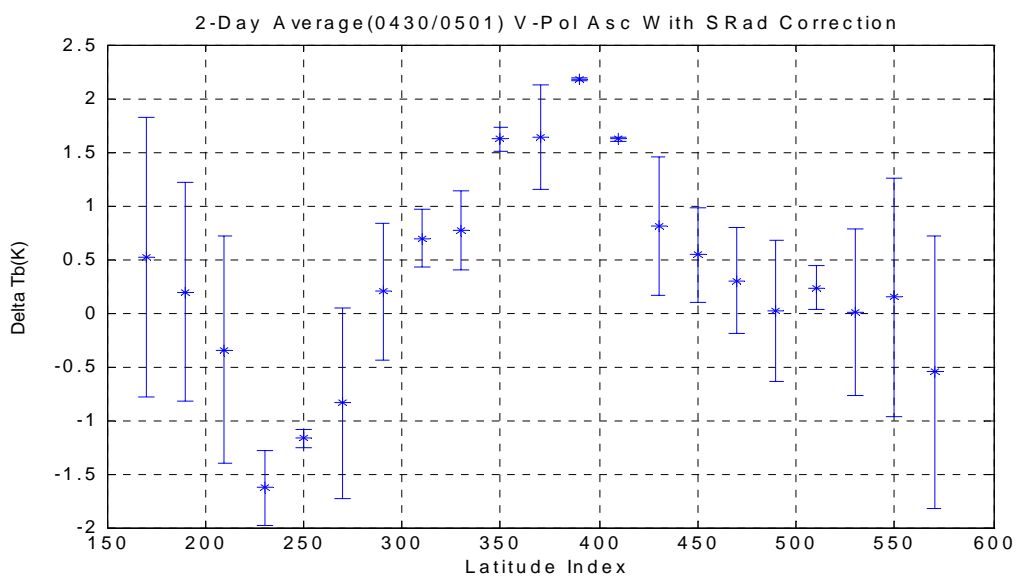


(b) After applying the empirical correction

Figure D.2 (SRad - AMSR) H-pol 2-day avg delta-Tb descending orbit segments (April 30 - May 1,2003)

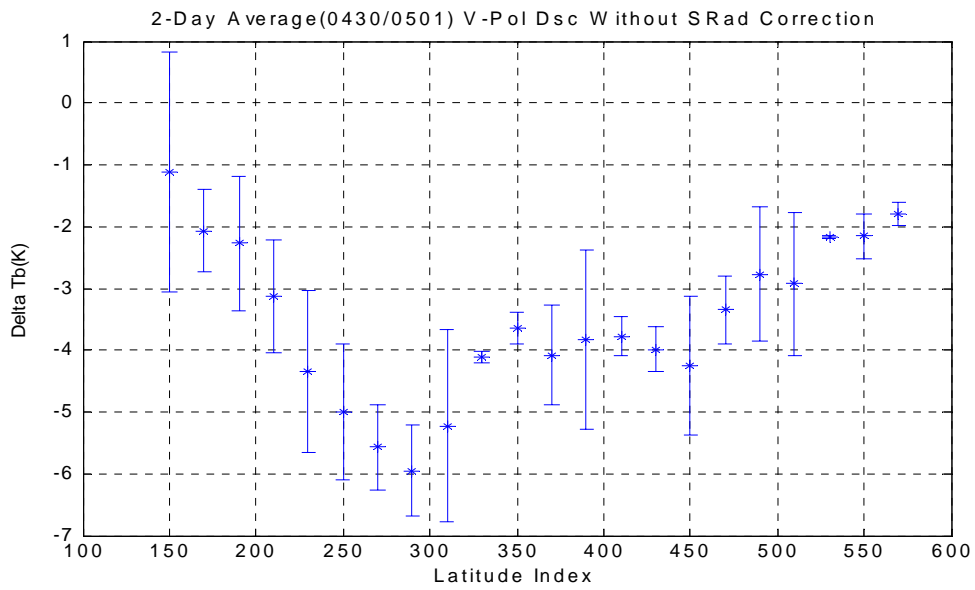


(a) Before applying the empirical correction

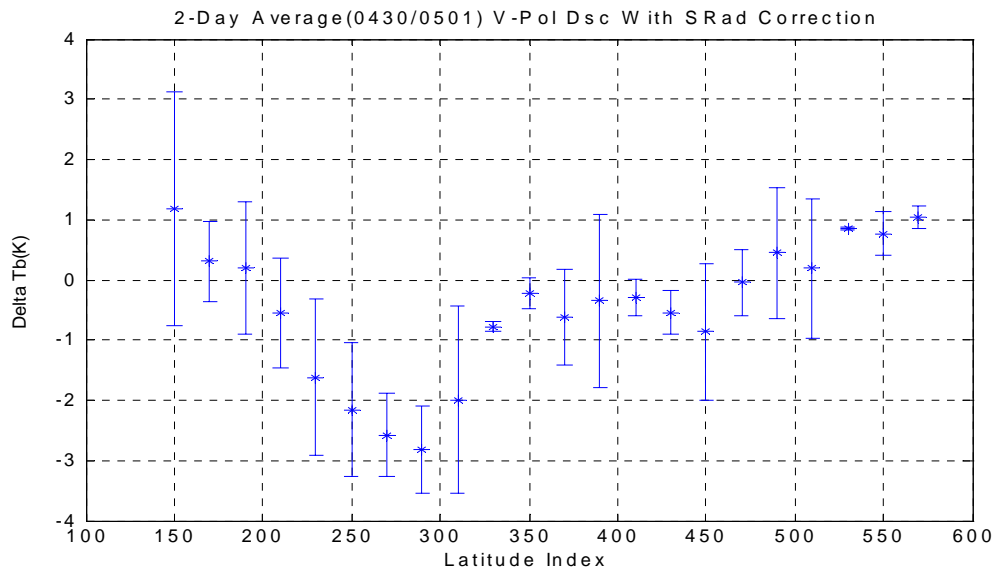


(b) After applying the empirical correction

Figure D.3 (SRad - AMSR) V-pol 2-day avg delta-Tb ascending orbit segments (April 30 - May 1, 2003)

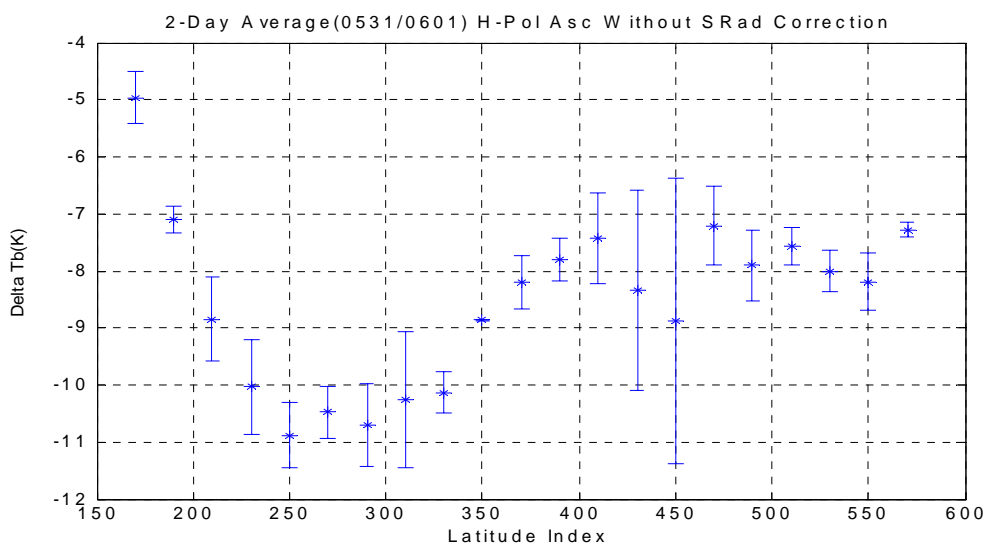


(a) Before applying the empirical correction

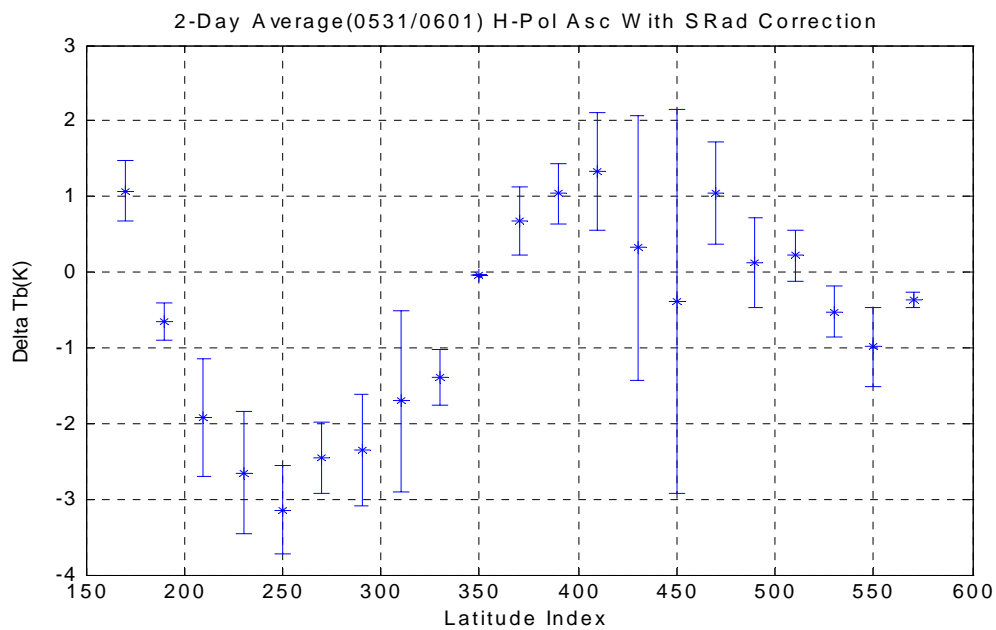


(b) After applying the empirical correction

Figure D.4 (SRad - AMSR) V-pol 2-day avg delta-Tb descending orbit segments (April 30 - May 1, 2003)

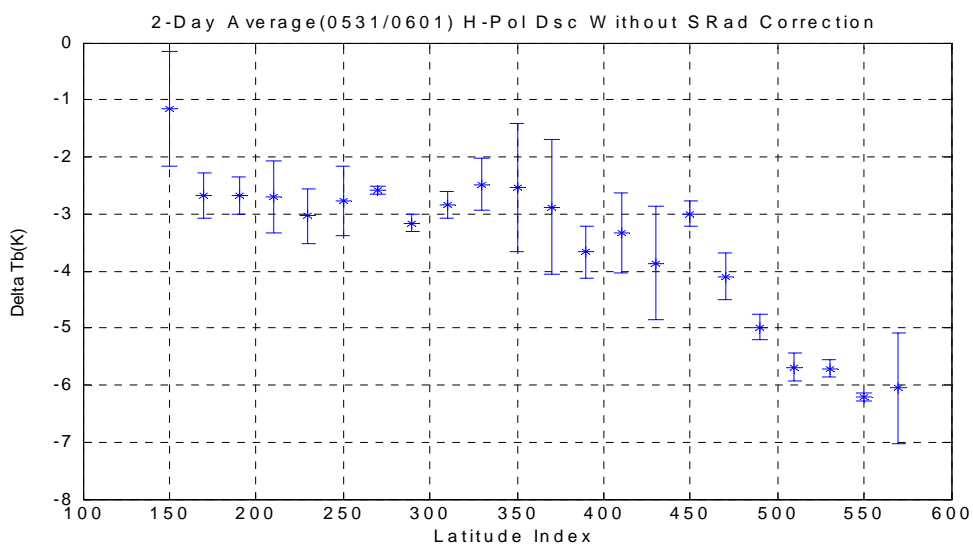


(a) Before applying the empirical correction

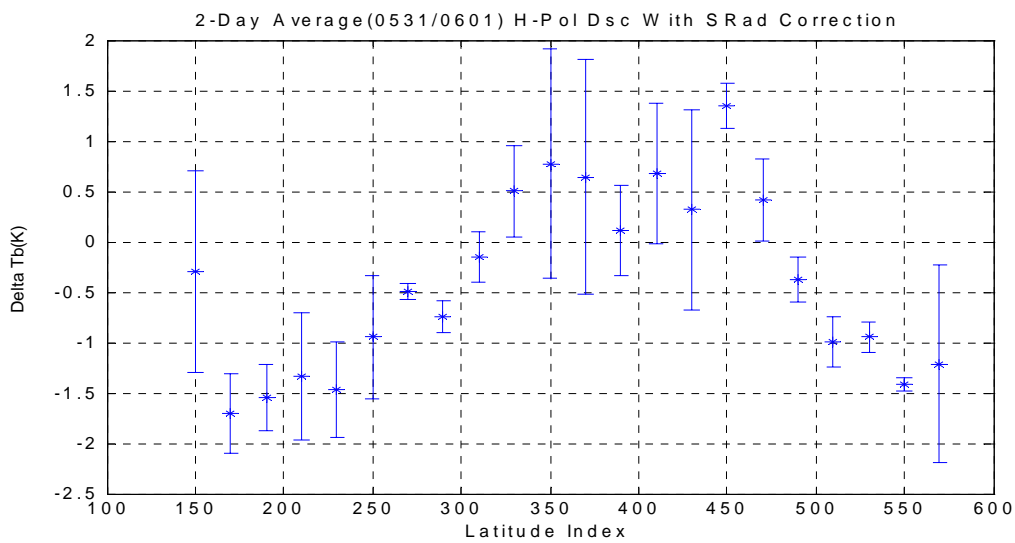


(b) After applying the empirical correction

Figure D.5 (SRad - AMSR) H-pol 2-day avg delta-Tb ascending orbit segments (May 31 - June 1,2003)

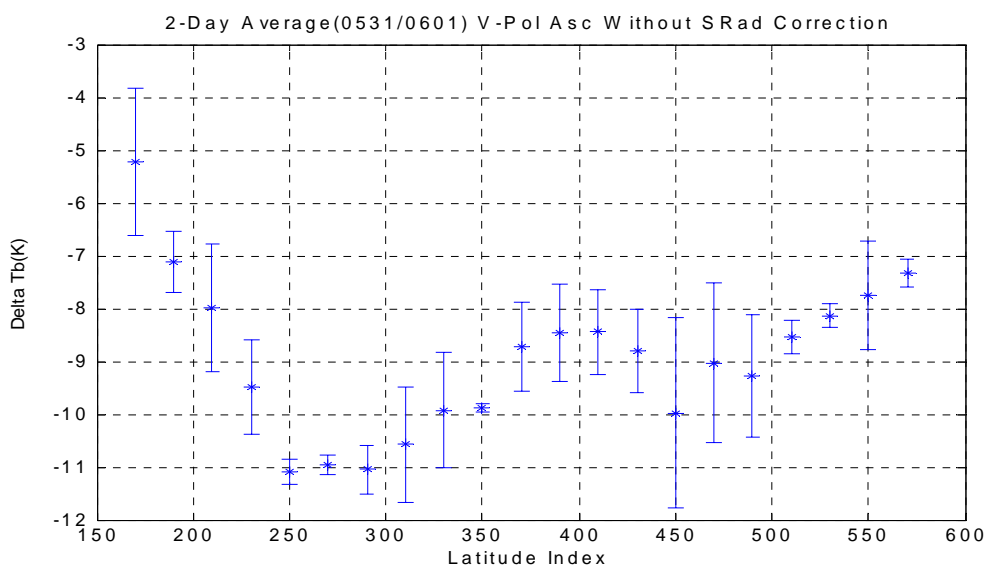


(a) Before applying the empirical correction

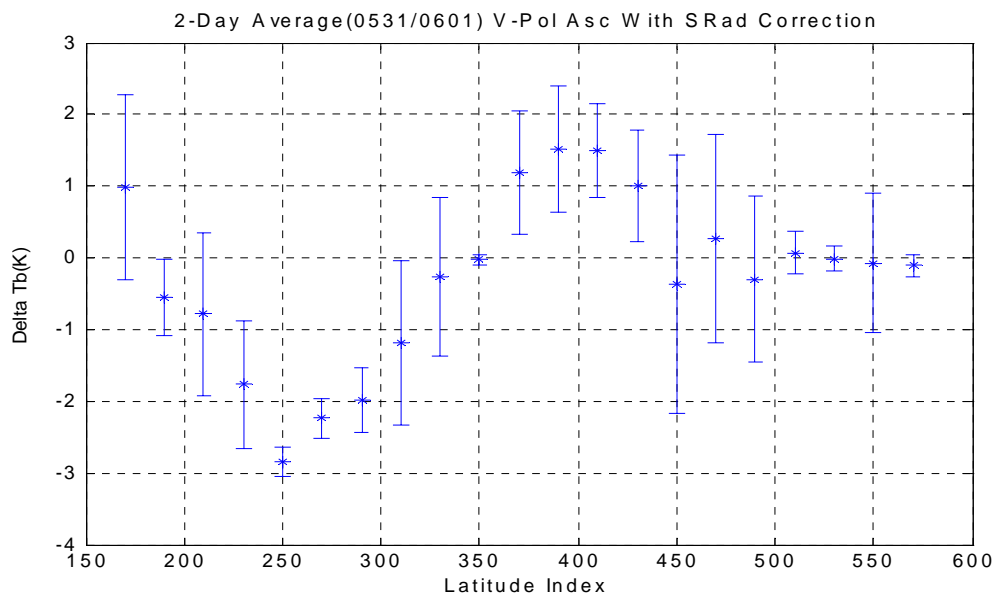


(b) After applying the empirical correction

Figure D.6 (SRad - AMSR) H-pol 2-day avg delta-Tb descending orbit segments (May 31 - June 1,2003)

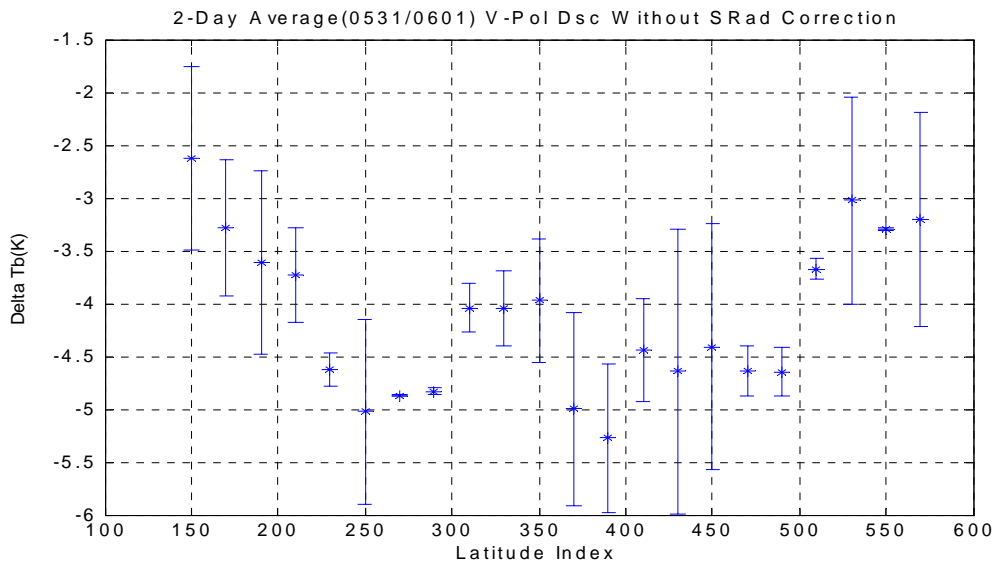


(a) Before applying the empirical correction

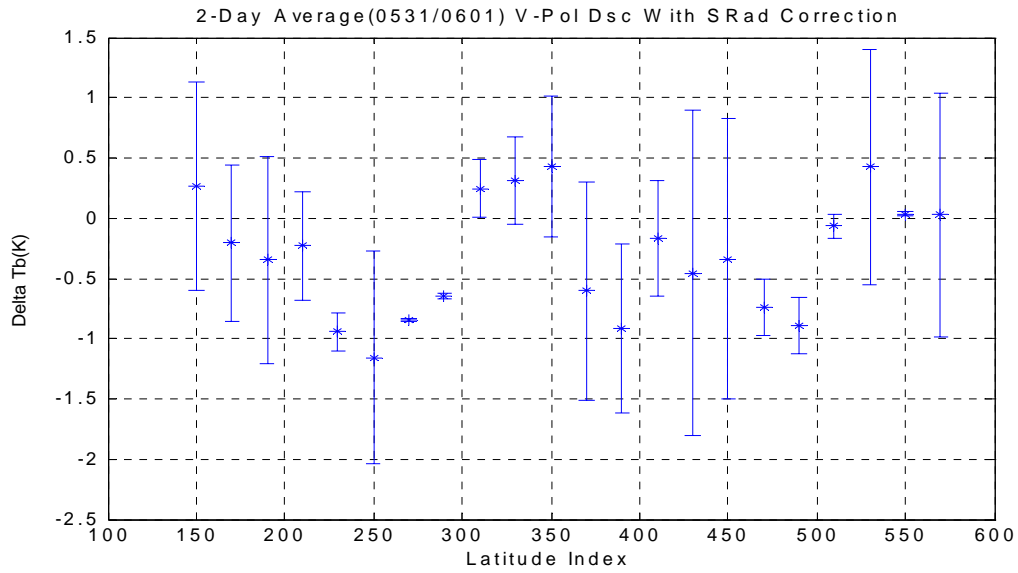


(b) After applying the empirical correction

Figure D.7 (SRad - AMSR) V-pol 2-day avg delta-Tb ascending orbit segments (May 31 - June 1,2003)

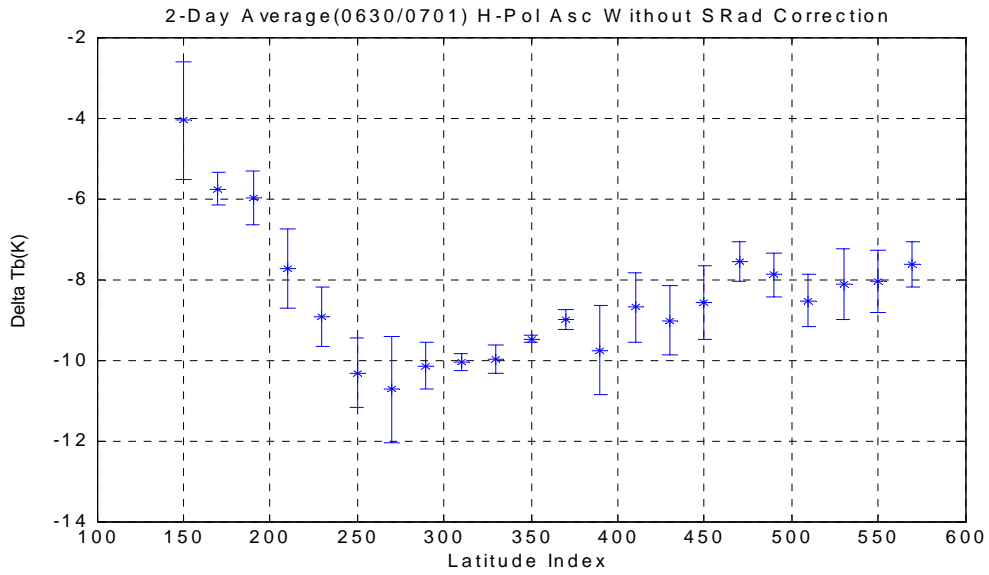


(a) Before applying the empirical correction

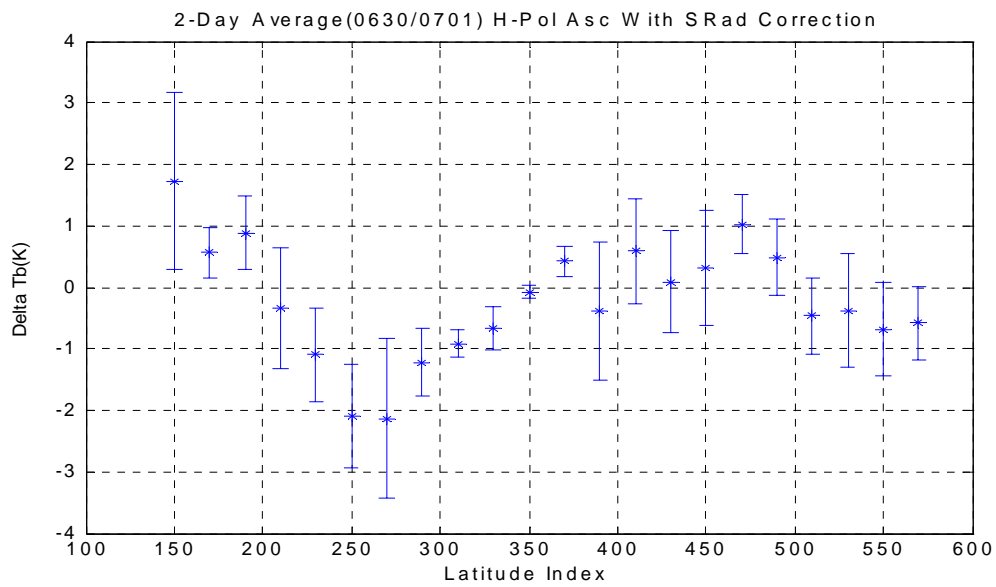


(b) After applying the empirical correction

Figure D.8 (SRad - AMSR) V-pol 2-day avg delta-Tb descending orbit segments (May 31 - June 1,2003)

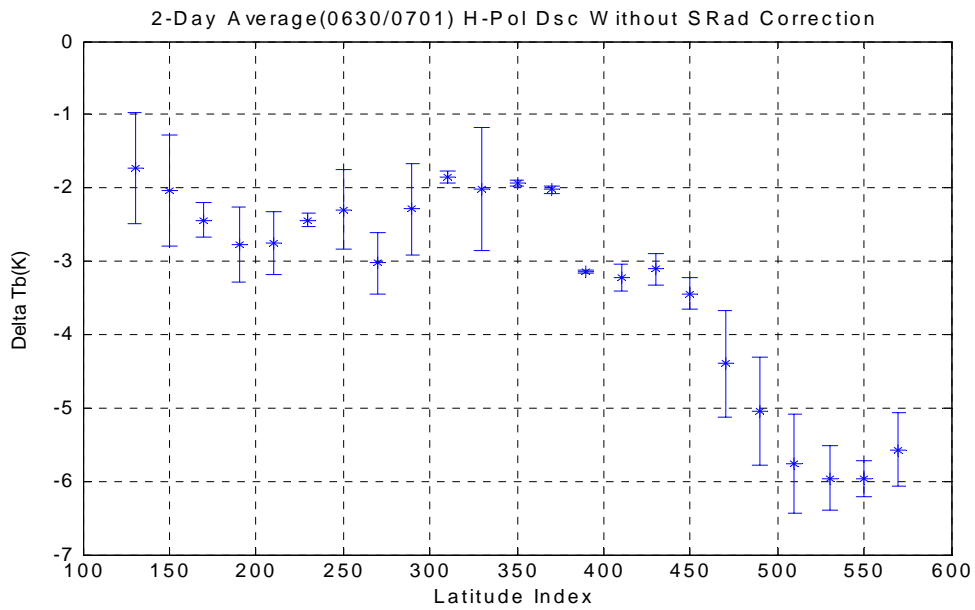


(a) Before applying the empirical correction

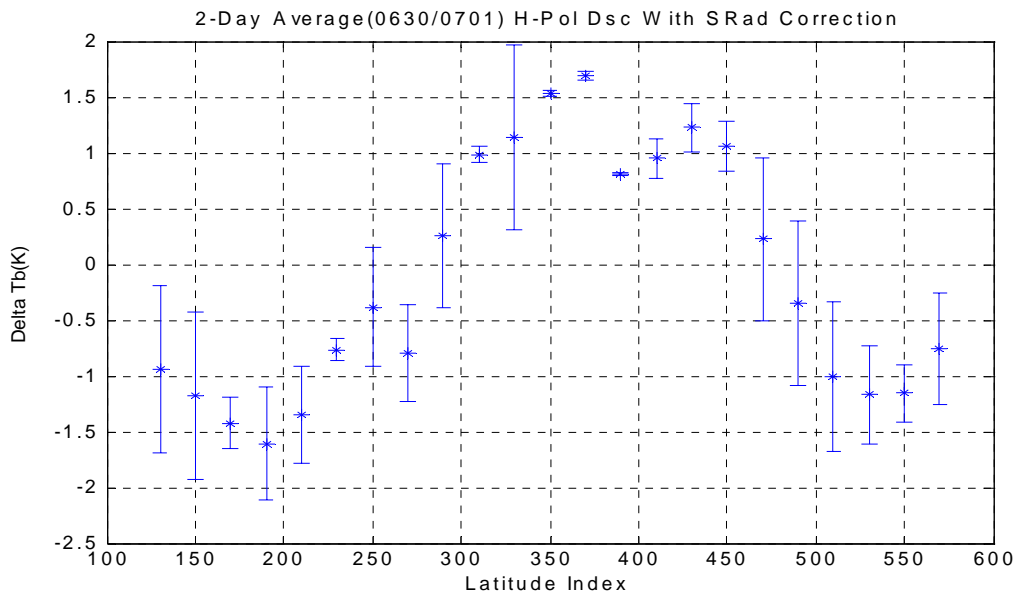


(b) After applying the empirical correction

Figure D.9 (SRad - AMSR) H-pol 2-day avg delta-Tb ascending orbit segments (June 30 - July 1,2003)

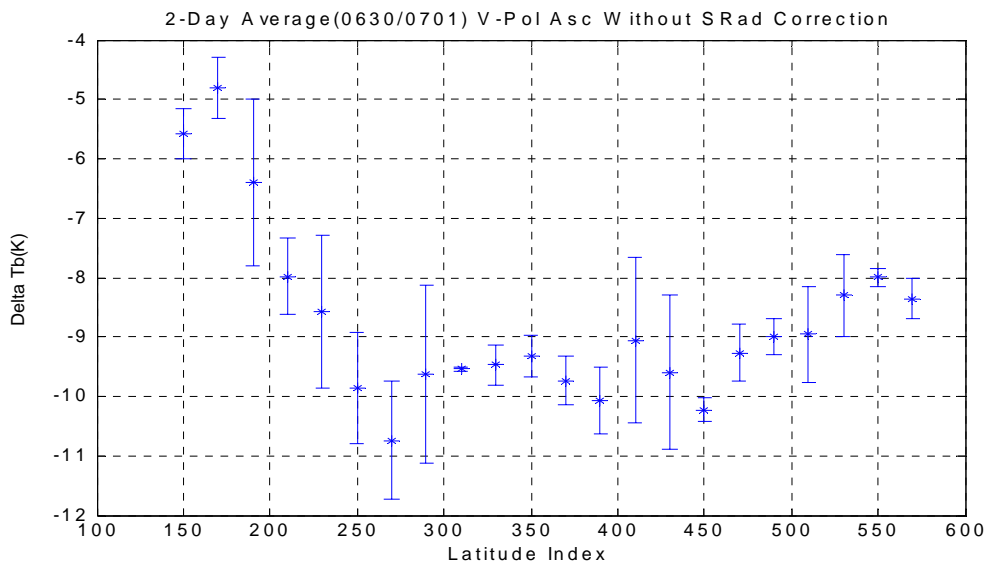


(a) Before applying the empirical correction

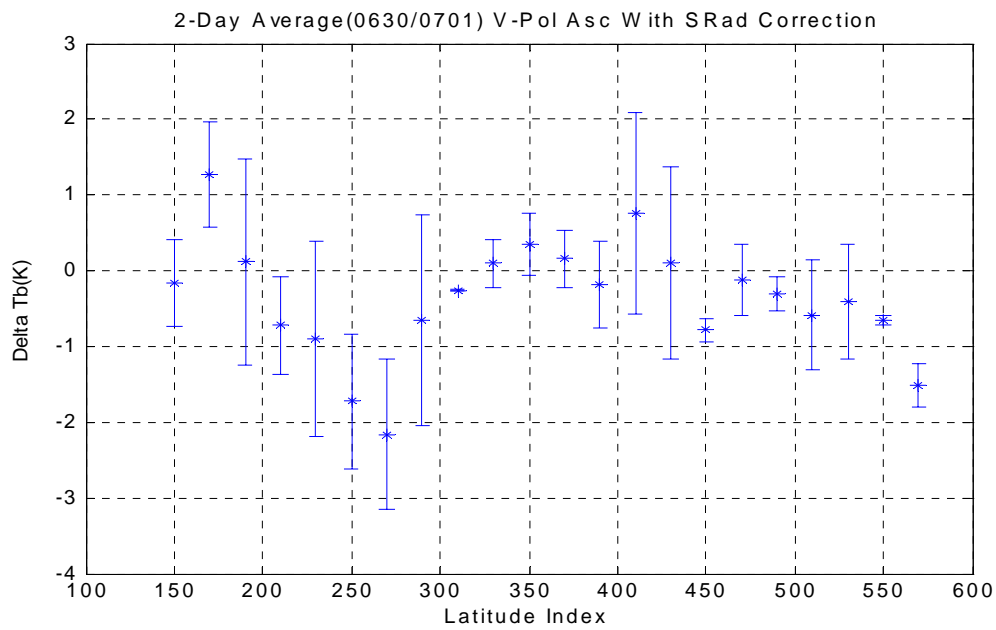


(b) After applying the empirical correction

Figure D.10 (SRad - AMSR) H-pol 2-day avg delta-Tb descending orbit segments (June 30 - July 1,2003)

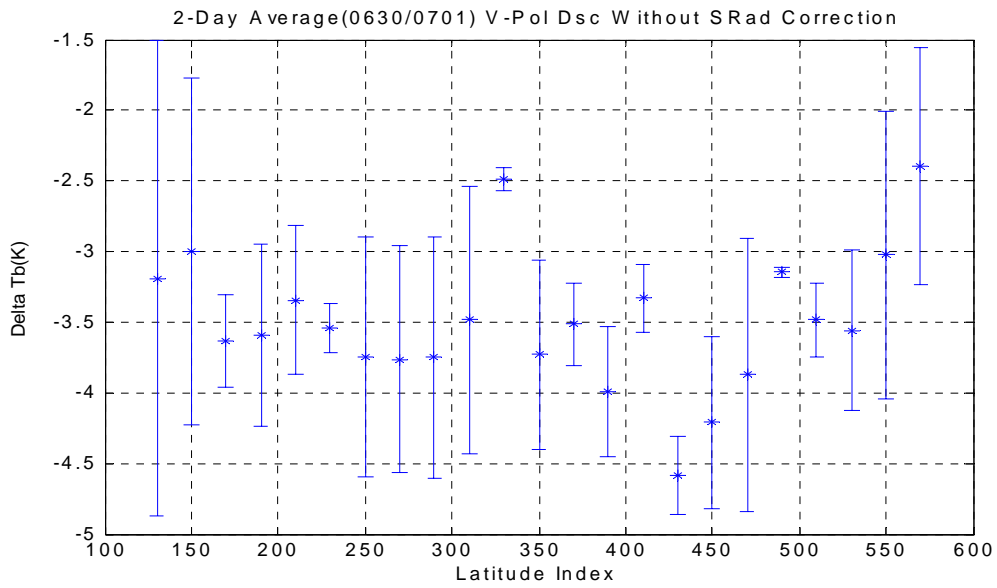


(a) Before applying the empirical correction

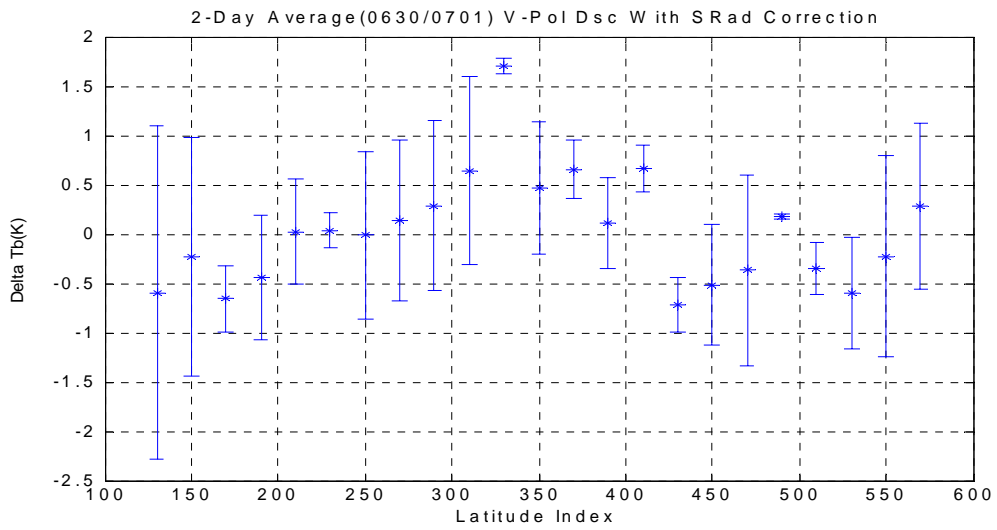


(b) After applying the empirical correction

Figure D.11 (SRad - AMSR) V-pol 2-day avg delta-Tb ascending orbit segments (June 30 - July 1,2003)

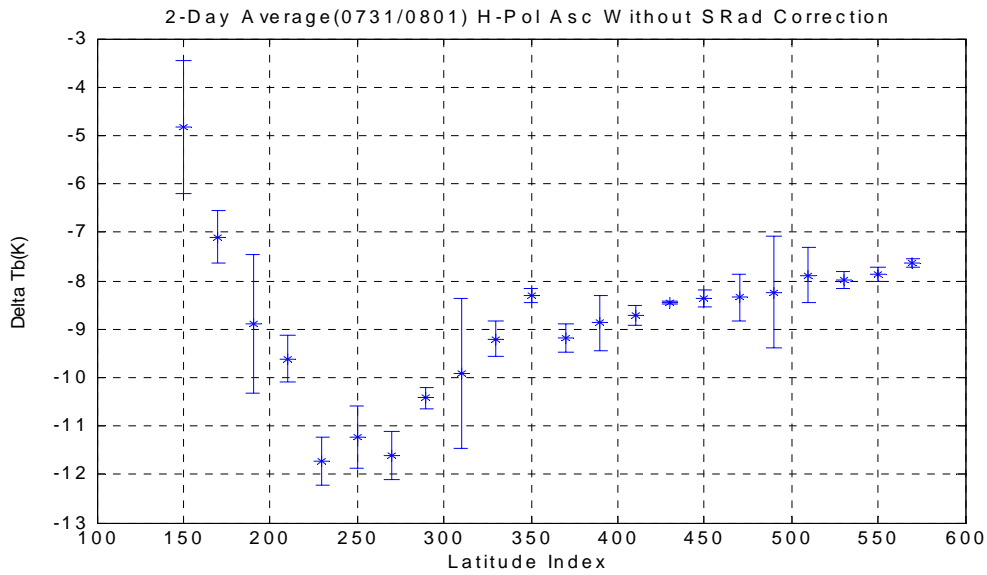


(a) Before applying the empirical correction

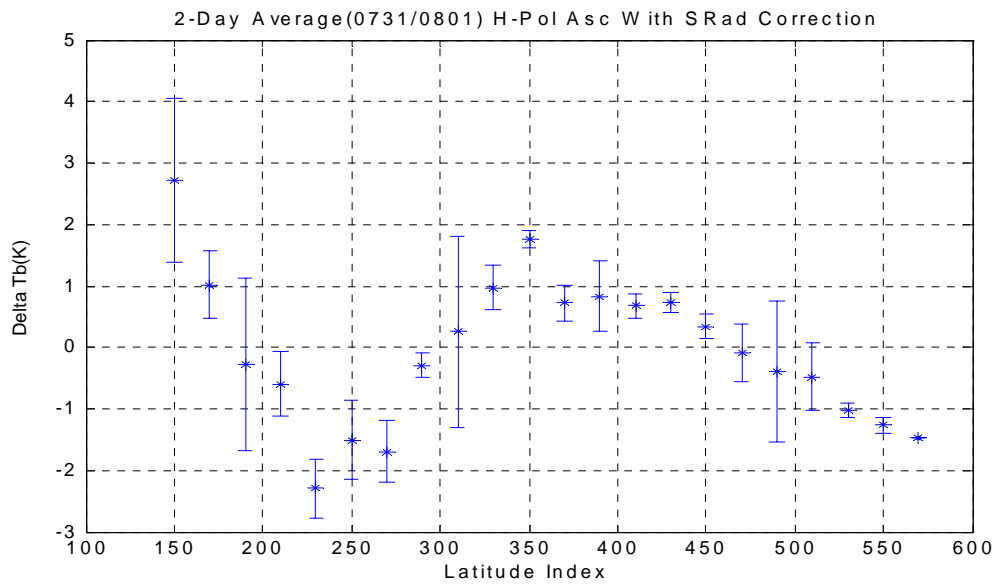


(b) After applying the empirical correction

Figure D.12 (SRad - AMSR) V-pol 2-day avg delta-Tb descending orbit segments (June 30 - July 1,2003)

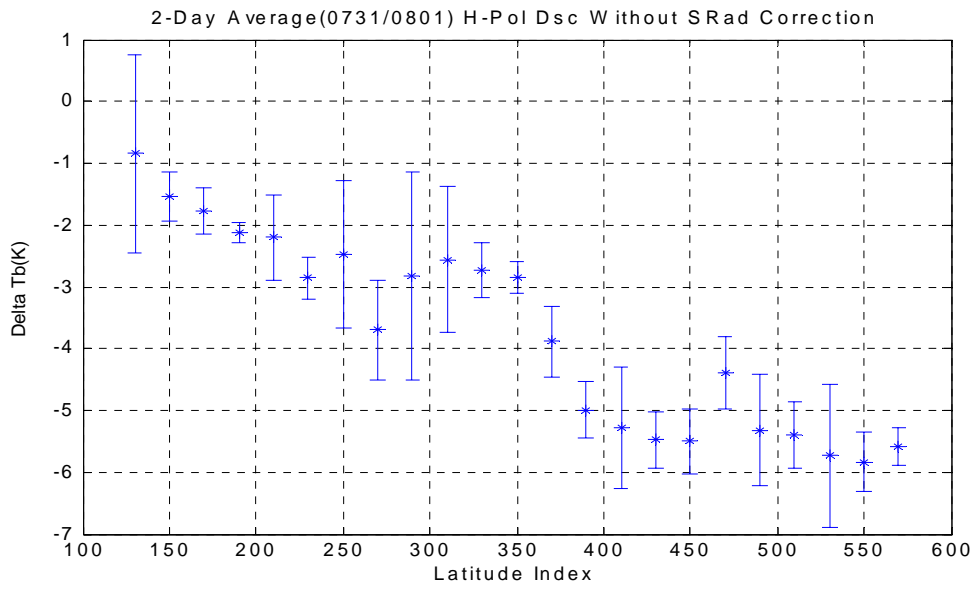


(a) Before applying the empirical correction

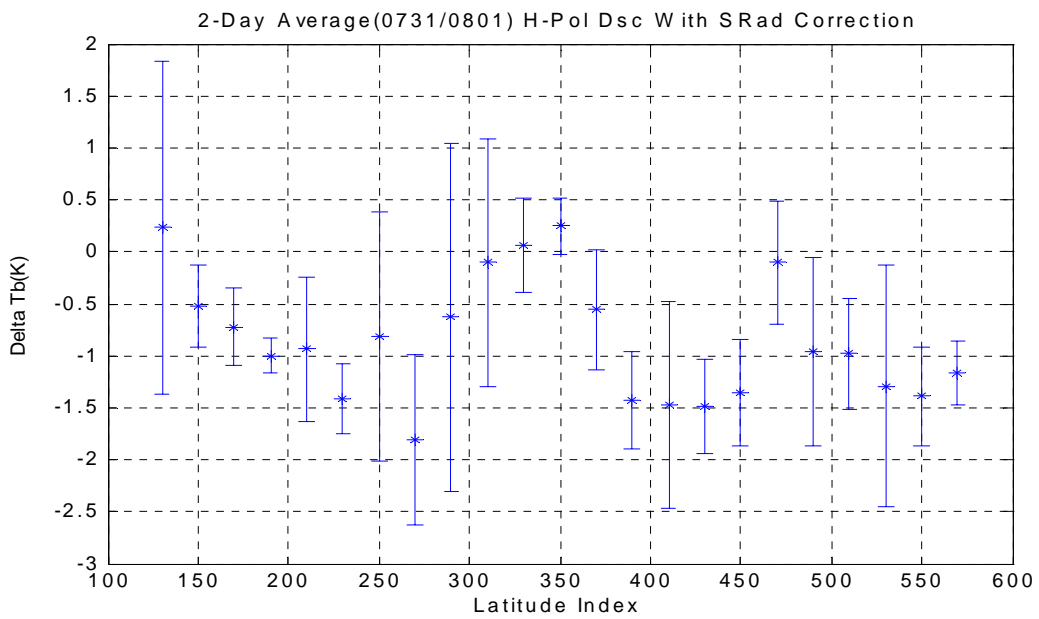


(b) After applying the empirical correction

Figure D.13 (SRad - AMSR) H-pol 2-day avg delta-Tb ascending orbit segments (July 31 - August 1, 2003)

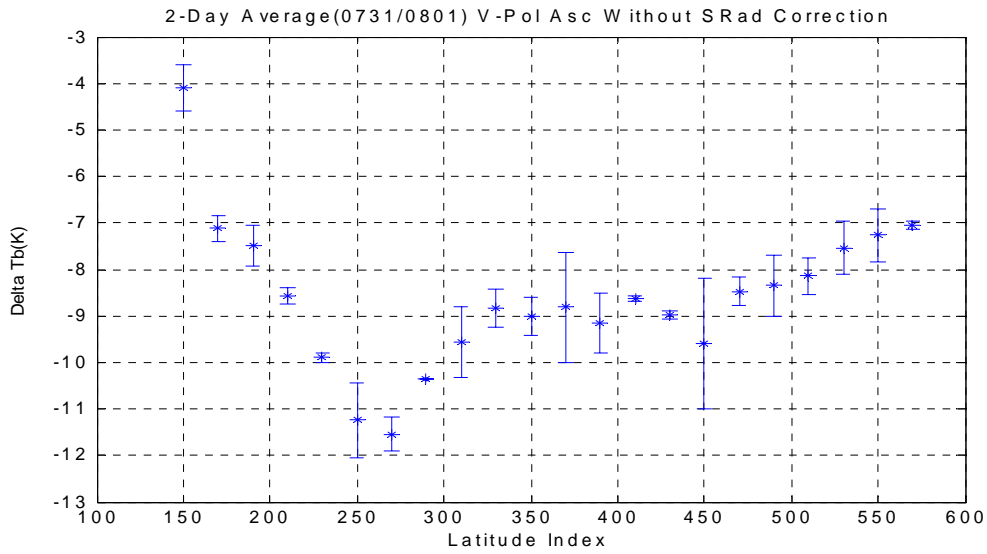


(a) Before applying the empirical correction

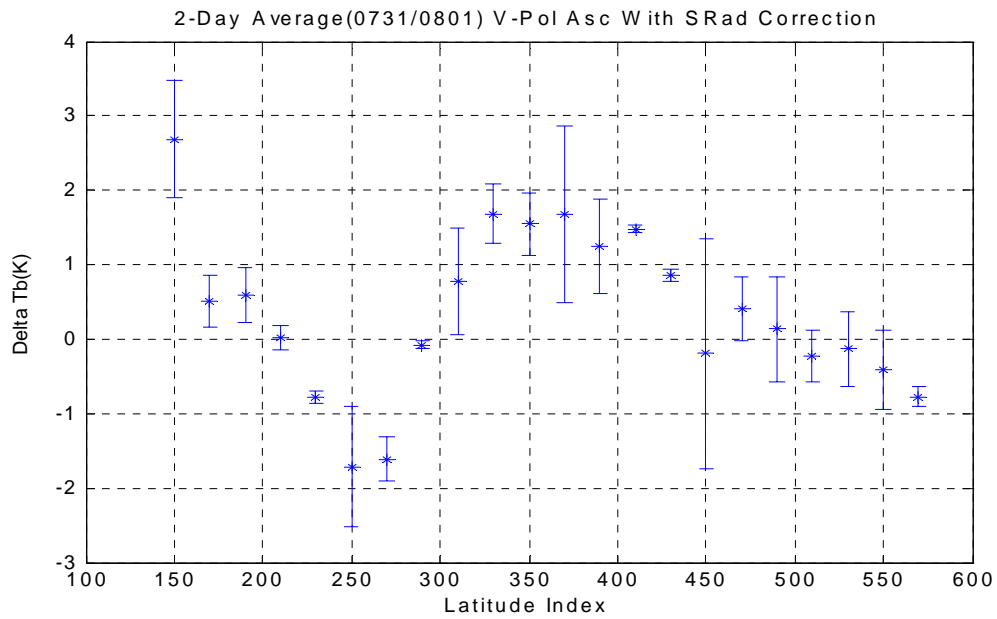


(b) After applying the empirical correction

Figure D.14 (SRad - AMSR) H-pol 2-day avg delta-Tb descending orbit segments (July 31 - August 1,2003)

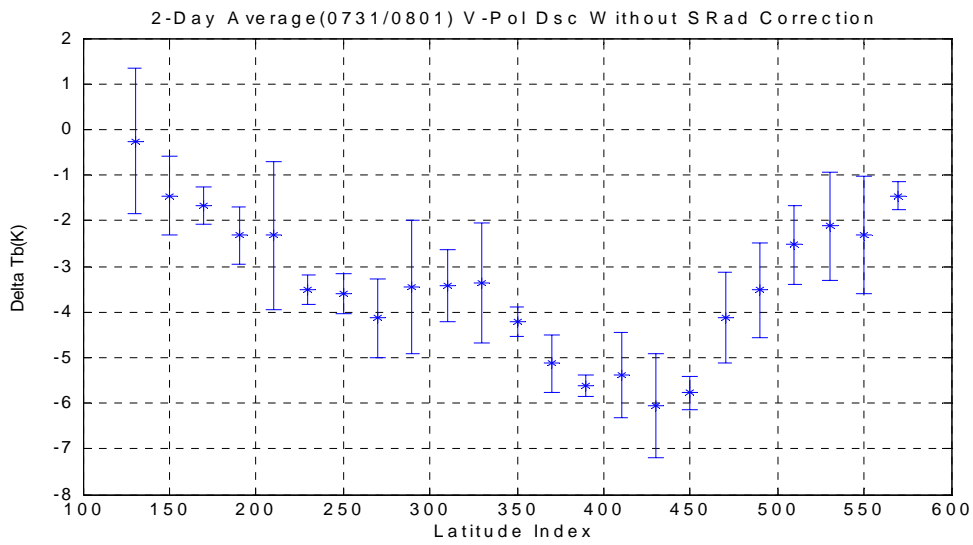


(a) Before applying the empirical correction

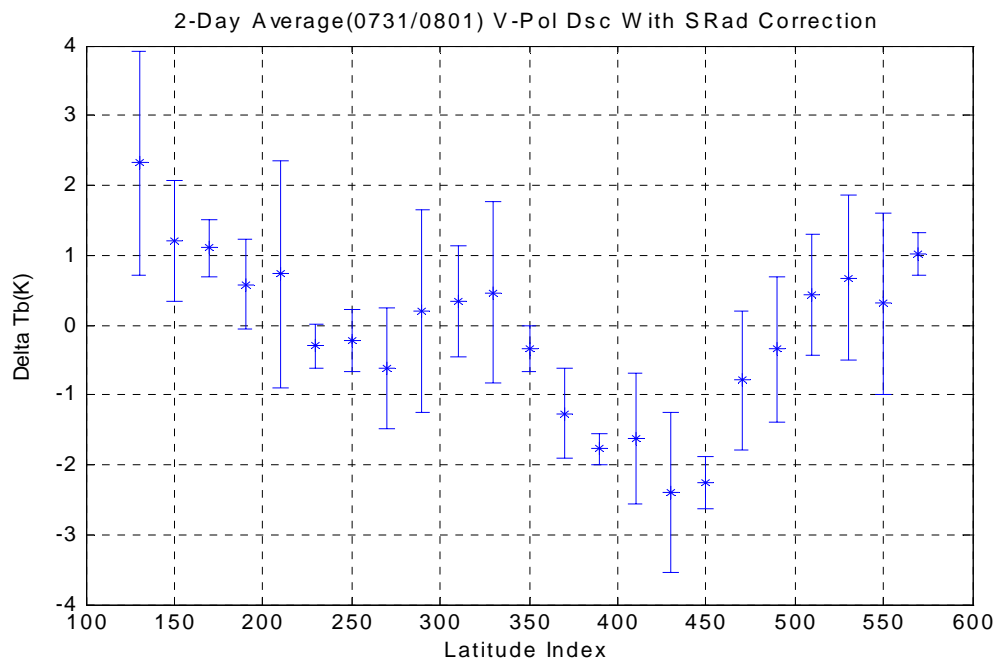


(b) After applying the empirical correction

Figure D.15 (SRad - AMSR) V-pol 2-day avg delta-Tb ascending orbit segments (July 31 - August 1,2003)

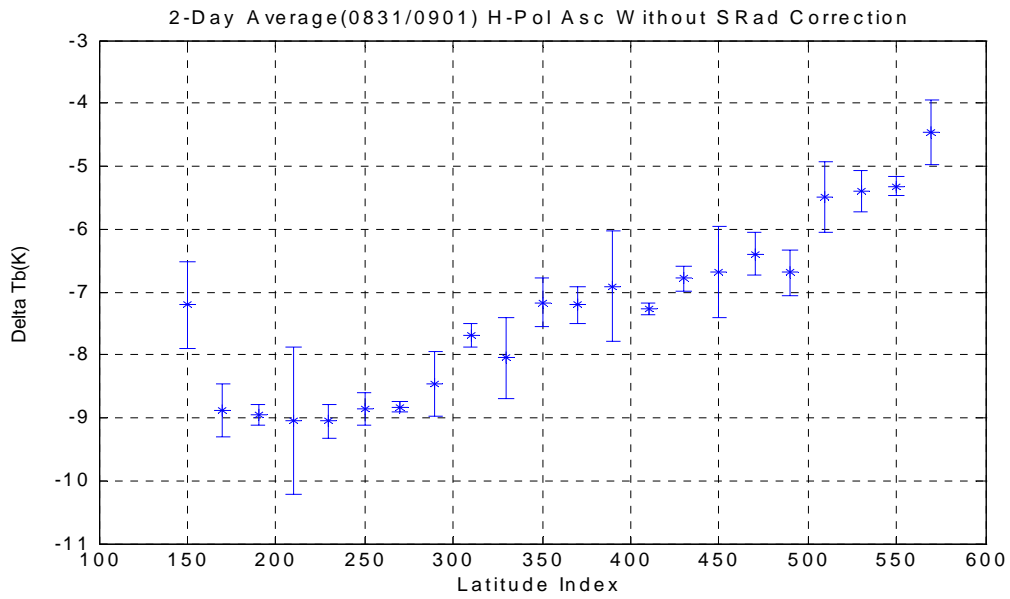


(a) Before applying the empirical correction

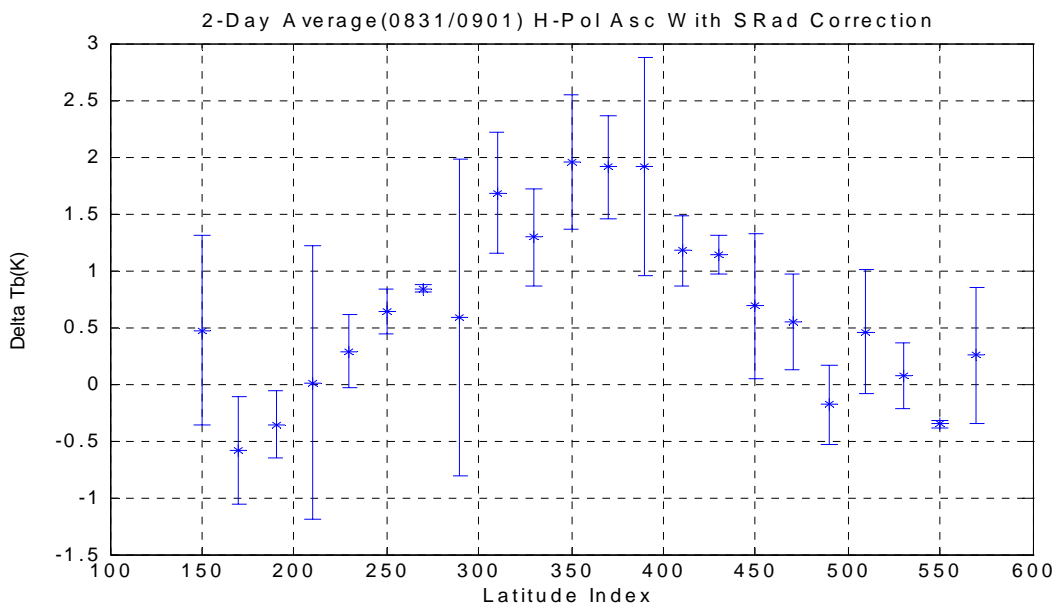


(b) After applying the empirical correction

Figure D.16 (SRad - AMSR) V-pol 2-day avg delta-Tb descending orbit segments (July 31 - August 1,2003)

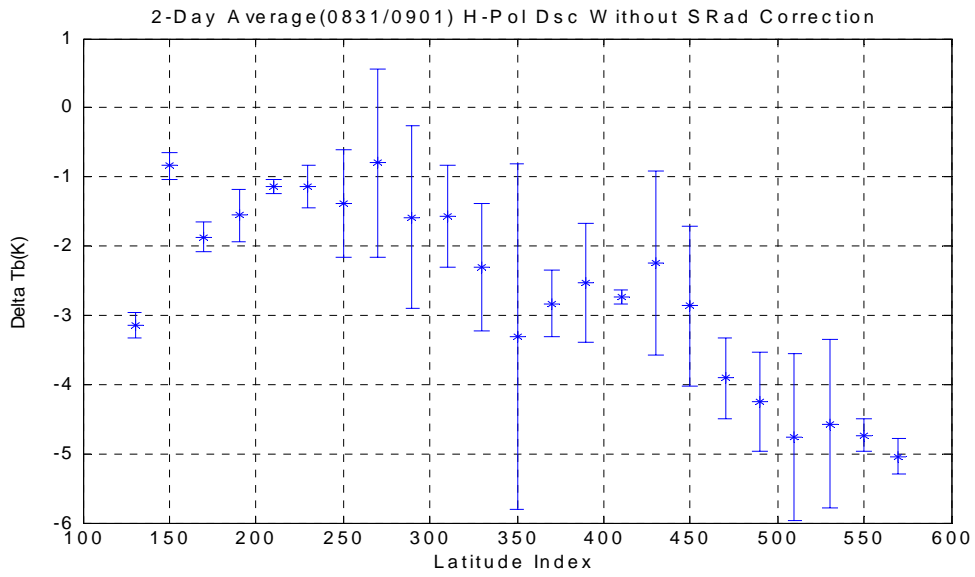


(a) Before applying the empirical correction

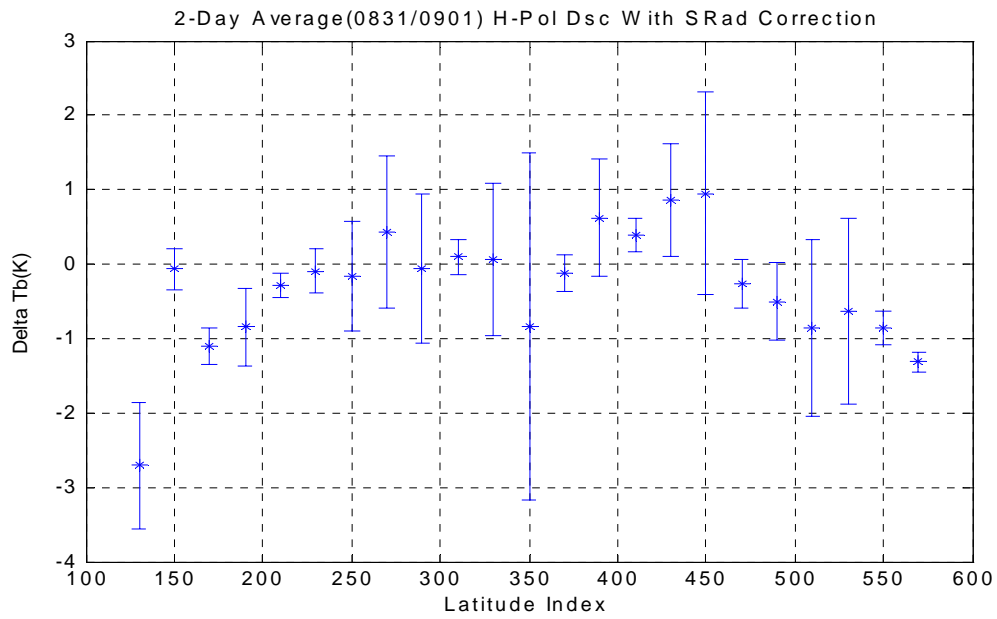


(b) After applying the empirical correction

Figure D.17 (SRad - AMSR) H-pol 2-day avg delta-Tb ascending orbit segments (August 31 - September 1,2003)

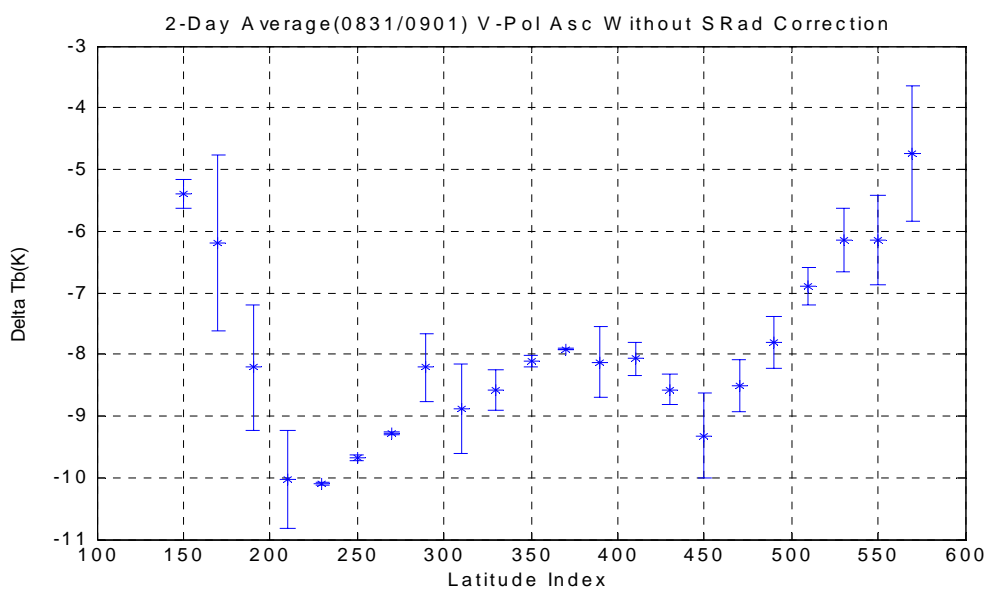


(a) Before applying the empirical correction

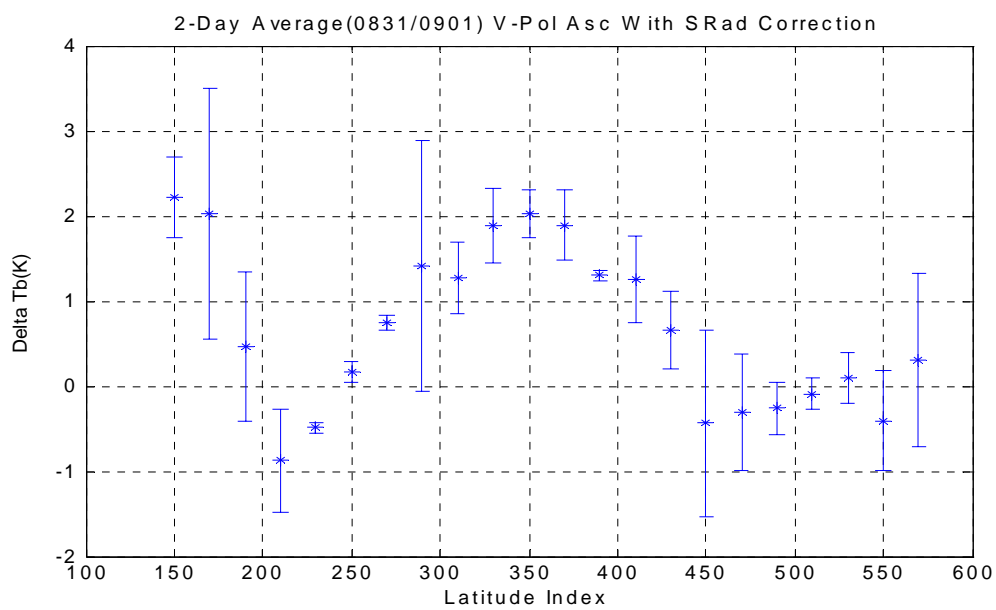


(b) After applying the empirical correction

Figure D.18 (SRad - AMSR) H-pol 2-day avg delta-Tb descending orbit segments (August 31 - September 1,2003)

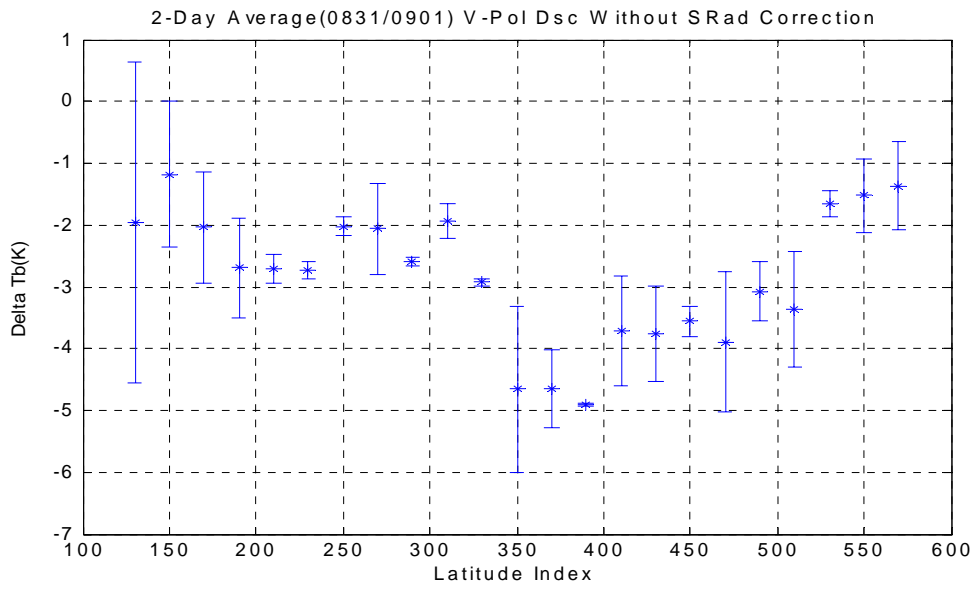


(a) Before applying the empirical correction

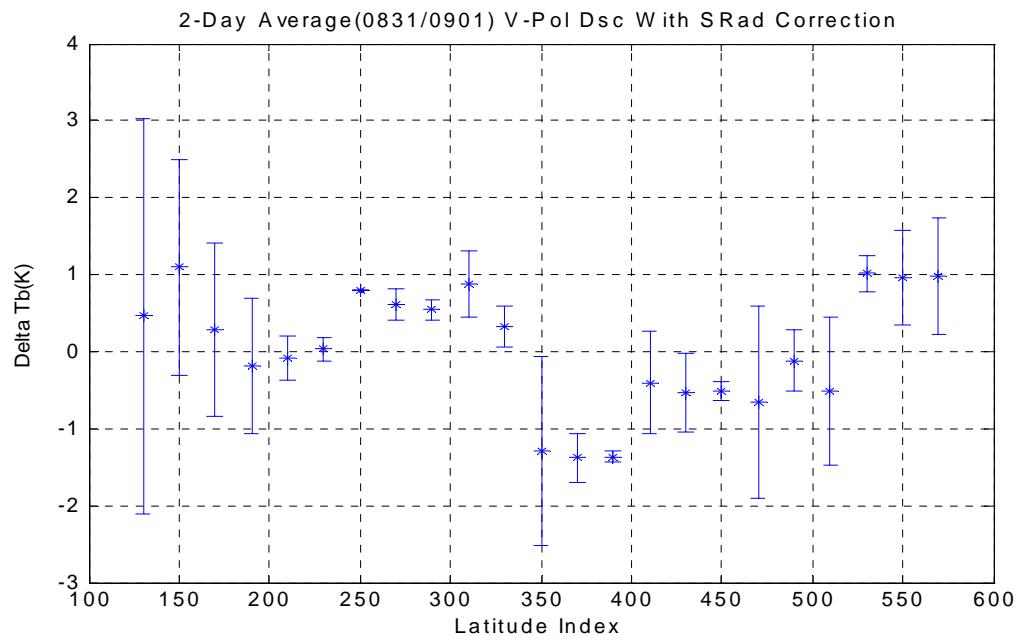


(b) After applying the empirical correction

Figure D.19 (SRad - AMSR) V-pol 2-day avg delta-Tb ascending orbit segments (August 31 - September 1,2003)

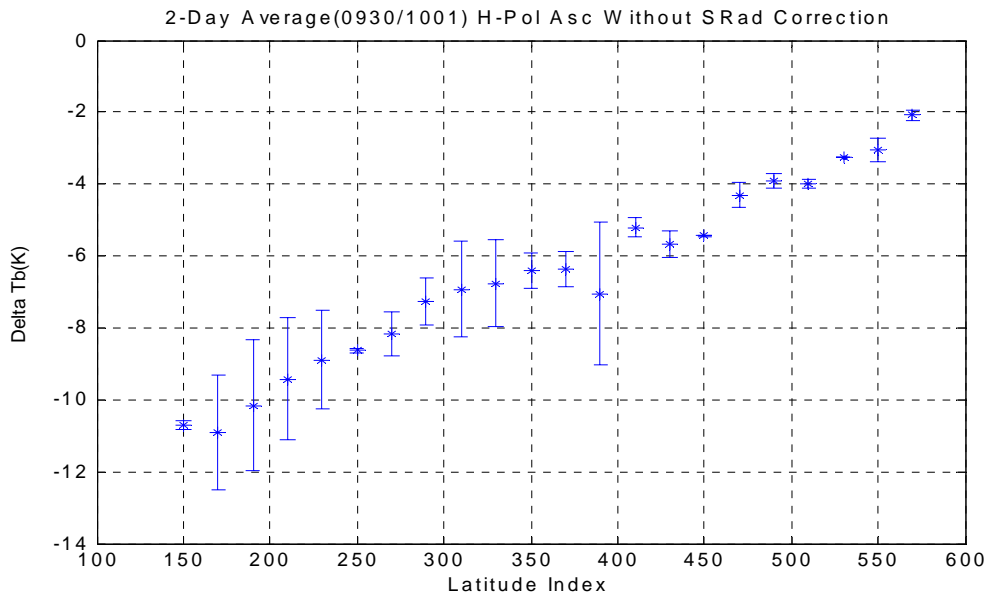


(a) Before applying the empirical correction

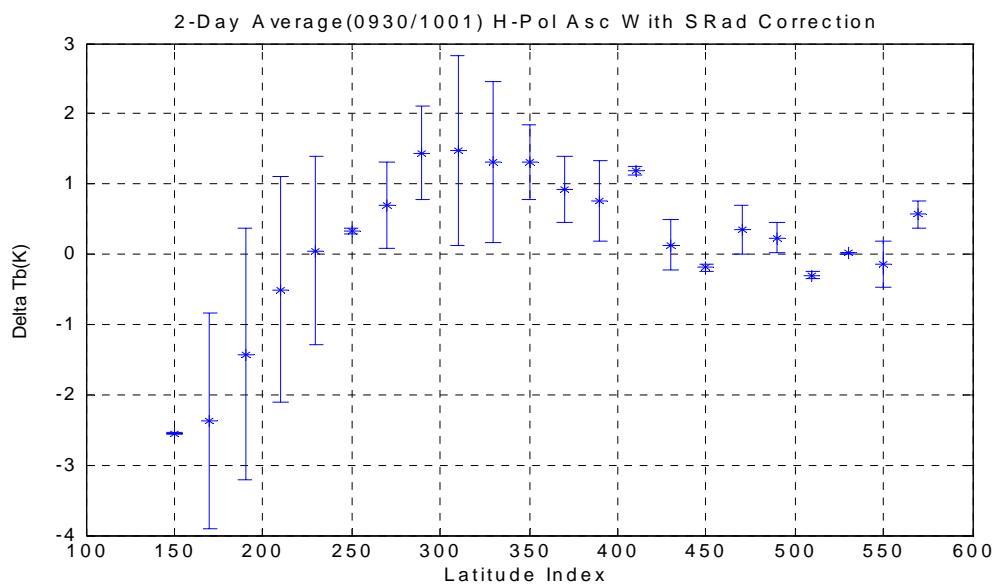


(b) After applying the empirical correction

Figure D.20 (SRad - AMSR) V-pol 2-day avg delta-Tb descending orbit segments (August 31 - September 1,2003)

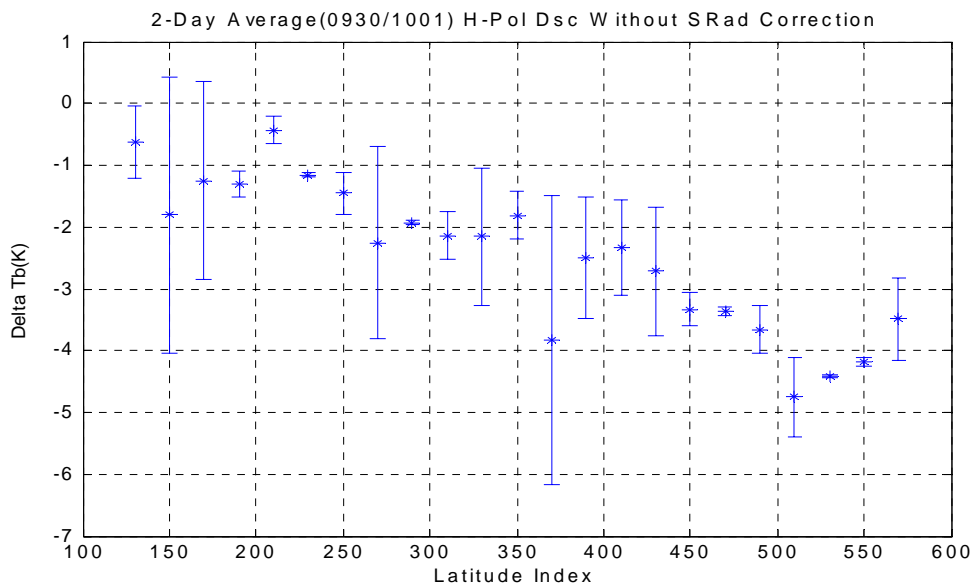


(a) Before applying the empirical correction

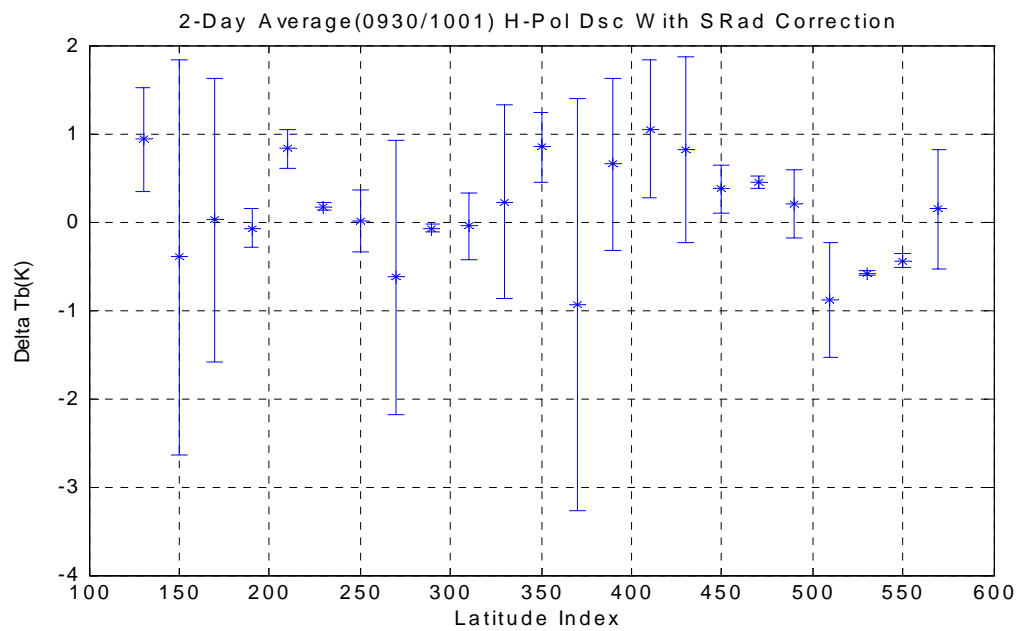


(b) After applying the empirical correction

Figure D.21 (SRad - AMSR) H-pol 2-day avg delta-Tb ascending orbit segments (September 30 - October 1,2003)

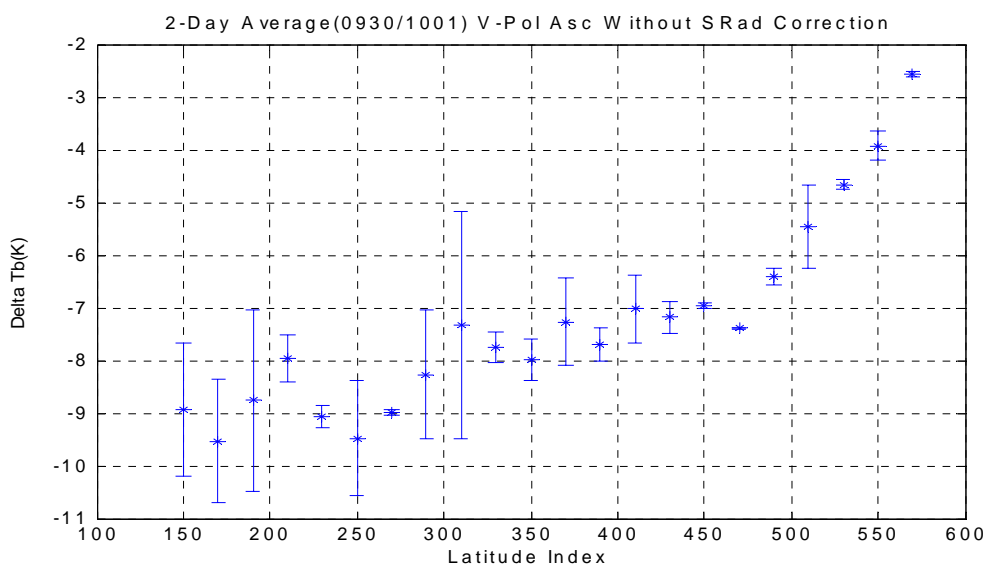


(a) Before applying the empirical correction

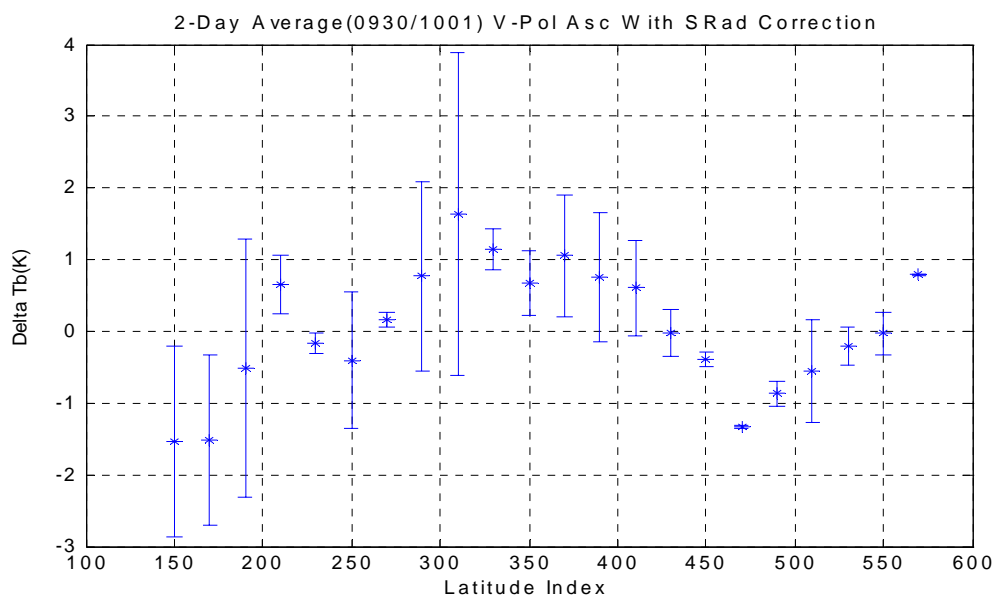


(b) After applying the empirical correction

Figure D.22 (SRad - AMSR) H-pol 2-day avg delta-Tb descending orbit segments (September 30 - October 1,2003)

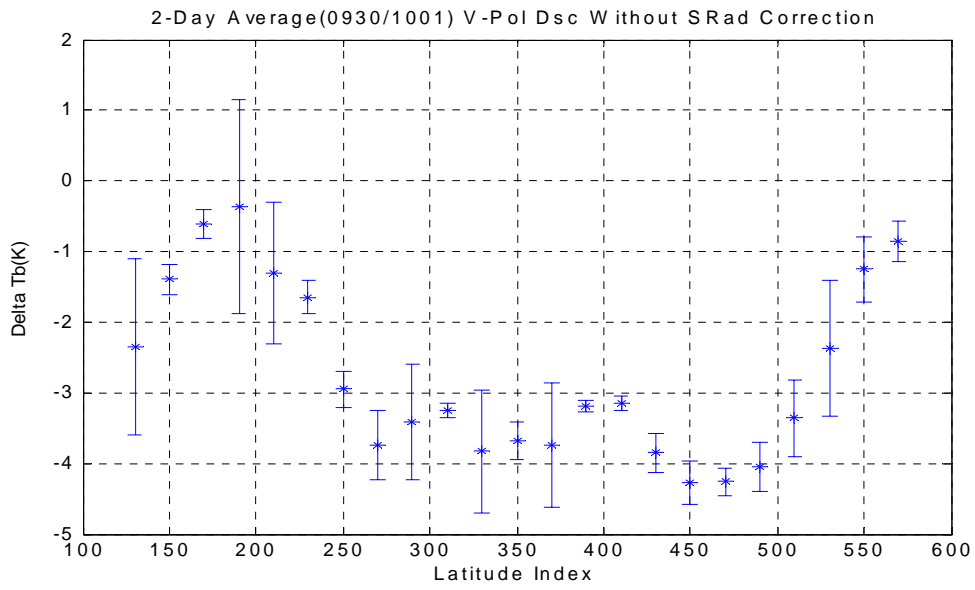


(a) Before applying the empirical correction

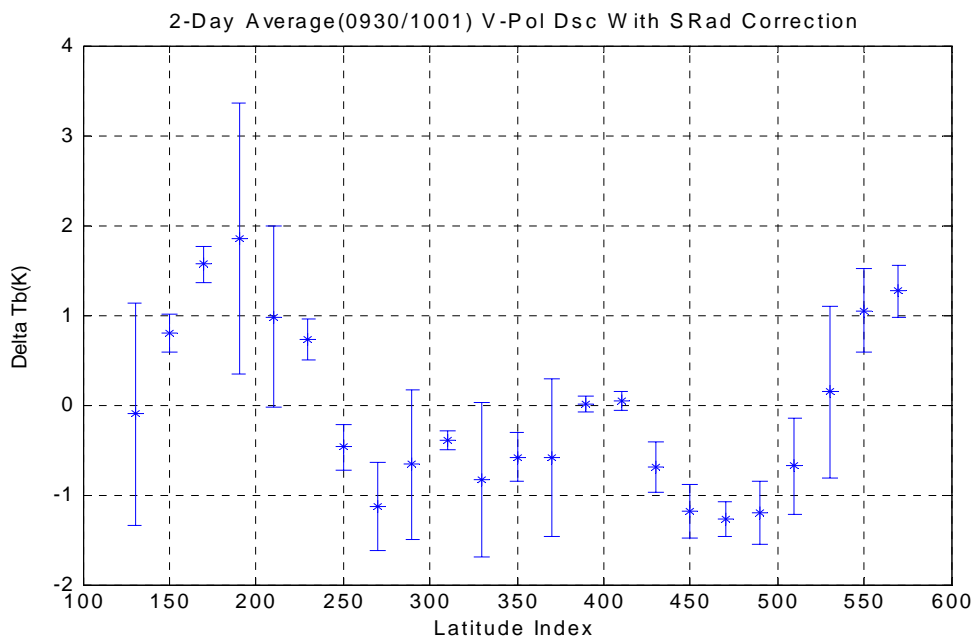


(b) After applying the empirical correction

Figure D.23 (SRad - AMSR) V-pol 2-day avg delta-Tb ascending orbit segments (September 30 - October 1,2003)



(a) Before applying the empirical correction



(b) After applying the empirical correction

Figure D.24 (SRad - AMSR) V-pol 2-day avg delta-Tb descending orbit segments (September 30 - October 1,2003)

LIST OF REFERENCES

- [1] Moore, R. K. and W. L. Jones, "Satellite Scatterometer Wind Vector Measurements – the Legacy of the Seasat Satellite Scatterometer", *IEEE Geosci and Remote Sensing Newsletter*, (132), 18-32, September 2004.
- [2] <http://winds.jpl.nasa.gov>
- [3] Thompson, Simonetta D., "Evaluation of a Microwave Radiative Transfer Model for Calculating Satellite Brightness Temperature", MS Thesis, Univ. of Central Florida, Dec. 2004.
- [4] Jones, W. L., Mehershahi, R., Zec, J. and D. G. Long, "SeaWinds on QuikSCAT Radiometric Measurements and Calibration" IGARSS'00, July 24-28, 2000, Honolulu, HA
- [5] Jones, W. L., Ahmad, K., Park, J. D. and J. Zec, "Validation of QuikSCAT Radiometer Rain Rates using the TRMM Microwave Radiometer and the Special Sensor Microwave Imager", IEEE IGARSS 2002, Jun 24-28, 2002, Toronto, Ontario, Canada
- [6] Rushad J. Mehershahi "Ocean Brightness Temperature Measurements using Quikscat Radiometer", M.S. Thesis, Univ. Central Florida, June 2000
- [7] M.Susanj, "An Algorithm for Measuring Rain over Oceans using the QuikSCAT Radiometer", M.S. Thesis, Univ. Central Florida, 2000
- [8] Yanxia Wang, "A Statistical Algorithm for Inferring Rain Rate from the QuikSCAT radiometer", M.S. Thesis, Univ. Central Florida, 2001
- [9] Ahmad, K. A., W. L. Jones, T. Kasparis, S. W. Vergara, I. S. Adams, and J. D. Park (2005), Oceanic rain rate estimates from the QuikSCAT Radiometer: A Global Precipitation Mission pathfinder, *J. Geophys. Res.*, 110, doi:10.1029/2004JD005560
- [10] Spencer, M.W.; Wu, C.; Long, D.G.; "Improved Resolution Backscatter Measurements with the SeaWinds Pencil-beam Scatterometer", *Geoscience and Remote Sensing, IEEE Transactions on* Volume 38, Issue 1, Jan. 2000 Page(s):89 - 104 Digital Object Identifier 10.1109/36.823904
- [11] Jones, W.L.; Zec, J.; "Evaluation of Rain Effects on NSCAT wind retrievals", *OCEANS '96. MTS/IEEE. 'Prospects for the 21st Century'*. Conference Proceedings Volume 3, 23-26 Sept. 1996 Page(s):1171 - 1176 vol.3
- [12] Rastogi, M; Jones, W.L.; I. S. Adams, "SeaWinds Radiometer Brightness Temperature Calibration and Validation", SouthEast Con 05, IGARSS 05